DTU Library

Efficient oxygen electrocatalysis on special active sites
A theoretical study

Halck, Niels Bendtsen

Publication date:
2014

Link back to DTU Orbit

Citation (APA):
Halck, N. B. (2014). *Efficient oxygen electrocatalysis on special active sites: A theoretical study.* Technical University of Denmark.

Efficient oxygen electrocatalysis on special active sites
- A theoretical study

Niels Bendtsen Halck

Center for Atomic-Scale
Materials Design
Department of Physics
Technical University of Denmark

Efficient oxygen electrocatalysis on special active sites
- A theoretical study

Dissertation for the Ph.D. degree in Physics

Niels Bendtsen Halck
December 2014

DTU

Preface

This thesis is submitted for the Ph.D degree in Physics from the Technical University of Denmark. The work presented here was carried out at the Center for Atomic-Scale Material Design (CAMD) between January 2012 and December 2014 under the supervision of Assistant Professor Jan Rossmeisl as part of the Catalysis for Sustainable Energy (CASE) initiative which funded this work.

Lyngby, December 31, 2014

Niels Bendtsen Halck

Abstract

Oxygen electrocatalysis will be pivotal in future independent of fossil fuels. Renewable energy production will rely heavily on oxygen electrocatalysis as a method for storing energy from intermittent energy sources such as the wind and sun in the form of chemical bonds and to release the energy stored in these bonds in an eco-friendly fashion in fuel cells.

This thesis explores catalysts for oxygen electrocatalysis and how carefully designed local structures on catalysts surfaces termed special active sites can influence the activity. Density functional theory has been used as a method throughout this thesis to understand these local structure effects and their influence on surface reactions.

The concept of these special active sites is used to explain how oxygen evolution reaction (OER) catalysts can have activities beyond the limits of what was previously thought possible. The concept is used to explain the increase in activity observed for the OER catalyst ruthenium dioxide when it is mixed with nickel or cobalt. Manganese and cobalt oxides when in the vicinity of gold also display an increase in OER activity which can be explained by locally created special active sites. Density functional theory calculation provides an insight into the how the activity is increased at these special active sites and proposes a modified reaction mechanism for the oxygen evolution reaction on these sites.

Another type of special active site can explain the production of hydrogen peroxide on nickel and cobalt incorporated in ruthenium dioxide at high overpotentials during the oxygen reduction reaction (ORR). Density functional theory calculations were used to explain this phenomenon.

The special active sites concepts are used to propose a general unified approach to increase the efficiency for oxygen electrocatalysis (ORR and OER) using organic functional groups on another class of catalysts. These consist of graphene sheets modified to have a local porphyrine site with different transition metals ions as model systems.

Resumé

Oxygen elektrokatalyse vil blive central i en fremtid uafhængig af fossile brændstoffer. Vedvarende energi produktion vil afhænge af oxygen elektrokatalyse som en måde at opbevare energi fra energikilder med varierende energi output, så som vind eller sol energi, i kemiske bindinger og bæredygtigt frigive energien gemt i disse bindinger i en brændselscelle.

Denne Ph.d. afhandling undersøger katalysatorer til oxygen elektrokatalyse og hvordan designede lokale strukturer på katalysatorens overflade her kaldet specielle active sites (på dansk særlige aktive steder) kan påvirke katalysatorens aktivitet. Tæthedsfunktionalteori er blevet brugt i denne afhandling til at undersøge og forstå deres indflydelse på overfladereaktioner.

Speciel active site konceptet bliver her brugt til at forklare hvordan oxygenudviklingskatalysatorer kan opnå aktiviteter, der er bedre, end den aktivitet, der tidligere var troet var den højest opnåelige. Dette koncept kan forklare den øgede aktivitet, der er blevet observeret i oxygenudviklingskatalysatoren rutheniumdioxid, når det er iblandet nikkel eller kobolt. Mangan og koboltoxider i nærheden af guld har også en øget oxygenudvikling der kan forklares ved hjælp af lokale specielle active sites. Tæthedsfunktionalteoriberegninger har givet en forklaring på hvordan den øget oxygenudvikling foregår på disse specielle active sites, og en ændret reaktion mekanisme for iltudvikling er blevet foreslået.

En anden type specielle active sites kan forklare produktionen af hydrogenperoxid med nikkel og kobolt inkorporeret i rutheniumdioxid ved høje overpotentialer i oxygenreduktion. Tæthedsfunktionalteoriberegninger er blevet anvendt som del af denne forklaring

Konceptet med disse specielle active sites er også brugt til at foreslå en general tilgangsvinkel til at øge effektiviteten for oxygenelektrokatalyse (oxygenudvikling og reduktion) ved hjælp af organiske funktionelle grupper på en gruppe katalysatorer. Denne type katalysatorer består af grafen der er modificeret til at have et lokalt område der minder om porfyrin med forskellige overgangsmetal ioner og de er brugt som model system.

Acknowledgements

I have really enjoyed my time at DTU and the 3 years working on this Ph.D project have gone by so quickly. Many people that have been around me in these 3 years at CAMD deserve to be acknowledged for their role in this work.

My most sincere and deepest thanks go to my supervisor Jan Rossmeisl. I feel privileged to have been selected for this project and been given the opportunity to work with such a dedicated and knowledgeable individual who is so passionate about his field.

I would also like to thank Marianne Ærsøe, Head of Administration, Ole Holm Nielsen, Head of Computer Services, Marcin Dulak, Computer Engineer and Jens Jørgen Mortensen, Computer Engineer, for allowing me to focus less about red tape and computer technicalities and GPAW oddities and more about research. It feels odd to acknowledge a super computer but without Niflheim this work would not be possible.

I would like fellow co-workers at CAMD both for valuable discussions about work and "stuff". Thanks to the Electrochemistry Group both former and current members especially the experienced Mårten Björketun, Vladimir Tripkovic and Micheal Busch for valuable discussions, office mates during the 3 years and the lunch gang, Kristian Ørnsø, Mohnish Pandey, Kirsten Andersen, Martin Hansen, Manuel Šaric, Chengjun Jin, Christopher Patrick, Korina Kuhar and Jakob Madsen for distracting me at just the right time for lunch or coffee.

I also want to thank the people from J. Heyrovsky Institute in Prague especially Petr Krtil for collaboration on several projects. It has been both challenging and rewarding.

Mohnish Pandey and Mårten Björketun thank you for helping with proof-reading the thesis.

I could not have done this without the help and support from my wife, Christina. Thank you so much.

List of Included Papers

Paper 1

Beyond the volcano limitions in electrocatalysis – oxygen evolution reaction

Niels Bendtsen Halck, Valery Petrykin, Petr Krtil and Jan Rossmeisl.
Phys. Chem. Chem. Phys., 2014, **16**, 13682.

Paper 2

Enhancing activity for the oxygen evolution reaction: The beneficial interaction of Au with Mn and Co oxides

Rasmus Frydendal, Michael Busch, Niels Bendtsen Halck, Elisa A. Paoli, Petr Krtil, Ib Chorkendorff and Jan Rossmeisl.
CHEMCATCHEM, accepted.

Paper 3

Oxygen reduction on nanocrystalline ruthenia – local structure effects

Daniel F. Abbott, Sanjeev Mukerjee, Valery Petrykin, Zdeněk Bastl, Niels Bendtsen Halck, Jan Rossmeisl and Petr Krtil.
RSC Advances, accepted

Contents

1 Introduction

Fossil fuels are without doubt the most efficient and easiest way to produce energy. The energy demand will only increases the population continues to grow and the more people want access to a better life quality. In 2012 the world energy consumption reached around 13371 million tonnes of Oil Equivalent or roughly 16,3 TW [1] and this is expected to increase in the future. By 2050 the consumption will reach somewhere around 30 TW which is a very conservative estimate assuming a lower growth rate that we have currently [2].

The easy access to energy has come at a great price. The increase in CO_2 and other greenhouse gas emissions are extremely likely to be the cause of global warming and observed climate changes such as risen sea-levels and an increase in extreme events such as floods, heat waves, cyclones and droughts [3].

Even without the risk of more severe climate changes at some point a transition away from fossil fuels is required as it is a finite resource even though there is still a debate of long the planets reserve of fossil fuels will last.

It is still urgent to find a clean and more sustainable alternative to fossil fuels. Renewable energy sources such wind and solar power has the potential to replace fossil fuels. Nevertheless, the scale up will not be without difficulties. The sheer amount of energy required to replace fossil fuels put a heavy constraint on material selection [2], [4], [5] which has to abundantly available or used in tiny amounts.

The ultimate power source is the sun and the catalysis for sustainable energy (CASE) is a research initiative and its goal is to utilise the power of the sun and store the energy in the form of chemical bonds using catalysis. The most direct approach is to use photo-electrocatalysis to convert the energy of the sun into chemicals in step. Alternatively it can be done indirectly by converting biomass into chemicals using catalysis or using the electricity generated from wind turbines or solar cells to form bonds using electrocatalysis. A visualisation of the possibilities for using the sun and catalysis to obtain fuel explored by the CASE initiative is shown in Figure 1.1.
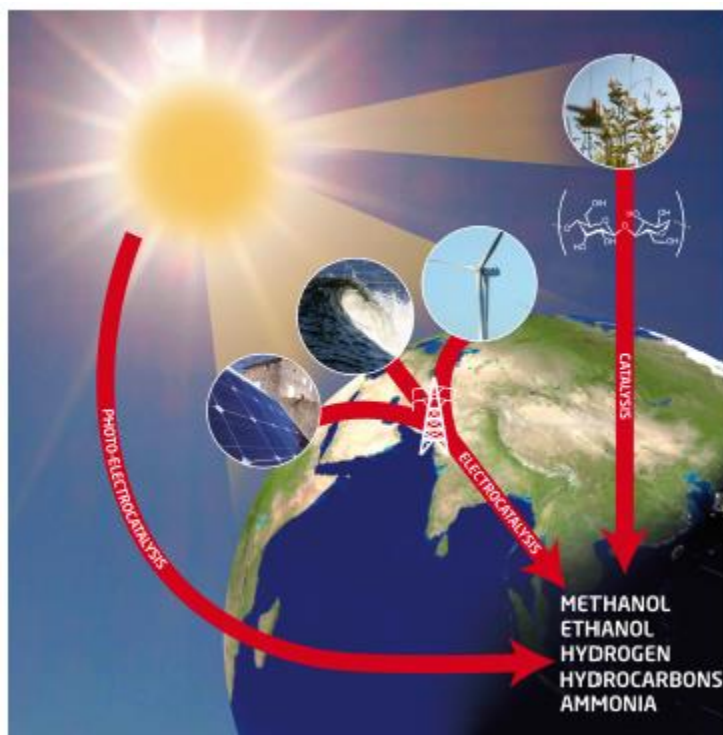
Figure 1.1: Possible routes to harvest the energy of the sun and store in the form of valuable chemicals supported by the CASE initiative.

Denmark has high ambitions for sustainable energy production. The goal is to have fossil fuels phased out and replaced by renewable energy sources by 2050. This includes fossil fuels for transportation as well [6]. As more and more energy is produced from intermittent power sources such as wind turbines and solar cells energy storage becomes a major concern. Even today Denmark has in some periods, a surplus of electricity generated from wind power and the problem will be more noticeable in the future.

Energy storage will play a vital role for a continued increase in electricity generation from intermittent sources. Electricity could be stored to provide energy for cloudy and windless days. Options of storing electricity include batteries and storing it as potential energy by pumping water up into high altitude water reservoirs. Battery technology is not yet a viable option as they are expensive and has a low energy density compared to fossil fuels. Pumping water to high altitude water reservoirs is also expensive and would require help from neighbouring countries which have mountain ranges suitable for these reservoirs [2].

Another option is to store the energy from electricity in the form of chemical bonds using electrocatalysis in electrolysers. Water electrolysis represents a clean and CO_2 emission free process for converting the water into hydrogen and

oxygen if the electricity used is from renewable energy sources. The hydrogen can be stored and used in fuel cells to get electricity back. Electrocatalysts are needed for both hydrogen and oxygen evolution reaction (OER). However, it is the OER which limits the overall efficiency in water electrolysers. In fact, the OER and its counterpart the oxygen reduction reaction (ORR) collectively known as oxygen electrocatalysis is a fundamental bottleneck for widespread use of sustainable energy conversion from water electrolysers and fuel cells. Still, water electrolysis represents a relatively easy method for obtaining hydrogen.

Computational studies offer valuable insight into the thermodynamics of electrochemical reactions and allow for studies of catalysts at an atomic level which is yet to be achieved by experimental techniques. The computational studies enter as the part of the workflow shown on Figure 1.2 for understanding the theory behind catalysis. Theory and computational studies are an integral part of catalysts design on equal terms with synthesis, characterisation and testing.
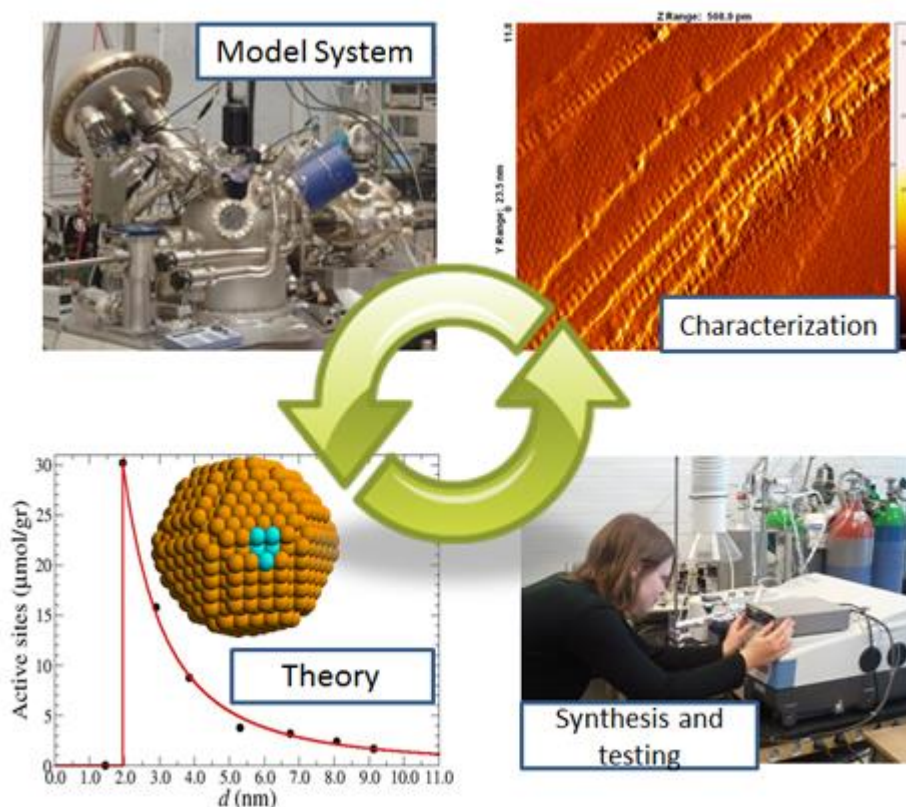
Figure 1.2: Ideal workflow cycle between synthesis, theory (computational studies), model systems and Characterisation. Figure is courtesy of www.cinf.dtu.dk

2 Theoretical basis

In this section the theoretical basis for this thesis will be described starting from the very fundamentals of quantum mechanics, the Schrödinger equation and the electronic structure problem. This leads to the popular method of density functional theory and how it can be used to calculating thermodynamic properties such as reaction energies and ends with the concept of the computational hydrogen electrode. These concepts form the basis of theoretical eletrocatalysis which is the subject of this work.

2.1 The electronic structure problem

Condensed matter physics and chemistry typically try to describe systems of atoms with its interacting nuclei and electrons. At these small length scales Newton's laws of motion are no longer valid. The analog of Newton's second law in this world is the time-dependent Schrödinger equation [7]. In its time-independent form its solutions describe the ground state of a system:

$$\hat{H}\Psi = \varepsilon\Psi \tag{2.1}$$

$\hat{H}$ is the Hamiltonian of the system, Ψ is the wavefunction and ε is the total energy. The Schrödinger equation is deceptively simple but the Hamiltonian contains the kinetic energy of the electrons and nuclei (T_e and T_N), interactions terms for the Coulumbic attraction between nuclei and electrons, electron-electron repulsion and nuclei-nuclei repulsion (V_{Ne}, V_{ee} and V_{NN}). Written in atomic units the Hamiltonian is then given by:

$$\hat{H} = \hat{T}_e + \hat{T}_N + \hat{V}_{Ne} + V_{ee} + V_{NN} \tag{2.2}$$

The kinetic energy for the electrons in the Hamiltonian is given by:

$$\hat{T}_e = -\frac{1}{2}\sum_{i=1}^{N}\nabla_i^2 \tag{2.3}$$

The kinetic energy of the protons is given by:

$$\hat{T}_N = -\frac{1}{2}\sum_{I=1}^{K}\frac{1}{M_I}\nabla_I^2 \tag{2.4}$$

The Coulumbic interaction between the positive nuclei and negative electrons is a double sum over the number of the electrons and nuclei:

$$\hat{V}_{Ne} = -\sum_{i=1}^{N}\sum_{I=1}^{K}\frac{Z_I}{|r_i - R_I|} \tag{2.5}$$

The electron-electron repulsion term:

$$V_{ee} = \sum_{i=1}^{N-1} \sum_{j>i}^{N} \frac{1}{|r_i - r_j|} \tag{2.6}$$

The last term in the Hamiltonian is the nuclear-nuclear repulsion term:

$$V_{NN} = \sum_{I=1}^{K-1} \sum_{J>I}^{K} \frac{Z_I Z_j}{\left\|R_I - R_J\right\|} \tag{2.7}$$

In the equation 2.3-2.7, Z is the atomic number of the nuclei, so its charge, M is the mass of the nuclei, r is the position of the electrons and R is the position of the nuclei. Solving this equation even numerically is only possible for very few particles and therefore approximations are needed.

The Born-Oppenheimer approximation [8] is one of these approximations and a very commonly used one. It states that since the nuclei are three orders of magnitude heavier than the electrons the nuclei are effectively stationary when compared to the speed of the electrons. This means that the Hamiltonian above can be split into an electronic Hamiltonian and a nuclear Hamiltonian as the kinetic energy of the nuclei, T_N can be removed and the nuclei-nuclei repulsion is constant. The electronic Hamiltonian is written as:

$$\hat{H} = -\frac{1}{2} \sum_{i=1}^{N} \nabla_i^2 + \sum_{i=1}^{N} \sum_{I=1}^{K} \frac{Z_I}{|r_i - R_I|} + \sum_{i=1}^{N-1} \sum_{j>i}^{N} \frac{1}{|r_i - r_j|} \tag{2.8}$$

More approximations are needed given the sheer number of coupled equations and variables that arises for any realistic system. There are several methods of solving this many-body problem. A very popular method is density functional theory (DFT). Its popularity is mainly due to its great compromise between accuracy and computational demand.

2.2 Density functional theory

Density functional theory is based on two theorems presented by Pierre Hohenberg and Walter Kohn in 1964 [9] which essentially accepts that the many-body problem of any realistic number of electrons and protons is unsolvable and another approach is needed.

2.2.1 Hohenberg-Kohn theorems

The first theorem by Hohenberg and Kohn states that "*there is a one to one correspondence between the ground state electron density and the external potential acting the system*".

This effectively means that all ground state properties can be obtained from the electron density. The total energy of the system E[ρ] is a functional of the electron density ρ(r) and depends on the external potential, V_{ext}, the kinetic energy, T, and the potential energy from the electron-electron interactions, V_{ee}:

$$E[\rho(r)] = \text{T}[\rho(r)] + \text{V}_{ee}[\rho(r)] + \int V_{ext}\rho(r)dr \qquad \text{2.9}$$

So for any given external potential there is one unique ground state electron density. Using the ground state electron density instead of the positions of the electrons the number of variables are reduced from three variables per electron to just three.

The second theorem by Hohenberg and Kohn states *"that for any density the ground state energy is the minimum value of the energy functional"*.

The basis for DFT has been developed using these two theorems. The total energy of the system is a functional of the density and the minimum of this energy functional is the ground state energy which can be found using the variational principle. However, there is no information about the form of the functionals or how to determine them.

2.2.2 The Kohn-Sham scheme

The scheme that provides the necessary framework for making an approximation for finding the ground state density was published a year later by Walter Kohn and Lu Jeu Sham [10]. The challenge with correlating the external potential with the ground state electron density is the electron-electron interactions. Instead of finding a method for incorporating the electron-electron interaction, Kohn and Sham used a reference system which is entirely fictitious and has non-interacting electrons. This fictitious non-interacting reference system is constructed so that it gives the same ground state electron density of the system with interacting electrons. The Kohn-Sham Hamiltonian with non-interacting electrons is given by:

$$\hat{H}_{KS} = -\frac{1}{2}\sum_{i=1}^{N}\nabla_i^2 + v_{eff}(r) \qquad \text{2.10}$$

v_{eff} is the effective potential which ensures that the non-interacting reference system has the same ground state electron density as the real interacting system. The Kohn Sham equations are then the Schrödinger equation which used the Kohn-Sham Hamiltonian.

$$\left(-\frac{1}{2}\sum_{i=1}^{N}\nabla_i^2 + v_{eff}(r)\right)\psi_i(r) = \varepsilon_i\psi_i(r) \qquad \text{2.11}$$

6

The associated wavefunctions are related to the electron density:

$$\varepsilon_i(r) = \sum_{i=1}^{N} |\psi_i(r)|^2 \qquad\qquad 2.12$$

The effective potential, v_{eff} is a sum of the external potential which is mainly generated by the nuclei of system, v_{ext}, the Hartree potential which is the classical Coulumb interactions between the electrons, v_H, and lastly the exchange-correlation potential v_{xc}.

$$v_{eff}(r) = v_{ext}(r) + v_H(r) + v_{xc} \qquad\qquad 2.13$$

This set of equations can be solved iteratively by starting with a trial wavefunction to determine an electron density and potential. Using the electron density a new wavefunction can be determined and the process is continued until self-consistency within a given convergence criteria is met. This is an exact formalism if it was not for the nature of the exchange-correlation functional

2.2.3 Exchange-correlation functionals

The exchange-correlation functional is a subject of its own. It is defined by its potential which is a functional derivative of $E_{xc}[\rho(r)]$:

$$v_{xc} \equiv \frac{\delta E_{xc}[\rho(r)]}{\delta \rho(r)} \qquad\qquad 2.14$$

The exchange correlation functional is the contribution from exchange and correlation which makes the Kohn-Sham equations exact. It is also the collective contribution of all the things we can't describe. Therefore approximations are required.

Although the exchange-functional cannot be described mathematically the physical origin of exchange and correlation is known. Exchange is due to electron being fermions and is subject to the Pauli exclusion principle. Two electrons cannot occupy the same position if they have the same spin. This gives an extra repulsion in addition to the repulsion from the electronic charge. Correlation is due to the motion of the electrons are not independent. The Coulomb repulsion decreases the likelihood of finding two electrons of in the vicinity of each other. The motion of the electrons is correlated and the electron density is therefore not homogenous.

The level of accuracy of a given approximation will determine the reliability of the calculated ground state energy using DFT. Here two classes of approximations will be described, the local density approximation, LDA, and the

generalised gradient approximations, GGA. The reason that the exchange and correlation are approximated together is due to cancellation of errors.

In the LDA approximation exchange and correlation is obtained using the exchange and correlation from the homogeneous electron gas which is a system of N electrons held together by a uniform positive background charge.

$$E_{xc}^{LDA} = \int \rho(r) e_{xc}^{HEG}(\rho(r)) dr \qquad\qquad 2.15$$

Due to the simple nature of the homogeneous electron gas the exchange part of e_{xc} is known exactly and the correlation part is calculated using very accurate quantum Monte-Carlo simulations. The LDA is only accurate for systems with slowly varying electron densities but has proved its merit over time. LDA has some shortcomings such as favouring homogeneous systems, overbinding of molecules and solids [11].

While the LDA approximation is somewhat crude it performs reasonable well and it also the basis for the next level of approximation the GGA. For the GGAs the gradient of the density is also taken into account which better describe systems with varying electron density. While this improves many properties such as bond lengths and total energies the GGA tend to overcorrect when comparing to experimental data. Unlike the LDA where the e_{xc}^{HEG} is a known function it is not case for GGA which means that several GGAs exist. A very popular GGA is the PBE [11] which comes in various variations such as PBEsol for solids[ref], RPBE for adsorption energies [12] etc. In general the GGAs can written as a function of the exchange energy obtained from LDA ε_x^{LDA}:

$$E_{xc}^{GGA} = \int \rho(r) \varepsilon_x^{LDA}(\rho(r)) F_x(s(r)) \qquad\qquad 2.16$$

In which the exchange enhancement factor, F_x, is given by:

$$F_x(s(r)) = 1 + \kappa - \frac{\kappa}{1 + \mu(s(r))^2/\kappa} \qquad\qquad 2.17$$

Here s(r) is the reduced density gradient which is given by.

$$s(r) = \frac{|\nabla \rho(r)|}{2(3\pi^2)^{1/3} \rho(r)^{4/3}} \qquad\qquad 2.18$$

For PBE the values of $\kappa = 0.804$ and $\mu = 0.21951$ are chosen to obey the LDA limit at Fx = 0 and the Lieb-Oxford lower bound. revPBE [13] was created to give better adsorption energies but violates the Lieb-Oxford lower bound. In case of RPBE exchange enhancement factor was changed to obey the Lieb-Oxford lower bound. The exchange enhancement factor is changed to:

8

$$F_x\big(s(r)\big) = 1 + \kappa \left(1 - e^{-\mu(s(r))^2/\kappa} \right) \qquad\qquad 2.19$$

With κ = 0.804. As a result RPBE gives better adsorption energies than PBE the RPBE functional is used throughout this thesis.

This is only a brief review of the key concepts in DFT. For a more comprehensive review the ABC of DFT is excellent [14].

2.3 Applied density functional theory

Two open source codes have been used throughout this thesis, Dacapo and GPAW to determine the total energy of the systems described in this thesis. As already established DFT is a powerful approximation to finding the ground state energy but for any practical use of DFT further approximation is needed.

The Kohn-Sham wavefunctions has to be expanded in some form. Dacapo uses plane-waves and GPAW was initially only a real-space grid code but now have modes which use plane-waves and linear combination of atomic orbitals.

2.3.1 Plane waves and real-space grid

Using plane waves to describe the wave functions is very advantageous for periodic systems as the plane waves can be selected to match the periodicity of the system using Bloch's Theorem [15]. The wavefunctions expanded as plane waves in reciprocal space is given by:

$$\psi_i(r) = \sum_G c_i G e^{i(G+k)r} \qquad\qquad 2.20$$

G is the reciprocal lattice vectors, k is the wave vector in the first Brilliouin zone and c_i are the expansion coefficients. To truly represent the wave functions an infinite number of plane waves would be required but the infinite sum of plane waves can be truncated using a cut-off energy, E_{cut}, such that

$$\frac{1}{2}|G + k| \leq E_{cut} \qquad\qquad 2.21$$

The cut-off energy has to be chosen carefully to converge the total energy of the system or other property. It is element dependent but the energy of the system will decrease monotonically towards the ground state energy due to the variational principle.

Wavefunctions can also be expanded on a real-space grid which is the finite-difference mode in GPAW [16]. Instead of the cut-off energy the convergence parameter is the grid spacing. The advantage of the real-space grid compared to

the plane waves is when calculating large systems the finite difference mode parallelize better than plane waves which result in faster convergence . However the plane-waves are better for smaller systems.

For both methods it is important to note that the cut-off energy and the grid spacing is not the only parameter to converge. There is also the matter of k-point sampling in the first Brillouin zone [17]. The wave functions must be evaluated at each reciprocal lattice vector and the number of these vectors can be infinite. In practice only a limited number of k-points are needed and it is a balance between having too few k points which will lead to questionable physical properties and too many k-points which will provide no benefit and will require excess computational power.

2.3.2 Pseudopotentials and projector-augmented wave method

The wavefunction of the electrons near the nuclei oscillates rapidly and it would require a very fine grid or very high cut-off energy in order to describe these oscillations accurately. Fortunately it is mainly the valence electrons which describe chemical properties. The approach to dampen these oscillations is to replace the real potential with a pseudo-potential which gives the correct wave-function outside a chosen radius. This reduces the computational time required for a given system substantially. In the Dacapo implementation the core electrons are represented by ultrasoft Vanderbilt pseudopotentials [18]. In GPAW the projector augmented wave method is used [17] and the pseudopotential equivalent is called a setup. Smooth wave-functions so-called projector functions replaces the all electron wave-functions when doing DFT calculations but in such a way that still provides access to the all-electron wave functions, density and potential if needed.

It is important to note that the total energy of system is not meaningful on its own as it will depend on the choice of pseudopotentials or setup. However, the energy difference between two systems is still a meaningful quantity as long the energies have been calculated with same pseudopotential or setup.

Another concern when performing DFT calculation is regarding the distinction between core and valence electrons. The inclusion of semi-core electrons in elements such as Ti and Ru can be important for some properties and irrelevant for others but calculations which include semi-core electrons can be difficult to converge. The developers of GPAW have solved this by introducing two different set of setups with or without semi-core electrons for relevant elements and left

10

it to the user to decide which setup is suitable for the problem at hand. In this thesis the work regarding RuO_2 is done using setups without semi-core electrons and for the more recent work on MnO_x and functionalised graphene sheets the setups including semi-core electrons was used.

2.4 Gibbs free energy and catalysis

The definition of the Gibbs free energy of a chemical reaction (G_r) is the difference between the Gibbs free energies of the all the products and all the reactants. For a general reaction the Gibbs free energy (G_r^0) is defined as:

$$\Delta G_r^0 = \sum G_{products}^0 - \sum G_{reactants}^0$$
2.22

The 0 denotes standard conditions meaning 298.15K, 1 atm of pressure and a molar concentration of 1M.

In an electrochemical cell the standard cell potential can be obtained from the Gibbs free energy of the net reaction that occurs in the cell:

$$\Delta G^0 = nFE_{cell}^0$$
2.23

Here n denotes the number of electrons involved in the reaction and F is Faradays constant. The standard cell potential E_{cell} is the difference between the standard potential of the cathodic and anodic reaction. In order to measure the potential at a single electrode a reference is needed.

The International Union of Pure and Applied Chemistry, IUPAC, defines the electrode potential as the electromotive force of a cell in which the electrode on the left is a standard hydrogen electrode (SHE) and the electrode on the right is the electrode in question. The electrode reaction considered is:

$$H_{(aq)}^+ + e^- \rightarrow \tfrac{1}{2}H_{2(g)}$$
2.24

The absolute potential of the standard hydrogen electrode is by recommended by IUPAC to be set to 4.44 ± 0.02V but the exact value is still debated [19], [20]. As it used as a reference for all other electrode reactions in electrochemistry it is set to 0 by definition.

The standard cell voltage the is ideal potential that can be obtained for a electrochemical reaction but there are usually several losses associated with actual electrochemical devices such as full cells and electrolysers which prevents reaching the standard cell voltage.

These losses at a single electrode are collectively called the overpotential. The overpotential is essentially the difference between the potential at which a given redox reaction occurs on a given electrocatalyst surface and the standard potential (pH= 0, T = 298,15K and p = 1 atm.).

Electrocatalysis is a subfield within catalysis in which catalysts modifies the rate of reaction on an electrode surface within an electrochemical cell. In regular catalysis a catalyst will reduce the activation energy of a chemical reaction which will make a reaction occur where it previously could not, or increase the rate of reaction without being consumed. A catalyst change the reaction mechanism by lowering the energy of select intermediates some of which are rate determining or by introducing more intermediate which have a lower energy between the initial reactant and the final product. A Schematic of this can be seen on Figure 2.1.
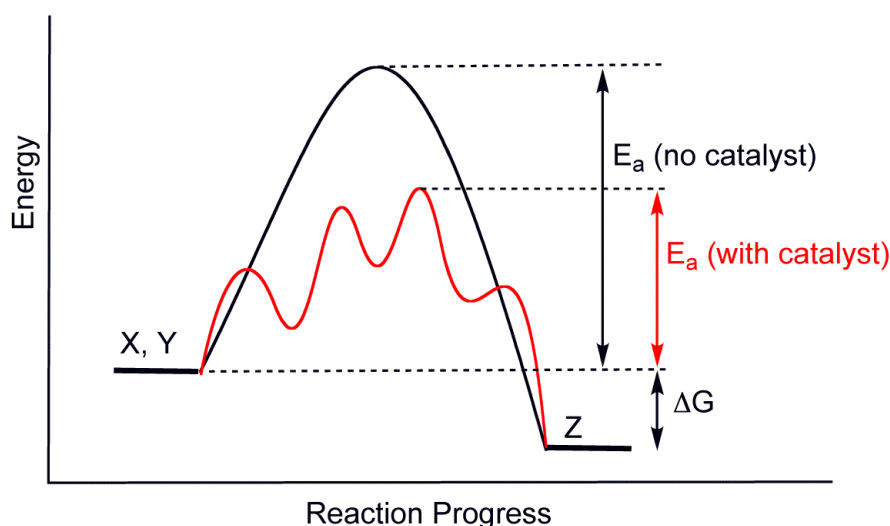
Figure 2.1: Two hypothetical methods of converting X and Y into Z. The black line represents the activation energy barrier (E_a) for converting X and Y to Z with no catalyst present. The red line represents the effect of the catalyst. The catalyst introduces several intermediate steps and lowers the activation energy. ΔG is the free energy of the reaction and is the energy gained in this case from converting X and Y to Z. This schematic is courtesy of http://en.wikipedia.org/wiki/Catalysis.

An electrocatalyst mounted on an electrode surface will lower the overpotential and the reaction will approach thermodynamic equilibrium which can be directly translated into saving energy in electrolysers when splitting water into H_2 and O_2.

2.5 Gibbs free energies from DFT

The total energies of a system obtained from DFT whether it is molecules or surfaces are calculated in vacuum and 0 K unless solvent is explicitly added. The

positions of the atoms are changed using a minimisation algorithm such as the Broyden–Fletcher–Goldfarb–Shanno (BFGS) algorithm to find the configuration with the lowest energy by varying the atomic positions. The minimum energy found is not the Gibbs free energy as zero-point energies and the entropic contribution needs to be included afterwards. The Gibbs free energy can be expressed in terms of the DFT energy like:

$$G = E_{DFT} + ZPE - TS + pV \qquad\qquad 2.25$$

At 0 K the atoms still vibrate and this effect is neglected by the Born-Oppenheimer approximation. This correction to the DFT energy is the zero-point energy correction and can be determined using vibrational analysis in which atoms are displaced to find the vibrational modes of the system using a harmonic approximation. The sum of contributions from all vibrational modes, i, are given by:

$$ZPE = \frac{1}{2}\sum_i h\omega_i \qquad\qquad 2.26$$

ω_i is the oscillation frequency and h is Planck's constant. The ZPE correction is usually only relevant for light elements that are loosely bounded together. For bulk materials or surfaces the effect is much smaller than the uncertainties in the DFT energy calculation. For gas-phase molecules and adsorbates on a surface that are studied in this work ZPE effects should be considered as they can vibrate more freely. The sum of the DFT energy and the ZPE correction can be thought of as an enthalpy and to obtain the Gibbs free energy the entropy term is needed. Tabulated values for the entropy contribution of the gas phase species are obtained from literature such as Atkins' Physical Chemistry [21] and only the vibrational component of the entropy, obtained from a vibrational analysis, is used for the adsorbed species as the remaining entropic contributions either cancels due to only looking at energy differences or are negligible. For liquid species the entropy correction is determined at the equilibrium pressure at standard conditions and these are also available in literature [21]. In principle the total zero point energy and entropy corrections are only relevant for H containing adsorbates when referenced to H_2 due to steep potential well and correspondingly large gaps in the energy levels in this potential well.

For O_2 the free energy is obtained from the experimental formation energy as O_2 with respect to water, since O_2 is not very well described within DFT and deviates from experimental values with around 0.5 eV [22].

2.6 Fuel cells and electrolysers

Fuel cells and electrolysers share the same relationship as the oxygen reduction reaction (ORR) and oxygen evolution reaction (OER). A fuel cell is an electrochemical device which resembles the galvanic cell a lot but it is fed the fuel and oxidising agent which react at the anode and the cathode respectively producing power for utilisation. A sketch of a polymer exchange membrane (PEM) which is also sometimes referred to as a solid polymer electrolyte (SPE) fuel cell is shown in Figure 2.2.
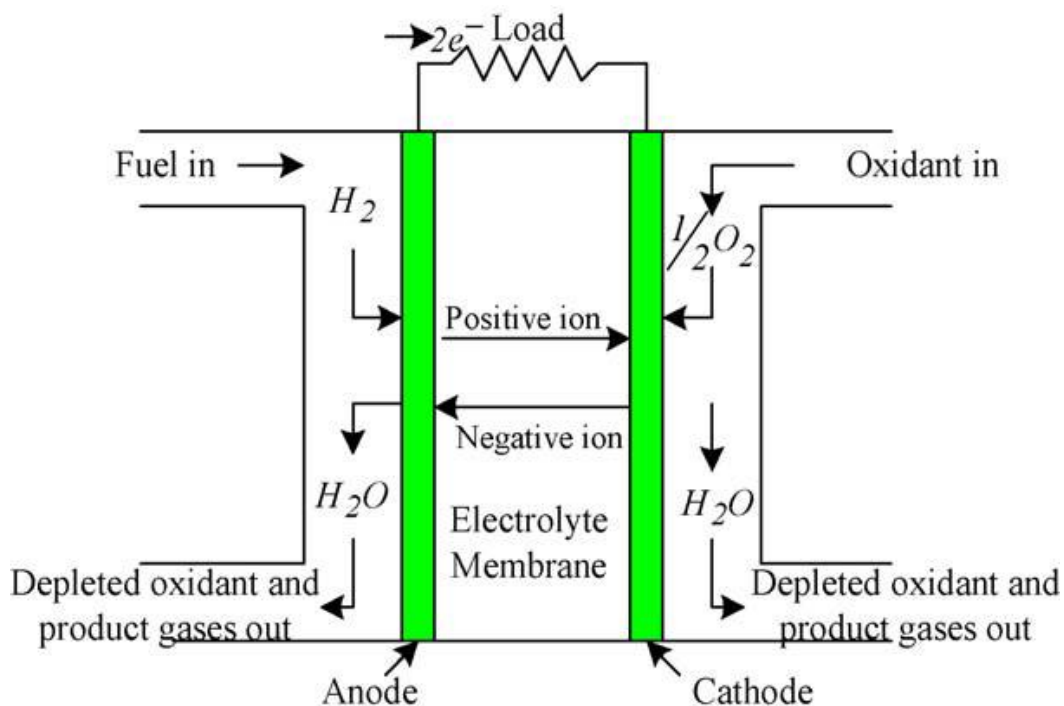

Figure 2.2: Fuel cell diagram showing the essential components of a fuel cell. Adapted from [23]

The fuel is oxidised at the anode (in this case, H_2 is being oxidised to H_2O) while the oxidant is reduced at the cathode (here is the reduction of O_2 to H_2O). The reactions take place at the catalyst surface of the respective electrodes. The electrons are passed through the external circuit producing electricity as the electrolyte membrane allows for the transfer of ions but not electrons between the anode and cathode. The PEM fuel cells are particularly interesting as the polymer membrane conducts protons and enables a very compact design which could replace internal combustion engines. However, there are still issues with durability, cost and scarcity of catalyst materials which prevent industrial scale applications [24].

For water electrolysers there are three different types based on the nature of the electrolyte. These types are the alkaline, PEM and solid oxide electrolysers. The

alkaline electrolysers are the most mature technology and offer the possibility for very pure hydrogen and oxygen production and are suitable for large scale production facilities.

For more decentralised production of hydrogen the PEM electrolysers which have a solid proton conducting membrane have great potential but the more corrosive environment requires more noble catalysts for the anodic oxygen evolution reaction. There are PEM electrolysers available on the market but on much smaller scale than the alkaline electrolysers [25]. A PEM like membrane for alkaline water electrolysis is heavily desired to develop the field of alkaline polymer electrolyte electrolysers (APE) but for now liquid KOH is the electrolyte used for commercial alkaline water electrolysis. The liquid KOH electrolyte give issues with safety and requires large facilities for the electrolysis [26]. However, the catalyst material is cheap and abundant as Ni based catalysts are quite effective and stable enough in the alkaline electrolyte [25].

While alkaline water electrolysis is the technology used in industry, PEM water electrolysis has some advantages. The PEM water electrolysers are much more compact due to the polymer electrolyte and it can operate at twice as a high current densities compared to alkaline water electrolyser [27]. A very popular membrane used in PEM electrolysers is Nafion®. This polymer membrane consists of perfluorosulfonic acid and is also used in the chlor-alkali process [28] and serves as the acidic electrolyte and the gas separator. This, combined with the higher current density, could potentially allow each household to produce its own power for consumption using solar cells when sunny and storing the excess power in hydrogen using a water electrolyser for use at night or when cloudy.

However, the advantages mentioned above come at a cost. Currently PEM water electrolysers have problems with durability of the polymer electrolyte. PEM electrolysers requires very noble catalysts such Pt-Ir for the anode [29] or the dimensionally stable anode (DSA®) [30]. The DSA® are made of titanium and are coated with mixed oxides usually RuO_2, IrO_2 as the electrocatalysts when used for the OER. TiO_2 is added in order to increase the stability. However, the catalyst loading is still too high for these materials cannot step up to the terawatt challenge [5].

The PEM water electrolysers have been investigated as a viable method for producing hydrogen in a system where they are connected directly to the power grid and a system where they are not. If the full potential of water electrolysis and a clean production of H_2 is going to be realised either major improvements for water electrolysers in terms of efficiency and cost is needed [31]. Without

this the cheapest process and the main source of H_2 is currently steam reforming which converts hydrocarbons such as methanol into CO, CO_2 and H_2. This does not solve the CO_2 emission problems but could be a cross-over technology to become independent of decreasing fossil fuel deposits. The problem with steam reforming is that the hydrogen must be post processed to remove any residual CO if the hydrogen is for use in fuel cells as CO is a known to poison the Pt based catalysts [32].

For both PEM fuel cells and electrolysers it is widely acknowledged that the largest part of the overpotential is due to the poor OER or ORR activity. This does not matter if it in PEM water electrolysers [33] or solar water splitting cells [34]. There is a great focus on designing better catalysts for these reactions and/or replacing the current state-of-art materials with cheaper alternatives which is also the topic of this work. There are other causes to overpotentials also called loses in fuel cells and water electrolysers which will be more important as more efficient catalysts for oxygen electrocatalysis is found.

Parasitic reactions can lower the equilibrium electrode potential. This is mostly due to fuel crossover through the electrolyte. The support and catalyst can also be corroded.

There are also ohmic losses which are due to the resistance in the electrical contacts and the electrolyte.

Lastly, there are mass transport issues which are due to the oxygen transport through the diffusion medium and the electrode layer.

The mentioned causes to the overpotential is based on the PEM fuel cells [35] but as the design of a PEM fuel and water electrolyser is so similar these contribution to the overpotential are the same.

2.7 Computational hydrogen electrode

The computational hydrogen electrode (CHE) developed by Nørskov, Rossmeisl and co-workers [36] has been used throughout this thesis to calculate adsorption energies for intermediates for the electrochemical evolution or reduction of O_2. The CHE resembles the SHE as the electrode reaction is the same, the evolution of hydrogen:

$$H^+_{(aq)} + e^- \rightarrow \tfrac{1}{2}H_{2(g)} \qquad\qquad 2.27$$

As chemical potential of solvated protons and electrons are notoriously difficult to determine using DFT, the CHE allows for the replacement of these chemical

potentials with the chemical potential of a hydrogen molecule in the gas phase which is obtainable using DFT. Now the adsorption energies which involve coupled proton and electron transfers can be determined using molecules in the gas phase as a reference.

A suitable example is the binding of water to an active site on a surface, denoted by *. This will form an adsorbed *-OH intermediate on the surface and release a proton and an electron. The reaction is given by:

$$* + H_2O \rightarrow \text{*-OH} + H^+ + e^-$$ 2.28

The associated reaction free energy using the CHE model which replaces the energy of the electron and proton with half a hydrogen molecule is:

$$\Delta G^0 = E(*-OH) + \frac{1}{2}E(H_2) - E(*) - E(H_2O) + \Delta ZPE - T\Delta S$$ 2.29

Where the E is the energies of the systems calculated using DFT, ΔZPE are the zero-point energy corrections and TΔS are the entropic contributions of the involved species.

Equation 2.29 only applies to standard conditions (pH= 0, T = 298,15K and 1 atm of pressure) and with no applied potentials. The free energy changes with applied potential with eU where U is the potential and e is the charge of the electrons and protons involved in the reaction. pH effects are added via the Nernst equation which takes concentration effects into account meaning that the reaction free energy is given by:

$$\Delta G(U) = \Delta G^0 - neU - kTln([H^+])$$ 2.30

Here k is the Boltzmann constant, T is the temperature and n is number of electrons.

For a reaction to be spontaneous the reaction free energy of each of the involved steps in the reaction mechanism needs to be negative. By tuning the potential (U) otherwise unstable intermediates which have a positive binding energy at 0 potential binds to the surface by applying a potential allowing for surface reaction to occur. By applying a potential endothermic reaction such as OER can occur on electrode surfaces. The free energy diagram for rutile RuO_2 [37] is used to illustrate the effect of applying a potential and is shown in Figure 2.3. At no applied potential the OER is uphill and at a potential of 1.23V this is still the case even though that is the thermodynamic equilibrium potential. For the OER to occur on RuO_2 a potential of 1.65V is needed since that is the largest difference

in binding energies. The excess potential, compared to thermodynamic equilibrium potential, which is required to force the all the intermediates downhill in energy is called the overpotential for the OER.
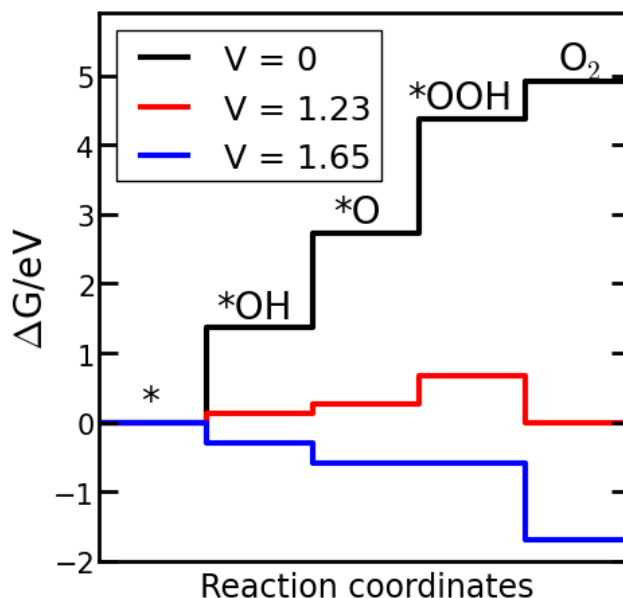
Figure 2.3: The free energy diagram for the OER on rutile RuO$_2$ at three different potentials to illustrate the concept of the overpotential. At no applied potential (black) and the equilibrium potential (red) there are still intermediates that are uphill in energy. The overpotential is the excess potential required to have a downhill reaction (blue).

It should be noted that for the ORR the goal is to obtain the smallest potential difference between the thermodynamic equilibrium potential and the operating potential and still have a downhill reaction. Here, the lowest reaction energy will be the potential limiting step.

Using this approach, no solvent effects are taken into account unless explicitly done so in the calculation by adding water molecules which is not done in this work. However, to fully model the electrochemical interface between electrolyte and catalyst surface is not within the scope of this project and it is far from trivial. Therefore, one has to keep in mind that the goal for theoretical design of catalysts is not necessarily to match the experimental properties as long as the trends in activity is captured and the fundamental properties of the catalysts can be determined. In this work, only the thermodynamic part of the overpotential is considered and since the intermediates that are studied for the OER and ORR do not have a sufficient dipole moment to interact with the electric field or the water structure the energies should not vary with pH. Kinetics and reaction barriers are a different problem entirely as is still not fully understood how these vary with the potential [38] and is not dealt with in this framework.

3 Theoretical oxygen electrocatalysis

This section will give a brief overview of the theoretical advances within oxygen electrocatalysis meaning both the ORR and the OER. The concept of the scaling between intermediates in electrocatalysis will be explained and how these scaling relations can influence the minimum theoretical overpotential. Experimental findings are included to further expand the understanding of the oxygen electrocatalysis and to support the theoretical advances.

3.1 Oxygen reduction reaction

Oxygen electrocatalysis is the focus point of this thesis. Oxygen electrocatalysis is the conversion between water and O_2 either by using electricity to split water into hydrogen and oxygen gas or producing electricity from the hydrogen and oxygen gas reaction into water:

$$H_2O \leftrightarrow H_2 + \frac{1}{2}O_2 \qquad\qquad 3.1$$

The water splitting is endothermic and is a complicated process which involves the removal of protons and an O-O bond formation. The potential required to split the water molecule is in principle only 1.23V but as mentioned in the introduction there are several loss mechanisms which lead to a large overpotential. For the reverse reaction there is also an overpotential which limits the potential a fuel cell can produce. A large part of the overpotential is due to what is typically called the "slow or sluggish kinetics" of the ORR or OER [39][40][41].

It is also possible to form H_2O_2 as a final or intermediate product when reducing O_2. Here the main focus is on the full 4 electron conversion between O_2 to H_2O.

The overpotential associated with ORR has been shown to be at least partly thermodynamic in nature using computational studies. The origin of the overpotential [42] for the ORR was explained by looking at various transition metals and observing a linear scaling between the binding of the involved intermediate as a function of the transition metal surface. Two mechanisms were discussed in this framework; the dissociative and the associative mechanism.. The active site on the metal is denoted by an asterisk (*) in the reaction mechanism for the ORR which is listed below. It involves 4 coupled proton and electron transfers. In the dissociate mechanism the O-O bond breaking occurs during the initial adsorption of O_2:

$$\tfrac{1}{2}O_{2\,(g)} + * \rightarrow *=O \qquad\qquad 3.2$$

The individual *=O intermediates are then reduced to H_2O separately using an electron and a proton transfer.

$$*=O + H^+ + e^- \rightarrow *\text{-}OH \qquad\qquad 3.3$$

$$*\text{-}OH + H^+ + e^- \rightarrow * + H_2O \qquad\qquad 3.4$$

To convert a full O_2 molecule requires 4 electron and protons as shown in 3.2-3.4.

In the associative mechanism the O-O bond splitting is separate from the initial binding of O_2. Instead, a proton is adsorbed forming a peroxide intermediate which is then attacked by a proton forming water and the *=O intermediate.

$$O_{2\,(g)} + H^+ + e^- * \rightarrow *\text{-}OOH \qquad\qquad 3.5$$

$$*\text{-}OOH + H^+ + e^- \rightarrow *=O + H_2O \qquad\qquad 3.6$$

$$*=O + H^+ + e^- \rightarrow *\text{-}OH \qquad\qquad 3.7$$

$$*\text{-}OH + H^+ + e^- \rightarrow * + H_2O \qquad\qquad 3.8$$

The associated binding energies of *-OH, *=O and *-OOH can be calculated using the computational hydrogen electrode:

$$G_{OH} = G_* + G_{H_2O} - \tfrac{1}{2}G_{H_2} \qquad\qquad 3.9$$

$$G_O = G_* + 2G_{H_2O} - G_{H_2} \qquad\qquad 3.10$$

$$G_{OOH} = G_* + {}^3\!/_2\, G_{H_2O} - G_{H_2} \qquad\qquad 3.11$$

If the binding energies of the intermediates are calculated using the same reference surface. The individual reaction energies can be obtained:

$$\Delta G_1 = G_{OH} \qquad\qquad 3.12$$

$$\Delta G_2 = G_O - G_{OH} \qquad\qquad 3.13$$

$$\Delta G_3 = G_{OOH} - G_O \qquad\qquad 3.14$$

$$\Delta G_4 = G_{O_2} - G_{OOH} \qquad\qquad 3.15$$

For the ORR the overpotential is then the equilibrium potential (1.23 eV) minus the minimum of the individual reaction energies.

This relatively simple approach correctly observed Pt, Pd and Ir that are good catalysts for the ORR which is also observed experimentally. The correlation between theoretical and experimental findings verifies the procedure and this marked the beginning for the describing oxygen electrocatalysis using DFT [42].

Even the best catalysts for the ORR have an overpotential associated with them limiting the overall activity. The cause of the overpotential was later attributed to the a constant offset of 3.2 eV between the binding of *OH and *OOH which is universal for metals, alloys [43] and oxides [37] with a single active site as seen in Figure 3.1. This universality of the linear scaling relations in electrocatalysis is also present in heterogeneous catalysis and can also limit the activity of heterogeneous catalysts in various reactions [44].
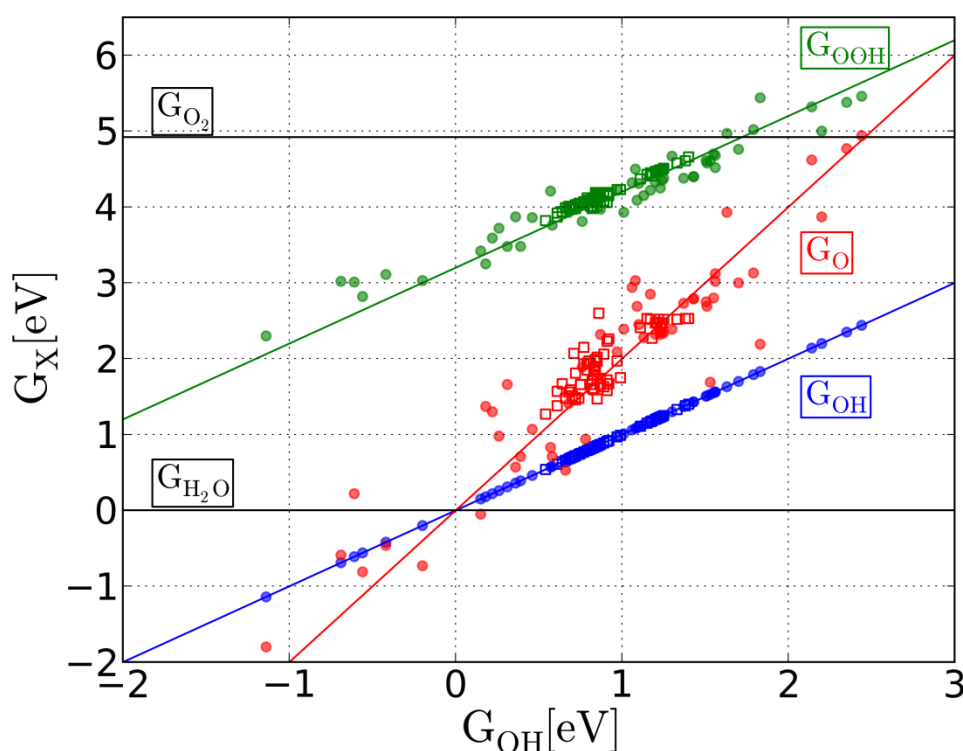
Figure 3.1: Scaling relation for the binding of *OH, *O and *OOH as a function of the binding of *OH for numerous materials. The squares represent binding energies found on metals and alloys [43] and the circles represent binding energies found on oxides [37]. Here $G_{OOH} = G_{OH} + 3.2eV =$ and $G_O = 2G_{OH}$ relative to H_2O and O_2.

The lines in Figure 3.1 are estimations of the binding energies of *=O and *-OOH using the assumptions that $G_O = 2G_{OH}$ and $G_{OOH} = G_{OH} + 3.2eV$. As all the energies are calculated as a function of the binding of G_{OH} for each electrocatalyst a single

catalyst is represented by three horizontal data points which ideally should be found on the lines. While there are some scatter from the first assumption the second assumption is more reasonable. As there are two coupled proton and electron transfers between these two intermediates the ideal value would be 2.46 eV as the thermodynamic equilibrium potential for the water formation from hydrogen and oxygen gas is 1.23V. The linear scaling relations between *-OH and *-OOH is as observed 3.2 eV which means that an overpotential of around 0.4V is seemingly unavoidable for both the ORR and the OER due to the linear scaling relations. For the ORR the offset means that the potential limiting step in most cases is either the initial binding of O_2 forming *-OOH or the final step which is the second release of H_2O. The theoretical overpotential is determined by taking the equilibrium potential of 1.23 V and subtracting the binding energy of the potential limiting step. These linear scaling relations between intermediates involved in a catalytic reaction are a fundamental and universal property of materials. The implications of the linear scaling relations between intermediates should not be undervalued as they are a major source of the overpotential which limits the efficiency of oxygen electrocatalysis and its use in more sustainable energy production and conversion. The linear scaling relations between intermediates are not only relevant for this work but for heterogeneous and electro catalyst design in general[44], [45].

The scaling relations between intermediates give the simple approach of using DFT calculations to determine the binding energies of energies predictive power in oxygen electrocatalysis without having to consider other effects of the electrochemical interface. Recently it has been demonstrated that these linear scaling relations are more accurately described by DFT than the individual binding energies by utilising the error estimations capability of the BEEF-vdW exchange-correlation functional for ammonia synthesis [46].

The binding energies of different intermediates on an active site on metal surfaces can be correlated to the local electron density using d-band model [47].

The d-band model can also be used to explain the increase in activity of platinum alloy nanoparticles why there is a difference in activity of bulk Au which is noble and small Au nanoparticles which are more reactive [48] and why kinks and steps sites on metal surfaces binds stronger than the active sites on terraces [49].

Pt based alloys with more reactive metals such as Y [50], Ga [51], Cu [52] Co and Ni [53] that dealloy under ORR conditions. This result in either a platinum skin or skeleton structure with a compressed lattice [54]. As a result of the compressed lattice the d-band centre will be shifted downwards giving a weaker binding of

intermediates which is required for a better ORR catalyst [50]. Ligand effects (neighbouring atoms being different elements) can also be explained using the d-band model [55]. However, the ligand effect have not been directly coupled to the increase in activity of ORR catalysts but it is an important factor for other catalysts for different reactions such as the binding of CO on overlayers of Pd on Ru surfaces[56] and Pt on Au [57]. The ligand and stress effects can be difficult to decouple unless, as in the case of the Pt skin structure on Pt alloy nanoparticels, the overlayers are quite thick which makes the ligand effect much less likely to be important for catalytic activity.

Core-shell nanoparticles are interesting candidates for the ORR. It lessens the amount of precious metal required and also induces strain. A Pt-alloy with a more reactive metal such as Cu or Ni is dealloyed which form a core-shell nanoparticle with a strained Pt shell that covers the remaining bimetallic alloy and offer some protection from further dealloying. Using different compositions of the initial alloy and different preparation methods the lattice strain of the core-shell nanoparticle can be tuned to some extent [52][58].

Oxides are also considered as potential candidates for the ORR but currently they are less investigated than metals. When studying the oxides for the ORR activity the studies are mostly performed in alkaline solution. IrO_2[59] and RuO_2[60] has been investigated and found to a have a similar activity as Pt (onset potential of 0.8V vs. RHE for IrO_2 in acidic conditions in a more recent study[61]) . However, they are more expensive than Pt.

Perovskites have also been investigated as ORR catalysts[62] although the primary focus was OER. $LaMnO_3$ was identified as a near optimal catalyst for the ORR using the e_g electron filling as a descriptor. Other oxide systems such as spinels[63], [64] and pyrochlores[65] have been tested experimentally for their ORR activity. However, there have so far been no attempts to determine the binding energies of intermediates by DFT of the previously mentioned oxides.

An alternative to metals and metal oxides are more bioinspired catalysts based on porphyrines. Porphyrines are a class of heterocyclic organic compounds which can function as a ligand for a metal ion. The single metal in the porphyrine is coordinating to 4 N atoms in the porphyrine. The use of porphyrines and similar materials as ORR catalysts could be seen as an attempt to mimic nature. For instance the heme group in haemoglobin is a Fe porphyrine which is used to transport O_2 in the blood. In the ORR some porphyrines with Ir[66] and Co[67] are considered as potential candidates to replace Pt but compared to metallic nanoparticles they are less investigated. While Ir is more expensive than Pt the

single site nature of the porphyrines allow for maximum utilisation of the precious metals unlike nanoparticles where only the surface is active thus minimising the amount of precious metal required.

Computational studies using DFT studied porphyrine based molecules[68] and have been shown to have similar issues with the scaling between intermediates as metal and metal oxides as the binding of *-OH and *-OOH was seen to have a constant offset of around 3. A Co based porphyrine was observed to have an almost near the apex of the volcano for the ORR.

A periodic system with porphyrine like character has also been explored with DFT[69]. The study concluded that the best of these systems dubbed functionalised graphitic materials are based on Ir, Co and Fe. Porphyrines have also been investigated as potential H_2O_2 producing catalyst[70]. The single site nature of these catalysts is proposed as reason for not reducing O_2 fully to H_2O combined with a good binding *-OOH for optimum efficiency[71].

The problem with the porphyrine based catalysts is synthesis however porphyrine like active sites have been on carbon nanotubes and such a structure carbon nanotube decorated with a porphyrine active site coordinating with Fe have been reported to have a lower overpotential and better stability than Pt/C with the only product being H_2O [72].

3.2 Oxygen evolution reaction

The OER or water oxidation is in principle the ORR run in reverse. However, catalysts which are excellent for the ORR are not great OER catalysts. It should also be noted that the potential required for OER is higher than ORR so many ORR catalysts are not stable in the potential region in which oxygen evolution occurs.

While metals have been investigated for the oxygen evolution reaction[73][74] and found that Ir and Ru are amongst the best catalysts it is generally accepted that they will form thin surface oxides [75][76] due to the large potential required for OER which are responsible for the catalytic activity. Theoretical studies have shown that even the most noble metal, Au, is oxidised under oxygen evolution reaction conditions and it is a surface oxide of Au which decomposes to form O_2 [77].

DFT studies [37] have shown that the 110 surface of rutile oxides, the noble oxides RuO_2 and IrO_2 are amongst the most active OER catalysts and located near

the apex of the OER volcanos shown on Figure 3.2 due to near optimal binding energies. The observation that RuO_2 and IrO_2 are excellent catalysts for the OER is in excellent agreement with experimental findings as RuO_2 and IrO_2 together with TiO_2 are part of the catalyst material on the commercial DSA® (dimensionally stable anode) [78]. This catalyst is one of only stable catalysts for the OER in PEM water electrolysers. Here the descriptor selected is the difference in binding energies between *O and *OH, i.e. the energy of the second coupled proton electron transfer in the OER mechanism. Due to the scaling relation between *OH and *OOH this single descriptor is able to describe oxides where the potential limiting step is breaking bonds to the surface, *O →*OOH, and oxides where the potential limiting step is forming bonds to the surface *OH→*O. At the same time it describes the limits set by the scaling relations and shows that the optimal reaction free energy of the second reaction step is about 1.6 eV which is significantly higher than the 1.23 eV it would be, if there were no scaling between intermediates. The overpotential is determined by first finding the potential limiting step which in this case of the OER is the largest of the reaction energies and then subtracting the equilibrium potential of 1.23V.
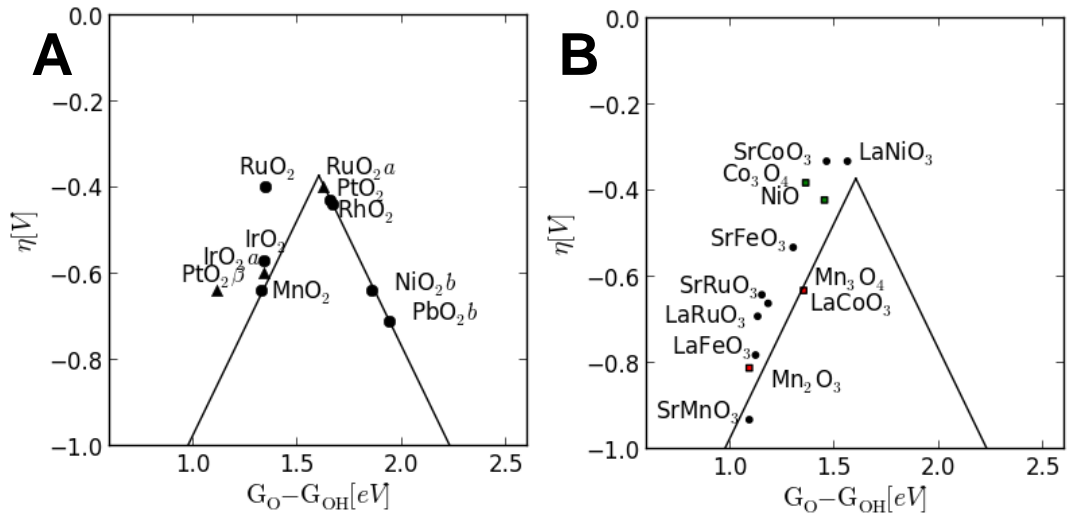
Figure 3.2: Volcano plots for the oxygen evolution reaction. A) displays rutile and anatase denoted by an (a) oxides. The structure of PtO$_{2\beta}$ is a slightly distorted rutile. The b means that the catalytically active site is a vacancy in the bridging row. B) displays perovskites and a few other oxides. The figure is adapted from [37]

The cause of the minimum theoretical overpotential as seen on the volcanos in Figure 3.2 is due to the linear scaling relations between the intermediates. The theoretical overpotential has the same magnitude for the ORR as the same intermediates are involved. The data for the OER catalysts are somewhat

scattered around volcano plots since the binding energies of some catalysts does not obey the linear scaling relations between intermediates as seen in Figure 3.1. However, the trends in activity amongst oxides is well predicted and the theoretical overpotential is linearly correlation with the actual observed overpotential [37].

Oxides, unlike metals which follow the trend that $G_O = 2G_{OH}$, have a larger degree of uncertainty associated with the binding of O to the surface. This can be explained in terms of oxidation states. In DFT, an unlikely or unstable oxidation state will result in a higher than expected binding energies and very stable oxidation state will result in lower binding energy. Two examples are NiO and CrO_2 which are displayed in Figure 3.3. These two compounds are highlighted as an examples of compounds that deviate considerably from the $G_O = 2G_{OH}$ assumption.
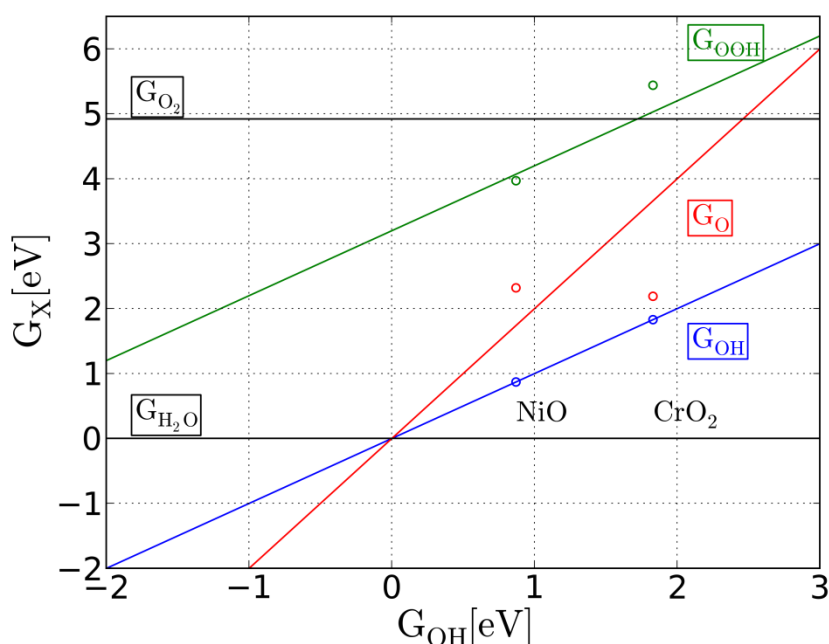
Figure 3.3: Scaling relations for G_{OH}, G_O and G_{OOH} for two select oxides, NiO and CrO_2 to highlight two examples of the uncertainty in the binding of O to the surface.

For NiO the binding of O is weak compared to the scaling relation while the binding of OH and OOH follow the linear scaling relations. However, the binding of O to NiO result in an unstable oxidation state which result in a higher than expected binding energy.

Ni based catalysts are great catalysts for the oxygen evolution in alkaline solution. High activity of amorphous Ni, Co and Fe oxides has been reported[79] and of their hydr(oxy)oxides [80].

CrO_2 is a very poor catalyst for the OER as predicted with DFT and there are no experimental studies reporting any activity towards the OER for this system. It is very likely unstable as the Cr is very oxophilic in the rutile structure which is seen by the strong binding of O compared to the scaling relations in Figure 3.3 meaning that Cr will probably oxidise further and dissolve.

Oxides, nitrides and sulfides have a similar linear scaling relationship for adsorption energies as metals [81]. This is seen in Figure 3.1 which has data from both metals and oxides. This seems to suggest that a modified d-band model could exist for oxides. A modified d-band model has been proposed for transition metal carbides, however this has only been done for a single type of crystal structure in the NaCl structure [82]. There is still need much work to be done before we can obtain a general model to correlate the binding of adsorbates on oxides with the electronic structure.

As mentioned previously, RuO_2 and IrO_2 are amongst the only catalysts that are suitable for water electrolysis in acidic solution[76] since they have close to optimal activity approaching overpotentials of 0.4 V and are somewhat stable, especially IrO_2. In alkaline solution, perovskites and double perovskites[62][83][84] and other cheaper oxides such as NiO and Co_3O_4 have similar activities as noble metal oxides. For the perovskites the trends are well reproduced with DFT however the absolute activities can be debated. Another observation is that there seem to be no volcanic trend for the perovskites as all the decent catalysts with a theoretical overpotential lower than 1V are found on the left side of the volcano. Experimental work on perovskites[85] show that a perovskite ($Ba_{0.5}Sr_{0.5}Co_{0.8}Fe_{0.2}O_{3-\delta}$) can be designed specifically for high activity towards oxygen evolution and outperform all other perovskites considered using molecular orbital theory and the e_g electron filling as a descriptor. The trends in activity is preserved but a simple relation between the e_g electron filling and the binding energies obtained from DFT has not been identified. For the double perovskites the descriptor for activity was the O p-band relative to the Fermi level and identified the double perovskite $Pr_{0.5}Ba_{0.5}CoO_{3-\delta}$ as excellent OER catalysts in alkaline solution.

The perovskite and the rutile structure have well-defined and not too complicated surface terminations which is great for DFT calculations. Oxides such as Fe_2O_3, Co_3O_4 and NiO have a more complicated structure under OER conditions. While NiO is simulated as the rocksalt structure by [37] a much more complicated structure based on NiOOH is supposed to be more accurate and proposes an active surface with a reasonable overpotential which can lowered even further by Fe doping [86]. This doping effect also works in reverse as

hematite, a crustal structure of Fe_2O_3, can be improved slightly by Ni and Co doping [87]. Cobalt oxides has also been investigated in greater detail using a CoOOH structure based on a calculated Pourbaix diagram and it was found that the activity was overestimated using standard DFT with the RPBE exchange-correlation functional [88],[89].

The three studies mentioned above all used DFT+U [90] which is a method that introduces a parameter U_{eff} to explicitly localise electrons to avoid the self-interaction error. The U correction is usually applied to systems with for unfilled d and f orbitals as valence d and f electrons are notoriously difficult to treat with standard DFT. However, care must be taken when selecting the U_{eff} parameter. Usually the U_{eff} parameter is selected to match a bulk property such as formation energies of varies relevant oxides as suggested by Ceder and others[91] or it can be determined from linear response theory[92] but there is no real consensus on how to select U_{eff}. In principle the U_{eff} will depend on the oxidation state and the local environment which makes adsorption energies particularly tricky to calculate with DFT+U and interpret. Using different U_{eff} for different oxides means that you also are using a different functional for each oxide system and in that case DFT loses it predictive power.

Theoretical design of catalysts makes no sense without predictive power and there is even reason to doubt the experiments as well. First of all there has been a lack of proper benchmarking which makes comparison of different catalysts problematic until the community decides to use a proper benchmarking procedure which is cumbersome [93]. What further complicates activity studies is the lack of focus on stability and although these two properties are certainly entangled and difficult to decouple. It has been proposed that the dissolution from the initial sweep from 1.23V to a potential where a current density of 5 mA/cm^2 is reached should be used as a stability descriptor [53]. With such a procedure OsO_2 was proposed as the best catalysts for the OER in terms of activity alone, however OsO_2 lacks the stability and RuO_2 and IrO_2 was identified as the best compromise between activity and stability.

Another and possible better descriptor for the stability could be to monitor the mass loss during the OER using a electrochemical quartz crystal microbalance to monitor the mass loss of the catalysts with inductively coupled plasma mass spectrometry which measured the content of the electrolyte. It is concluded that stability tests based on electrochemical measurements are insufficient [94].

The stability-activity-cost relation is key for designing any potential new OER catalyst. To reduce cost, one tactic could be to reduce the loading of the

expensive OER materials while retaining activity. Very recent studies suggest that nanoparticles of RuO_2 can be stabilised using a proper pre-treatment such as thermal oxidation. This enables smaller particles to be effective catalysts. Interestingly, not only were the nanoparticles stabilised but gained a 45-fold increase in activity [95].

IrO_2 is more stable than RuO_2 but also more expensive however core-shell nanoparticles or other high surface area structures could lessen the amount of iridium needed for making a sufficiently stable and active oxygen evolution catalyst. This approach is not as developed as the Pt core-shell nanoparticles for the ORR but core-shell nanoparticles of IrO_x have been synthesised recently [96]. Ir and Ru based catalysts are hardly cost-efficient no matter how active they are. In this respect core-shell nanoparticles with a shell of Co3O4 encasing Au seem promising [97].

Another approach could be to increase the active site density as observed on rutile RuO_2 and IrO_2 when comparing the 100 and 110 surface. The 100 surface has a higher density of active sites but is not the thermodynamically stable surface. It is sufficiently stable to be synthesised and to work as an oxygen evolution catalysts in alkaline medium [98].

While stability is important for designing proper oxygen evolution catalysts it is beyond the scope of this thesis to understand corrosion processes under OER conditions.

The ideal OER catalysts would not consists of IrO_2 and RuO_2 and would be stable and active in acid solution using only abundant materials. Plants and other organisms convert sunlight into energy and use it to reduce CO_2 to hydrocarbons. In this process water oxidation is the other half reaction and as plants are limited to abundant materials it is of particular interest that the active site of photosystem II the so-called, oxygen evolution center (OEC), contains a cluster of four manganese and a calcium atom [99]. A striking feature compared to most catalysts is its ability to oxidise water in neutral pH. However, millions of years of evolution has not been able bypass the overpotential limit set by the universal scaling relation as the overpotential for photosystem II is reported to be around 0.3-0.4V towards OER [100][101].

Mimicking plants may not be a viable option for industrial water electrolysers due to stability issues. While the water oxidation occurs at the OEC the surrounding protein ligands which hold the Mn_4Ca cluster in place get photodamaged and have to be replaced as frequently as every 30 min for some organisms meaning that the plants have to reinvest a lot of energy to repair

photosystem II which limits the overall efficiency [102]–[104]. Biomimetic inorganic catalysts for OER have been reported but the catalysts are more aimed at photochemical water oxidation [105]–[107]. While there are many identical challenges for photochemical and electrochemical water oxidation comparing the catalysts activity is not trivial but there is common ground if one adjusts to the fields terminology [108].

With a self-healing mechanism unstable catalysts might be relevant for oxygen evolution. Several catalysts have been found to have regenerative properties. In these catalysts such as nickel borate [109], CoPi, which is a cobalt phosphate catalyst [110], the self-healing process is due to interchangeability of anions in the catalysts and the same type of anions in the electrolyte during potential cycling. Here it is possible perform the OER while slowly dissolve the catalysts. The potential can then be decreased to facilitate the regenerative mechanism restoring the catalyst. It also enables the inherently unstable MnO_x can function in acid if a redeposition is introduced at potentials below the potential at which OER occur [111].

3.3 Consequences of the linear scaling relations

The fundamental problem of the overpotential being limited by the universal scaling relations is still an issue that has to be addressed. This is especially important when discussing the so-called bifunctional catalysts which are designed to function for both the ORR and the OER. The linear scaling relations between the three intermediates, *-OH, *=O and *-OOH makes it impossible for a single active site to catalyse both the ORR and the OER efficiently as the binding energies of intermediates cannot be tuned individually. This is illustrated on Figure 3.4 where the binding energies of the intermediates in ORR and OER of Pt, the best pure metal for ORR, and binding energies of the same intermediates for rutile RuO_2 which is one of the most active oxide for OER, together with the binding energies of two hypothetical catalysts which has the best possible binding energies for the ORR and the OER respectively and still obeys the scaling relations $GO = 2*G_{OH}$ and $G_{OOH} = G_{OH} + 3.2$. For the ORR the optimal ORR catalyst have a binding of *-OH equal to 1.23-0.37 = 0.86 eV and the optimal OER catalyst has a binding of *-OH equal to 1.23+0.37 = 1.6 eV. The 0.37 eV represent the excess energy obtained from the theoretical overpotential due to the linear scaling relation between intermediates. This positions the best possible ORR and OER catalysts far away of the hypothetical ideal catalyst which is not limited by scaling relations between intermediates. This catalysts will have no overpotential meaning all coupled proton and electron transfers (G_1,G_2,G_3,G_4) equal 1.23 eV.
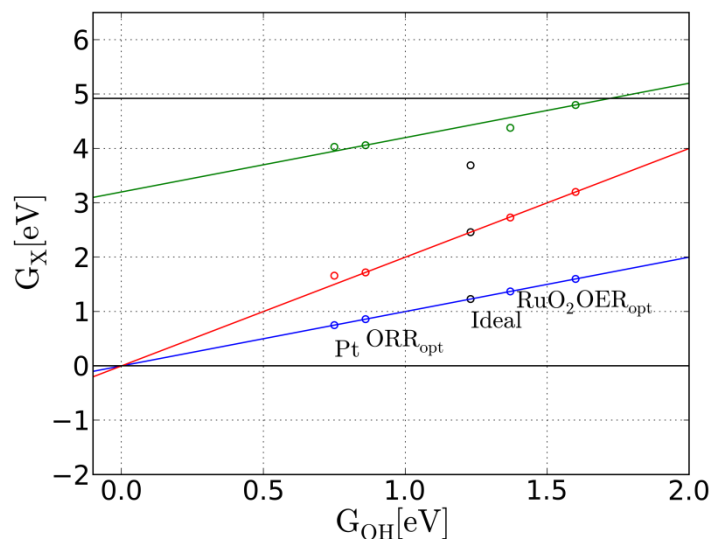
Figure 3.4: The theoretical linear scaling relations between G_{OH}, G_O and G_{OOH} for selected catalysts. Here Pt and RuO$_2$ is compared to the hypothetically optimal ORR and OER catalysts which still obeys the linear scaling relations. The ideal catalyst is shown for comparison which for an active site which obeys the scaling relations is not possible.

The linear scaling relations between intermediates are responsible for the fact that the same active site cannot be optimal for both ORR and OER. However many oxides systems have the possibility of having different adsorption sites for intermediates and/or different surface compositions at different potentials. As an example the spinels have been investigated as bifunctional catalysts [63]. These catalysts are reported to have defects and the number of defects and oxygen vacancies probably varies with the potential. And these defects have different O$_2$ binding energies calculated with DFT so in principle different defect sites could be responsible for OER and ORR. This could also be the case for other complicated oxide systems such as the double perovskites[83]. However the catalysts investigated so far as bifunctional have not reported significantly better activities than Pt for the ORR and RuO$_2$ or IrO$_2$ for the OER and usually the bifunctional catalysts have a superior activity towards either ORR or OER [63][112][113].

4 Beyond the scaling relations

This section here summarised the effort made in paper 1 and paper 2 which are part of this thesis. The results obtained in the papers are two concrete examples of how the universal scaling relations for the intermediates in the OER [37] can be avoided. The first part deals with the concept of the H transfer mechanism on RuO_2 modified with either Ni or Co as a proof of concept. The second part details how the H transfer can explain the beneficial interaction between Au and transition metal oxides such CoO_x and MnO_x which result in higher OER activities compared to the bare oxides.

4.1 Ni and Co modified RuO_2

The OER mechanism is investigated on Ni and Co modified RuO_2. The mechanism for the OER that is considered is the associative mechanism which involves the formation of the peroxide intermediate (*-OOH) described previously in section 3.1 assuming acidic conditions.

$$* + H_2O \rightarrow \text{*-OH} + H^+ + e^- \qquad\qquad 4.1$$

$$\text{*-OH} \quad \rightarrow *{=}O + H^+ + e^- \qquad\qquad 4.2$$

$$*{=}O + H_2O \quad \rightarrow \text{*-OOH} + H^+ + e^- \qquad\qquad 4.3$$

$$\text{*-OOH} \rightarrow *{+}O_{2(g)} + H^+ + e^- \qquad\qquad 4.4$$

For RuO_2 the potential limiting step is the 3rd step (equation 4.3) [37] which is the formation of the peroxide intermediate. In principle many ways of stabilising the *-OOH intermediate relative to the *-OH could be investigated. One idea is to functionalise the surface so that the larger *-OOH can reach an electronegative region of the catalyst for increased stability. In the extreme case the *OOH could split into O_2 and H which adsorb on two different sites. A secondary site on an oxide surface which can fully adsorb hydrogen from the peroxide intermediate splitting the *-OOH into. In this case the scaling relations between *-OH and *-OOH can be avoided entirely.

Experimental work with RuO_2 demonstrated that introducing Ni or Co into the rutile RuO_2 matrix did not change the overall structure of the catalyst too much as NiO forms clusters within the rutile RuO_2 matrix or lines of NiO if the molar concentration of Ni is above 0.1 thus forming a clear phase separation between

the two oxides. A proposed structure based on Extended X-Ray Absorption Fine Structure (EXAFS) studies is shown in Figure 4.1.
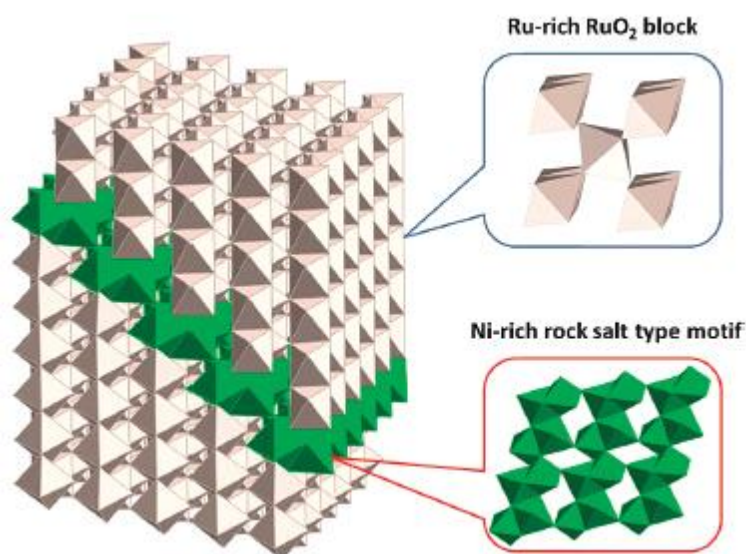

Figure 4.1: A model of the mixed Ru Ni oxide which shows the non-mixing of RuO_2 and NiO Figure is obtained from[114]**.**

The activity towards OER on the modified RuO_2 is increased compared to the bare RuO_2 [115][116][114] which contradicts the volcano analysis based on the universal scaling relations in the oxygen evolution reaction which places RuO_2 at the very top with little to no possibility for improvement in terms of overpotential [37].

To model the influence on Ni insertion into the matrix of RuO_2 using density functional theory a model system of sufficient simplicity was created. The 110 surface of rutile RuO_2 was selected as it is the most stable surface of rutile structure and has been used in previous studies [37]. The surface consists of two distinctly different types of surface sites. The coordinatively unsaturated sites (cus) which are the active sites as they only coordinate to five O atoms instead of the six in bulk RuO_2. The bridge sites are called so due to the bridging O atoms which are exposed on the surface which only coordinate to two Ru atoms instead of three which is what is found in the bulk. A slab was created from a 1x3 supercell which were 4 atomic trilayers thick. To understand the influence of the Ni and Co insertion in RuO_2 two atoms of Ru on the surface was replaced with Ni or Co. One Ni/Co was placed in the cus position and one Ni/Co just below a bridging O creating the modified RuO_2 model system. Vacuum was added to this slab to avoid interactions between periodic images.

This doped system is used as a model system for the experimentally prepared Ni and Co modified RuO_2 catalysts. A model of the system is shown in Figure 4.2. At potentials relevant to oxygen evolution the RuO_2 will be covered by O and the Ni in the cus position is assumed to be inert. The binding energies from the conventional RuO_2 are obtained from literature [37]. The structure of conventional RuO_2 has identical thickness and surface orientation as the model system of Ni and Co modified RuO_2 however the supercell is only 1x2. For the modified RuO2 the calculations were spinpolarised by providing an initial magnetic moment for Ni or Co and allowing the magnetic moments to relax during optimisation.
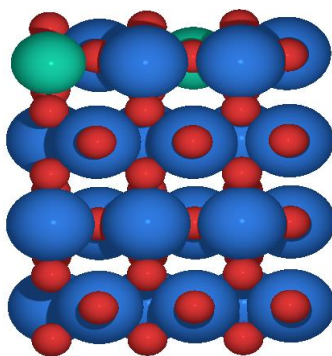
Figure 4.2: Model system of the Ni modified RuO_2. An identical model system for Co modified RuO_2 was used. Color code: Blue - Ru, Green - Ni, O - red.

In order to break the constant scaling of 3.2eV between the two key intermediates OH and OOH in the mononuclear mechanism the binding of one intermediate must be drastically different than the other. The two bridging O near the Ni in the bridge position are highly active and reducible and in combination with the cus Ru creates a local structure with high activity due to a change in mechanism. The cus Ru atom is the usual active site for rutile oxides. In Ni and Co modified RuO_2 the cus Ru adsorbs O containing species and the bridging O next to the transition metal (either Ni or Co) adsorbs H. In this case *OH and *OOH never form on the surface and instead O and O_2 form on the Ru cus site and H adsorbs on the bridging O and this is cause for the increase in activity compared to conventional RuO2 as the scaling between *-OH and *-OOH is bypassed by never forming these species on the surface. The one site mechanism with the * denoting the Ru cus site (associative mechanism) is shown below and is compared the new mechanism based on two active site the Ru cus site for O containing species *, and bridging O for H containing species denoted x.

$* + H_2O \qquad \rightarrow *\text{-}OH + H^+ + e^-$ 4.5

$* \, x + H_2O \qquad \rightarrow *=O \, x\text{-}H + H^+ + e^-$ 4.6

$*\text{-}OH \qquad\qquad \rightarrow \; *=O + H^+ + e^-$ 4.7

$*=O \, x\text{-}H \qquad \rightarrow \; *=O \, x + H^+ + e^-$ 4.8

$*=O + H_2O \qquad \rightarrow *\text{-}OOH + H^+ + e^-$ 4.9

$*=O + H_2O \qquad \rightarrow *\text{-}O_2 \, x\text{-}H + H^+ + e^-$ 4.10

$*\text{-}OOH \qquad\qquad \rightarrow * + O_{2(g)} + H^+ + e^-$ 4.11

$*\text{-}O_2 \, x\text{-}H \qquad \rightarrow * \, x + O_{2(g)} + H^+ + e^-$ 4.12
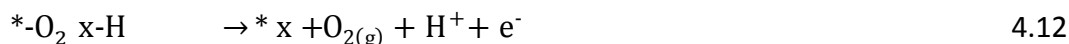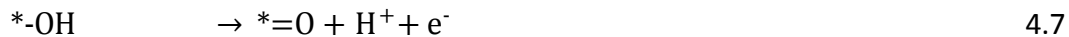
This two site mechanism based on the activated bridging O next to either Ni or Co was proposed based on the calculations of the binding energies of the intermediates in each reaction step. The results are collected in Table 4-1 using two different DFT implementations; Dacapo and GPAW. All energies are referenced to water and a reference oxide surface. This reference serves is covered with O on the cus and bridge sites except the vacancy on the active site. which serves as the active site for oxygen containing intermediates in the OER mechanism. In order to stay consistent with literature[37], [117] only the binding energies for Dacapo will be used for further analysis.

Table 4-1: Adsorptions energies for regular RuO_2 and Ni and Co modified RuO_2 with determination of the potential limiting step and the associated theoretical overpotential with two different DFT implementations, Dacapo and GPAW.

	Energies calculated using Dacapo			Energies calculated using GPAW		
	RuO_2	Ni modi. RuO_2	Co modi. RuO_2	RuO_2	Ni modi. RuO_2	Co modi. RuO_2
$\Delta G_{H^{\#}*}$ (eV)	--	-1.33	-1.23	--	-1.19	-1.18
$\Delta G_{H^{\#}O*}$ (eV)	--	1.26	1.33	--	1.01	0.96
ΔG_{HO*} (eV)	1.37	1.37	--	1.25	1.24	1.09

	RuO$_2$	Ni modi. RuO$_2$	Co modi. RuO$_2$	RuO$_2$	Ni modi. RuO$_2$	Co modi. RuO$_2$
ΔG_{O^*}(eV)	2.73	2.75	2.59	2.34	2.29	2.19
	Energies calculated using Dacapo			Energies calculated using GPAW		
	RuO$_2$	Ni modi. RuO$_2$	Co modi. RuO$_2$	RuO$_2$	Ni modi. RuO$_2$	Co modi. RuO$_2$
$\Delta G_{H^\#OO^*}$(eV)	--	3.57	3.62	--	3.68	3.61
$\Delta G_{(H^{\#*}+O_2(g))}$(eV)		3.59	3.69		3.73	3.74
ΔG_{HOO^*}(eV)	4.38	4.45	---	4.11	4.27	4.06
Potential limiting step	O^* $\rightarrow HOO^*$	$H^\#O^*$ $\rightarrow O^*$	$^\#{}^*$ $\rightarrow H^\#O^*$	O^* $\rightarrow HOO^*$	O^* $\rightarrow H^\#OO^*$	O^* $\rightarrow H^\#OO^*$
Theoretical overpotential (V)	0.42	0.26		0.54	0.16	0.18

The key to reduce the binding of *-OOH by such a large degree is the almost ideal binding energy of H on the bridging O next to the Ni and Co. In order to maximise the efficiency of the hydrogen transfer mechanism the adsorption of H should be around the equilibrium potential of the reaction in consideration and the H adsorption or desorption should be potential limiting. Ideally, this will change the potential limiting step, in this case from the formation of *-OOH to another step in the reaction mechanism. This will reduce the adsorption energy considerably depending on the remaining reaction energies. In this particular case the H adsorption energies are found to be 1.33 eV and 1.23 eV for Ni and Co modified RuO$_2$ respectively. This is also seen in Table 4-1 by removing the contribution from O$_2$ (4.92eV) for the $\Delta G_{(H^{\#*}+O_2(g))}$ binding energy.

The reaction mechanism for Ni and Co modified RuO$_2$ is very similar to the RuO$_2$ the only difference being that *-OH and *-OOH do not form on the surface. Instead, these intermediates split into *=O and *-O$_2$ and an H which adsorb on a bridging O forming x-H. The mechanism is visualised on Figure 4.3 starting from a clean surface S$_0$, adsorbing OH from H$_2$O which splits into *=O and x-H in S$_1$, removing the proton from the bridging O in S$_2$, adsorbing another H$_2$O forming *-O$_2$ and x-H in S$_3$. The O$_2$ desorbs which is not an electrochemical step forming S$_{3a}$ after which the H is removed completing the catalytic conversion of 2 H$_2$O into O$_2$. Since there are issues with O$_2$ in DFT the S$_3$ state might be a concern. In this

case it is not, as the binding energies of the states, S_3 and S_{3a} plus the free energy of an O_2 molecule are very similar as seen in Table 4-1 (3.59 eV vs. 3.69eV).
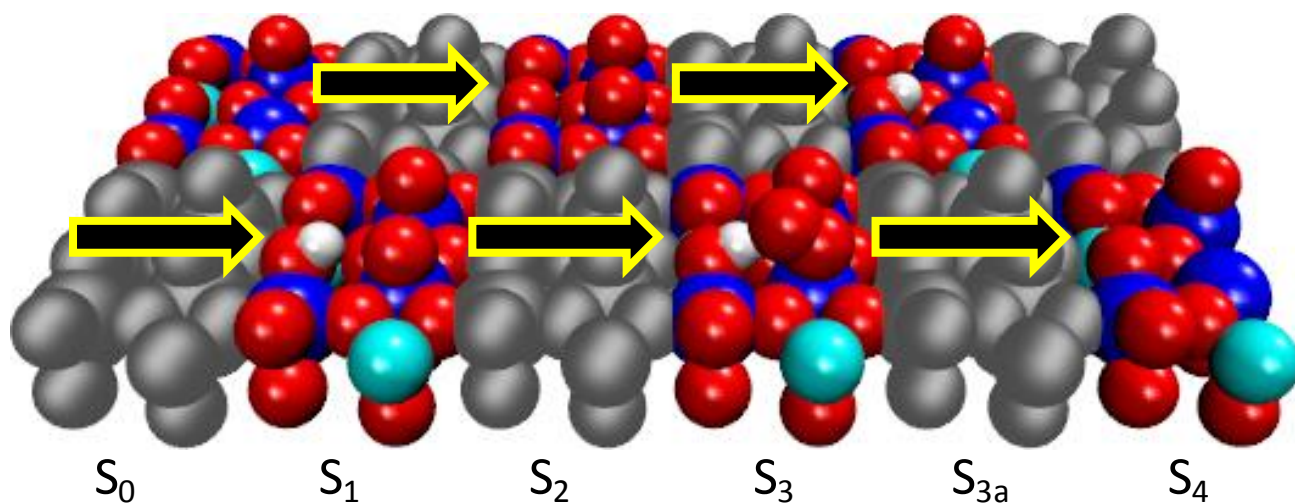

S_0 S_1 S_2 S_3 S_{3a} S_4

Figure 4.3: A visualisation of the 110 surface of modified RuO$_2$ and the OER reaction mechanism on this system. Each state S_0, S_1, S_2 and (S_3 and S_{3a}) and S_4 represents a coupled proton and electron transfer in the OER mechanism. S_0 is the initial binding. S_1 is the binding of *-OH however it splits into *=O and x-H due to the activated bridging O. S_2 is displays the *=O. S_3 corresponds to the *-OOH which splits into *-O$_2$ and x-H. S_{3a} is S_3 with desorped O$_2$ which is considered as the DFT energy of O$_2$ is associated with large deviation from experimental values. S_4 is the same as S_0 completing the catalytic cycle.

A free energy diagram displaying the binding energies of the four intermediate steps for the oxygen evolution for conventional RuO$_2$, Ni and Co modified RuO$_2$ is shown in Figure 4.4. This diagram clearly shows the cause of the reduction of the overpotential and the violation of the scaling relations between *-OH and *-OOH as the *-OOH intermediate on conventional RuO$_2$ is stabilised by around 0.8 eV due to the H-transfer on the Ni and Co modified RuO$_2$ but the *-OH intermediate is almost unchanged.
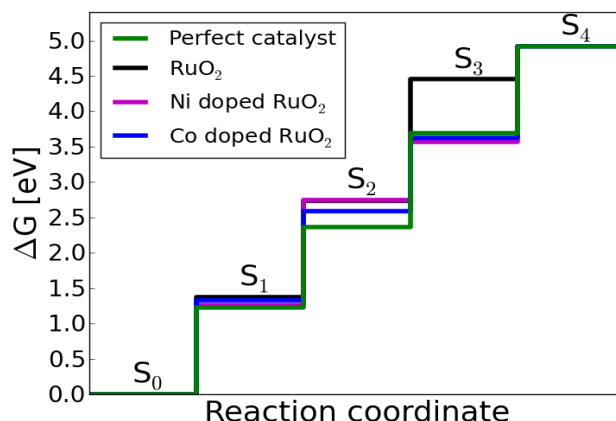
Figure 4.4: Free energy diagram for the perfect catalyst - green, RuO_2 - black, Ni doped RuO_2 - magenta, and Co doped RuO_2 - blue. It should be noted that for the S_2 state of RuO_2 and Ni doped RuO_2 lines overlap and all the lines collapse at the S_0 and S_4 state.

There are several implications of these results which could have large impact on future design and synthesis of OER catalysts. Rutile RuO_2 is a metallic conductor which can also be extracted from the information and therefore the binding energies should not change by the Ni or Co insertion on the surface since it is not possible to dope a metal. The only reason for the change in binding energies is due to the change in mechanism. In Table 4-1 it can be seen that the binding of *=O is largely unchanged by the surface Ni and Co. This is not true for semiconductors as observed with transition metal doped TiO_2 [118] and Ni doped hematite [87] where the binding of the O intermediate can change due to the doping of ions which have a different number of valence electrons. Subsurface doping of Ni in RuO_2 was also performed to further support this claim and compared to two other rutile oxides IrO_2 and MnO_2 in Figure 4.5
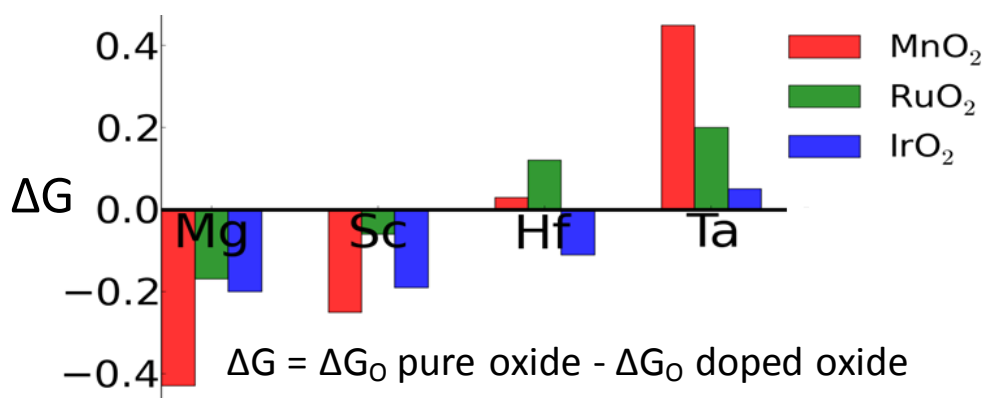
Figure 4.5: Effect on the free binding energy of O on 110 surface of rutile oxides with metallic conductivity RuO_2 and IrO_2 and a semiconductor MnO_2.

The influence of doping in RuO_2 and IrO_2 with either a +2 ion (Mg^{2+}), a 3+ ion (Sc^{3+}), or a 5+ ion (Ta^{5+}) is much smaller when compared to a semiconductor such as MnO_2. A 4+ ion such as Hf^{4+} has almost no change on the binding energies for all considered oxides. When replacing a Mn^{4+} with a lower valent ion either 1 (in the case Sc^{3+}) or 2 electrons are removed (in the case of Mg^{2+}) the oxide surface is slightly deactivated resulting in a higher binding energy when compared to the pure oxide surface and a negative ΔG in Figure 4.5. When adding an electron to an oxide the reverse is the case. The oxide surface is activated giving a stronger binding compared to MnO_2. This is within the standard error associated with DFT calculated binding energies which is around 0.1eV. When this is taken into account it can be seen that RuO_2 and IrO_2 is almost not affected by doping of any of the elements considered except Ta^{5+}. For MnO_2 only doping with Hf results in an unchanged binding energy which is not surprising as Mn and Hf have the same number of valence electrons. However, subsurface doping with ions should not influence the constant scaling between *-OH and *-OOH as the bonding of these two intermediates is of the same character and the catalyst considered still have a single active site. This is also what is observed for doping of TiO_2 [118].

The volcano plot based on the linear scaling relations with the two violations of the scaling relations, Ni and modified is shown in Figure 4.6 using the binding energies from Table 4-1.
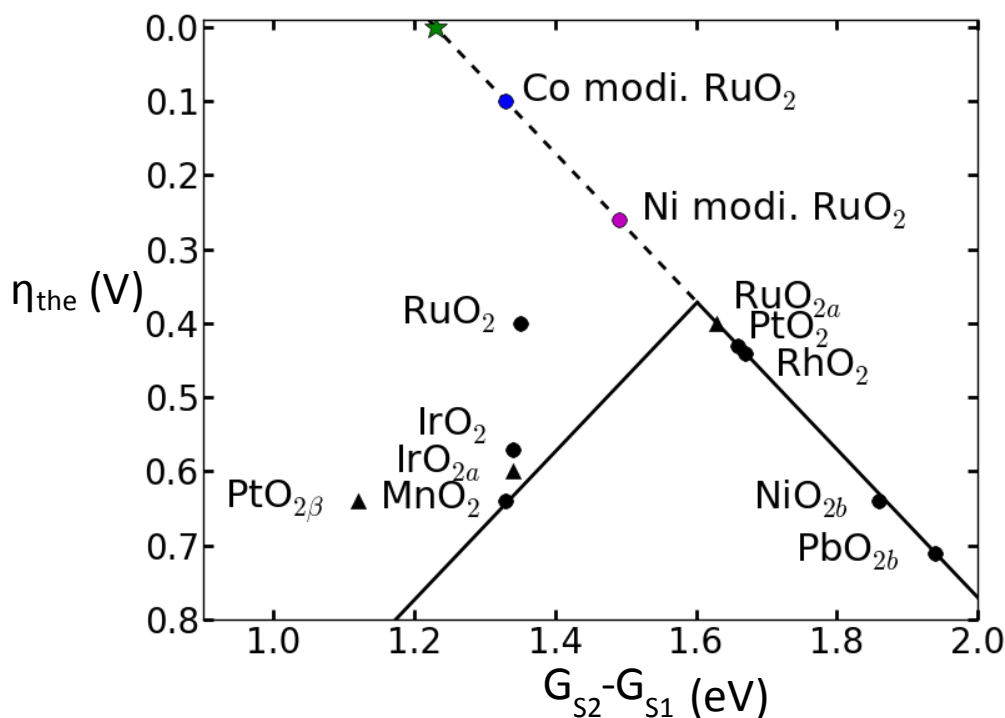
Figure 4.6: The volcano plot for the oxygen evolution with data for selected oxides (rutile, anatase (denoted by an a) and PtO$_{2\beta}$) obtained from literature[37] using the descriptor G$_{S2}$ − G$_{S1}$. Ni and Co modified RuO$_2$ are well above the apex of the volcano. The green star represents the thermodynamic perfect catalyst.

Ni and Co modified RuO$_2$ are positioned well above the apex of the volcano. The theoretical overpotential of Co modified RuO$_2$ is calculated to only 0.1 V. Ni modified RuO2 has a slightly higher overpotential of around 0.3V. This is in contrast to experiments which show that Ni modified RuO$_2$ is more active than Co modified RuO$_2$.

Ni and Co modified RuO$_2$ does not obey the linear scaling relations between *-OH and *-OOH. If they did the binding energies would place the catalysts around the same level as conventional RuO$_2$ as it is the linear scaling relations between *-OH and *-OOH that position *-OOH at a too high energy compared to an ideal catalysts which limits the overpotential. Ni and Co modified is not limited by the linear scaling relations and that is the reason for the increased activity beyond what is predicted by the previous analysis[37].

Experiments also show an increase in activity of Ni and Co modified RuO$_2$ compared to conventional RuO$_2$ with Ni modified RuO2 having a larger impact on the activity (current density) than Co modified RuO2 as seen in Figure 4.7 However, DFT predicts Co modified RuO$_2$ to have the better activity than Ni modified RuO$_2$ due to a lower theoretical overpotential.
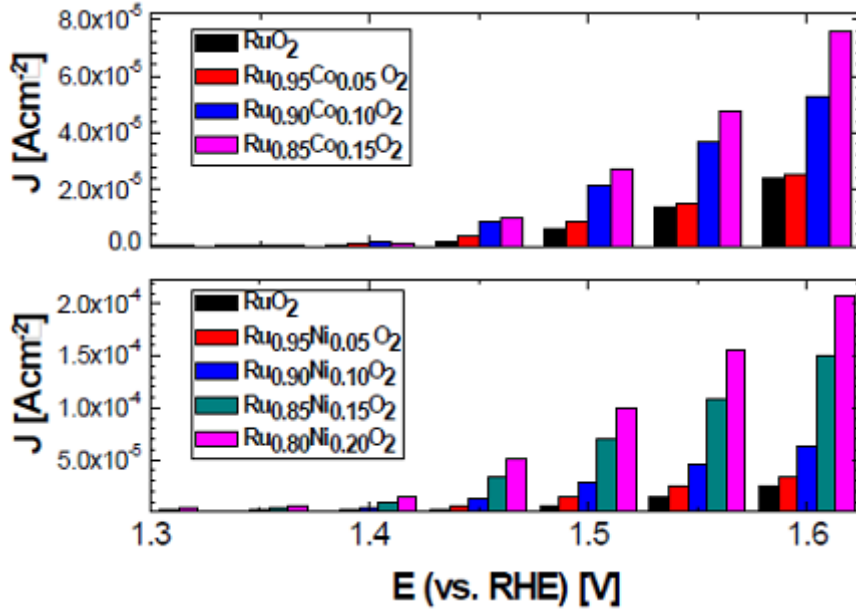
Figure 4.7: Experimental measurement of the total current at different potential in 0.1 M HClO$_4$. Notice the difference in scale showing that Ni modified RuO$_2$ has a higher current density than Co modified RuO$_2$.

The difference between experimental and theoretical results demonstrates another key point when dealing with catalytic activity on catalysts which have a special locally improved active site on the surface. While the RuO$_2$ 110 surface is catalytically active towards OER the special active sites are even more active. In this case the special active site is a local structure which consists of a cus Ru site with a bridging O which is activated by the Ni or Co modification in the immediate vicinity.

However the analysis done with the DFT calculations are a per site analysis and the overpotential is per special active site whereas the experiments measure the total current density of the catalysts which include special active sites and other cus Ru sites. So in order to compare theoretical and experimental results directly the experimental measurements of the current density has to be normalised to a per site activity.

In this particular case, the lone cus Ru sites also contribute to the activity. The current density per special active site can obtained using two current density measurements, one for the modified RuO$_2$ denoted J(RuMe$_x$), and one for a pure RuO$_2$ denoted J(Ru) measurement. By subtracting these two currents and adjusting for the concentration of Ni or Co denoted x the current per site is given by:

$$J(RuMe_{site}) = \frac{J(RuMe_x) - (1-x)J(Ru)}{xy}$$

4.13

The correction parameter y accounts for different cluster orientations with respect to the 110 surface for Ni and Co modified RuO_2. For the Co modified RuO_2, the correction factor is 1/3 for all concentrations. For Ni modified RuO_2 the correction factor varies with the concentration of Ni which equals 1/3 for the low stoichiometry of 0.05 and 3/5 for the higher stoichiometry of 0.1 based on EXAFS studies. The need for the correction factor can be seen in Figure 4.8 where the current per site with and without the correction factor. Co modified RuO2 (red and green symbols) are indeed independent of the concentration X whereas the Ni modified RuO_2 is not before the cluster shape correction factor. This analysis agrees with the DFT results and shows the superior activity of Co modified RuO_2 per site however the total current density is greater for the Ni modified RuO_2 due to the creation of more active sites.
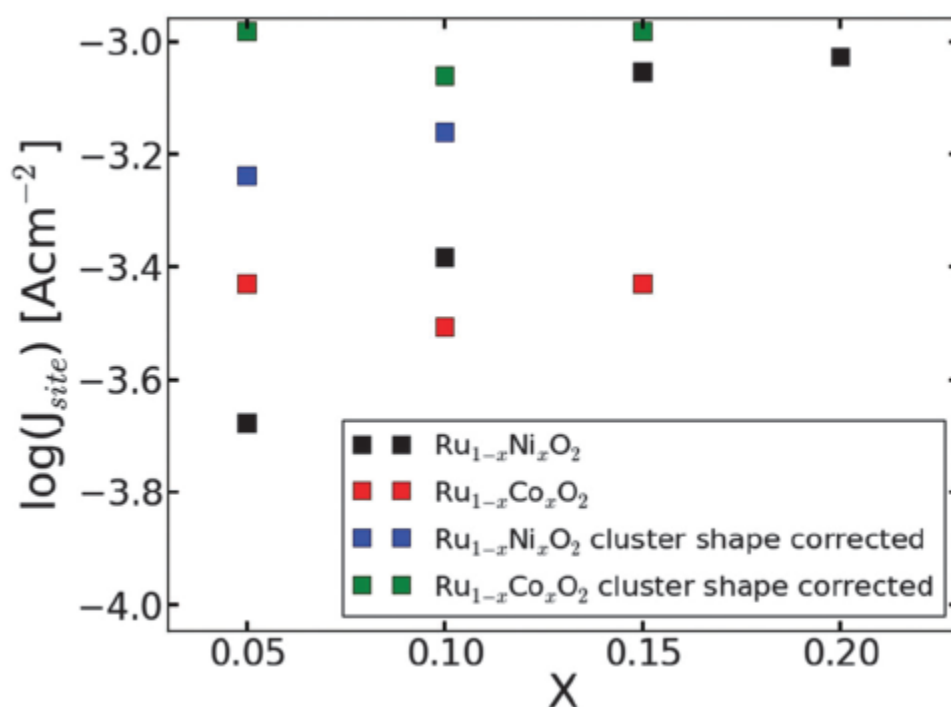
Figure 4.8: Comparison between the site normalised oxygen evolution activity of Ni and Co modified RuO₂ as a function of the Ni and Co content, X, without site cluster shape correction (blue and green squares) and with cluster shape correction (red and black squares.

Ni and Co modified RuO_2 demonstrates that the scaling relations between intermediates can be bypassed by introducing a special active site. In this particular case a hydrogen acceptor functionality is added to surface in the form of an activated bridging O next to either Ni or Co. The theoretical overpotential of the Ni and Co modified RuO_2 is lower than what previously thought possible. These catalysts are not suitable for large scale industrial applications due to scarcity of Ru and the instability of RuO_2 at OER potentials. The modification with

Ni and Co oxide only makes the catalyst more unstable in acidic solution. However, the concept might be transferable to more suitable OER catalysts.

4.2 The beneficial interaction of Au with Mn and Co oxides

The beneficial interaction between Au and transition metal oxides such as CoO_x and MnO_x which enhances the activity towards the oxygen evolution reaction has been observed experimentally [119]–[121]. The increase in activity can be seen in the Tafel plot displayed in Figure 4.9 with the pure oxides in dashed lines and oxides with Au in full lines.
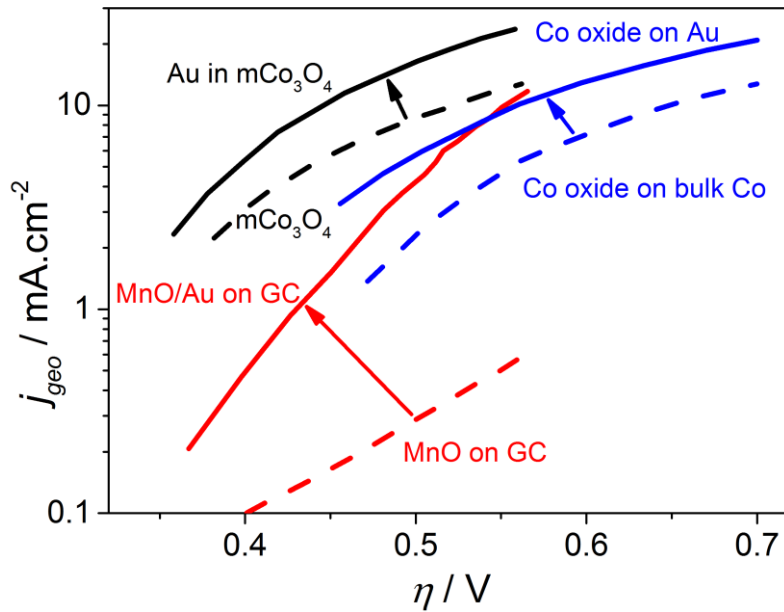
Figure 4.9: Experimental data summarised in a Tafel plot, showing recent reports of OER activity enhancements due to the presence of Au. For MnO$_x$/Au and MnO$_x$ the data is taken from [120]. **For CoO$_x$ on Au and on bulk Co the data is from** [122]**, and for Au in mesoporous (m-) Co$_3$O$_4$ and Co$_3$O$_4$ the data is from** [121].

The concept of the H transfer mechanism can be used to explain why Au improves the activity of MnO_x and CoO_x towards oxygen evolution. In fact the H transfer mechanism could improve any catalysts which is limited by the formation of the *-OOH intermediate. In this particular case when providing an explanation for the beneficial interaction between MnO_x and CoO_x with Au an oxidised Au atom on the Au nanoparticle act is the hydrogen acceptor. As with the modified RuO_2 system the key concept is that the *-OOH intermediate does not form on the surface as it is split in *-O_2 and x-H.

$$*=O + x\text{-}O_{acceptor} \rightarrow *\text{-}O_2 + x\text{-}OH_{acceptor}$$ 4.14
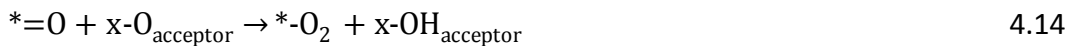
Here the * denotes an active site for O containing species on the either MnO_x and CoO_x and x is the oxidised Au atom on an Au nanoparticle.

Two stoichiometries of Mn and Co oxides were considered. For MnO_x the chosen stoichiometries were MnO_2 and Mn_2O_3. For CoO_x, Co_3O_4 and β-CoOOH with different surface orientations were selected.

Rutile MnO_2 was modelled using a 2x1 supercell. The thickness of the slab was two atomic trilayers and the bulk side was terminated with *-OH species to model the bulk oxidation state of +4. The Mn_2O_3 used a slightly modified unit cell which only contains two subunits of Mn_2O_3. This structure have been used with success in literature [123]. A two monolayer slab was created and terminated in such a way that all Mn ions were in the +3 oxidation state. No termination with *-OH was required as were done with the rutile MnO_2.

For Co_3O_4 and CoOOH the binding energies of the intermediates was obtained only from literature [88].

The effect of Au was investigated using two different approaches. The first approach was to substitute a bridging Mn on rutile MnO_2 110 surface with Au in a bigger 3x1 supercell which actives a bridging O for H transfers much like the modified RuO_2 structures. The other approach was to assume that a specific site on the Au nanoparticle has an oxidised Au atom which has a hydrogen transfer energy (reduction potential) of 1.4eV. The choice is based on a calculation done on the 111 surface of Au with a coverage of 1/3 [124]. This may be a crude approximation as nanoparticles will have many different binding energies depending on the facet and coordination number of the Au atoms on the nanoparticle. However, the single hydrogen transfer energy of 1.4 eV can be used to illustrate the decrease in overpotential towards the OER of MnO_x and CoO_x due to introduction of the Au nanoparticle hydrogen acceptor. An illustration of the splitting of *-OOH due to the Au H acceptor functionality for direct insertion into MnO_2 or by a nearby Au nanoparticle is displayed in Figure 4.10.
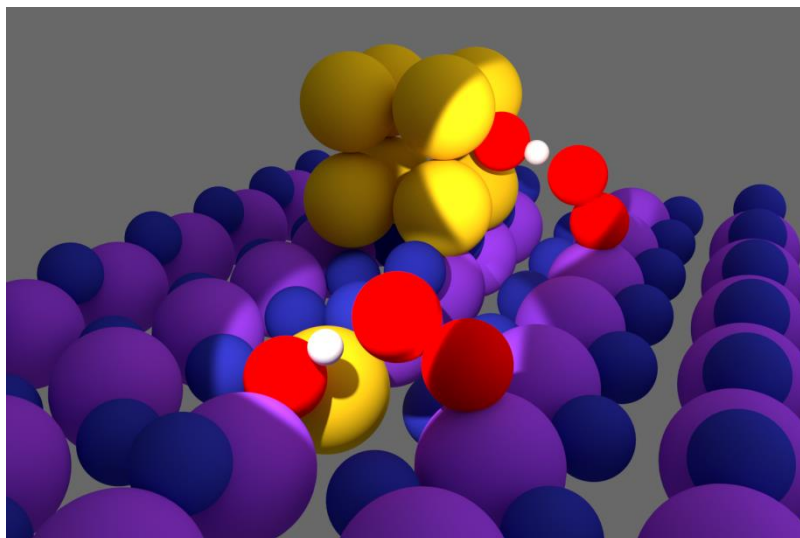
Figure 4.10: Some of the possible incorporations of the H acceptor functionality from Au either in the form of insertion into the bridging row of MnO₂ (in the front) or by a nearby Au nanoparticle (in the back). Color code: Mn - purple, blue - non active O, red - highlighted O, Yellow - Au.

The binding energies of the *-OH, *=O and *-OOH or *–O₂ and -OH_acceptor for the OER on Mn_2O_3, MnO_2, $CoOOH$ and Co_3O_4 with and without the effect of Au at zero applied potential are shown in a free energy diagram in Figure 4.11.
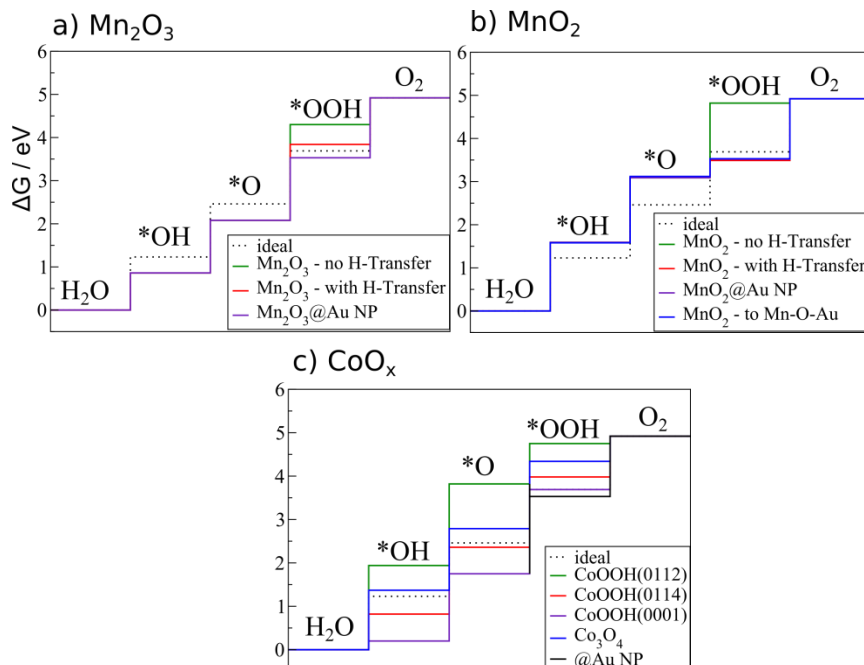
Figure 4.11: Free energy diagrams for the OER on MnO₂, Mn₂O₃ and CoOₓ with no applied potential. The dotted line on all subfigures displays the perfect catalyst. a) Modified Mn₂O₃ with color code: Green – no H transfer, red – with H transfer, and purple - H transfer at a Au nanoparticle. b) rutile MnO₂ with same color code as supfigure a including blue – H transfer to a bridging O next to Au. c) CoOₓ with 3 orientations including Co₃O₄ and the H-transfer to an Au

**nanoparticle for all considered surfaces. Color code: Green – (0112), red (0114), purple – (0001), red – Co_3O_4, and black – H-transfer to an Au nanoparticle.**

The one site mechanism for the oxides always result in a higher binding of the *-OOH intermediate for MnO_2 and Mn_2O_3 and the different orientations of CoOOH as seen on the green curve on figure 4.11a, 4.11b and green, red, purple curve in figure 4.11c.

The H transfer denoted by the red lines in figure 4.11a and b refers to an H-transfer to an adjacent Mn=O site. This is a clear stabilisation compared to the *-OOH intermediate for both MnO_2 and Mn_2O_3 compared to the mononuclear mechanism. However the adjacent sites themselves are involved active sites for the OER so they are probably not available for H transfers. It should also be mentioned that the correlation between the theoretical overpotential and the actual measured overpotential support the one site mechanism[37] and the fact that MnO_2 is less active OER catalyst than RuO_2 which is not the case assuming the H transfer to an adjacent Mn=O site.

The H transfer mechanism in all the considered oxides lowers the energy of the stoichiometric adsorption of the state corresponding to the *-OOH adsorption. For catalysts that binds *-OOH too weakly this will reduce the overall overpotential for the oxygen evolution reaction. The addition of the Au nanoparticle which acts as a hydrogen acceptor should ideally change the potential limiting step from third reaction energy which is the second water adsorption (*=O to *-OOH see eq. 4.3) to the deprotonation of –OH which is the second reaction energy. (*-OH to *=O see eq. 4.4).

A volcano sketch displaying the influence of adding the hydrogen transfer energy of 1.4eV is shown in Figure 4.12. The green curve depicts the volcano curve for the mononuclear mechanism and the green data points are the theoretical overpotential towards OER for the various oxides assuming the mononuclear mechanism. The black curve depicts the volcano curve of the binuclear mechanism using an Au=O site as an H-acceptor for the third reaction step. The black points show the theoretical overpotential obtained with this H-acceptor for the various oxides considered.
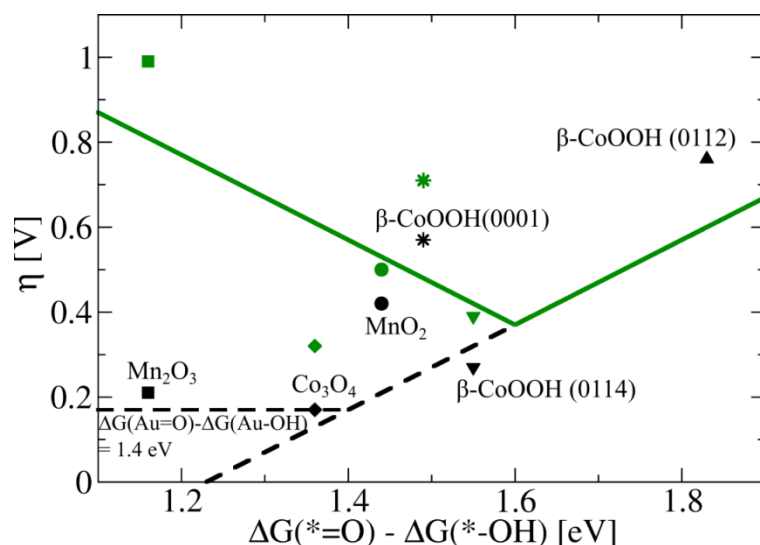
Figure 4.12: In green the theoretical volcano for the OER using a mononuclear mechanism. The green data points show the theoretical overpotential for oxides using this mechanism. This mechanism is limited by the scaling between *-OH and *-OOH. The effect of the H acceptor functionality of Au is shown in black for theoretical volcano. The overpotential is now limited by the reduction potential of the oxidised Au on the Au nanoparticle which set to 1.4V. The black data points show the theoretical overpotential of the oxides using the Au nanoparticle site as an H acceptor.

As seen in Figure 4.12 using the Au nanoparticle as a H acceptor during the OER mechanism the minimum achievable theoretical overpotential has effectively been halved. The scaling between *-OH and *-OOH have been eliminated since *-OOH does not form on the surface and the lowest achievable theoretical overpotential is now limited by the reduction potential of the oxidised Au on the Au nanoparticle since the reduction potential is not ideal (1.4V vs. 1.23V which would be ideal).

The black data points roughly correspond to limits set by the theoretical volcano. However, it is interesting that MnO_2 and β-CoOOH (0001) is not improved much by the H-transfer mechanism. This is due to the fact that it is neither the second reaction energy (*-OH to *=O) or the third reaction energy (*=O to *-OOH) is potential limiting. For the β-CoOOH (0001) final release of the hydrogen from the acceptor site is potential limiting and for MnO_2 the initial binding of *-OH becomes potential limiting. This may have been avoided with a more complicated descriptor but it was chosen to be consistent with previous work on modified RuO_2 (see section 4.1).

Without any H-transfer mechanism MnO_2 and β-CoOOH (0114) are close to the limit of 0.4V set by the limits of constant offset between *-OH and *-OOH [37]. The introduction of Au as a H acceptor shift the optimal reaction energy of the

formation of the *=O intermediate from 1.6 eV which is the apex of the volcano assuming a mononuclear mechanism to reaction energies of the region of 1.2-1.4 eV which is the range that Mn_2O_3 and Co_3O_4 have reaction energies. As a consequence the introduction of Au has the largest change in theoretical overpotential for Mn_2O_3 and Co_3O_4.

While MnO_2 is the most stable phase at potentials relevant for oxygen evolution there is evidence that a Mn has a lower oxidation state in the vicinity of Au according to ex-situ XAS[120]. This suggests that near the vicinity of an Au nanoparticle Mn could exist in a Mn_2O_3 like structure and be responsible the OER activity. Without the gold the Mn_2O_3 is quite inert towards oxygen evolution with an overpotential of 1V, however, with the introduction of Au reduces the overpotential to only 0.2 V.

The binding energies either obtained from literature [88], [123], [124] or calculated for this work are listed in Table 4-2. The energies listed are free energies meaning that zero-point energies and entropy corrections obtained from literature[37] have been added to obtain the free energies.

Table 4-2: Binding energies for MnO_x, CoO_x oxides and Au(111) calculated using DFT with no applied potentials and at standard conditions with reference to H_2O and H_2. The data marked by * have been obtained from literature [88], [123], [124].

| System	ΔG_{OH} [eV]	ΔG_O [eV]	ΔG_{OOH} [eV]	η_{the} [V]	η_{the} [V] with Au(111)
*Co_3O_4	1.43	2.79	4.40	0.38	0.2
*β-CoOOH(0112)	1.94	3.82	4.75	0.76	0.76
*β -CoOOH(0114)	0.82	2.36	3.98	0.48	0.33
*β -CoOOH(0001)	0.20	1.75	3.69	0.70	0.54
MnO_2	1.59	3.09	4.82h	0.56	0.36
Mn_2O_3	0.86	2.08	4.30	1.05	0.21
*Au(111); $q_{*=O}$ = 1/3	1.15	2.85	4.39	-	

It can be difficult to compare the effect when comparing theoretical predicted activity towards OER and the actual measured OER activity. At the interface of the Au and MnO_x or CoO_x a special active site is created which is highly active towards OER. However, there will be a dampening effect since not all the sites will be activated by Au and without a detailed count or estimation of these special active sites it is not possible to estimate the exact increase in OER activity and how much is due to the special active sites. However the increase in activity is observed experimentally as shown in Figure 4.9 can at least conceptually be understood using the concept of special active sites and the following analysis.

5 Oxygen reduction on RuO_2 and modified RuO_2

This section here summarise the effort made in paper 3 regarding oxygen reduction on RuO_2 and modified RuO_2 with Co, Ni and Zn as well as the influence on the local structure and the selectivity between the two reduction products of the ORR, H_2O and H_2O_2.

H_2O_2 is another possible product from oxygen reduction besides H_2O. The reaction mechanism for both reactions is shown below. The selectivity between the 2-electron pathway to H_2O_2 and the 4-electron pathway to H_2O is where the second proton adsorbs. To form H2O2 the *-OOH the proton needs to attack the O closest to the surface:

$$O_{2(g)} + H^+ + e^- \,* \rightarrow *\text{-OOH} \qquad\qquad 5.1$$

$$*\text{-OOH} + H^+ + e^- \rightarrow * + H_2O_2 \qquad\qquad 5.2$$
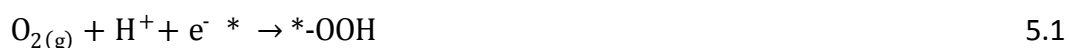
If the O furthest away from the surface is protonated a release water will follow leaving *=O intermediate on the surface and continue along the 4-electron pathway forming two water molecules is shown below:

$$*\text{-OOH} + H^+ + e^- \rightarrow *\text{=}O + H_2O \qquad\qquad 5.3$$

$$*\text{=}O + H^+ + e^- \rightarrow *\text{-OH} \qquad\qquad 5.4$$

$$*\text{-OH} + H^+ + e^- \rightarrow * + H_2O \qquad\qquad 5.5$$

Selectivity between the reaction 5.2 and 5.3 is key to understanding the oxygen reduction on RuO_2 and modified RuO_2 which is not typically captured using only thermodynamic reaction energies as the reaction barrier will determine selectivity. However, a thermodynamic approach to the problem have proved a valuable tool for understanding H_2O_2 production on metal alloys[71].

The bulk and surface structure of nanocrystalline RuO_2 and modified RuO_2 with Ni, Co and Zn were observed to be rutile using X-ray diffraction patterns. All patterns of the modified RuO_2 resemble the rutile RuO_2 and SEM images verify an enrichment of the inserted metal on RuO_2 surface especially for Zn.

The activity of the RuO_2 was assessed using a rotating disk electrode setup in alkaline solution. The rotating disk electrode setup can used to distinguish between current contribution from the overall oxygen reduction and the contribution from H_2O_2 production as seen on Figure 5.1. It is observed RuO_2 and Zn modified RuO_2 show a larger overall ORR activity as seen on the higher disk current compared to the Ni and Co modified RuO_2 samples as seen in the bottom plot in figure 5.1. However, Ni and Co modified RuO_2 have a higher ring disk current as seen in top of Figure 5.1 meaning that Ni and Co modified RuO_2 favours the 2-electron pathway more than RuO_2 and Zn modified RuO_2.
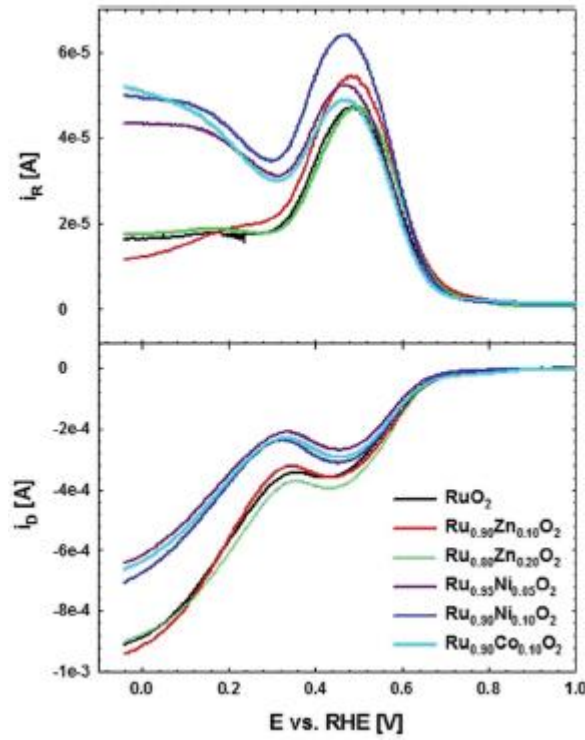
Figure 5.1: Polarisation curves for oxygen reduction on RuO_2 and modified RuO_2. The top displays the current contribution from the ring current (i_R) and the bottom the current contribution from the disk (i_D).
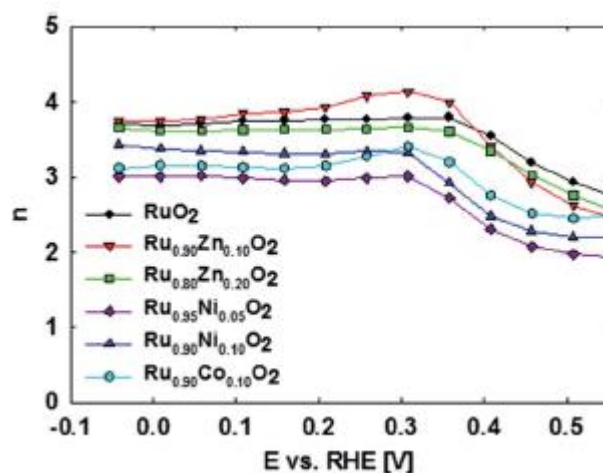
Figure 5.2 displays the potential dependence of the average number of electrons transferred during the oxygen reduction for conventional RuO_2 and modified RuO_2. This estimated using the Koutecky-Levich equation[125] :

$$\frac{1}{i} = \frac{1}{i_K} - \frac{1}{0.62nAFD_{O_2}{}^{2/3}v^{-1/6}C_{O_2}^*\omega^{1/2}} \qquad 5.6$$

The currents consist of two terms; one containing i_K which is the current without mass-transfer effects and the second term is the diffusion limited current. In the diffusion limited current n is the number of electrons, A is the geometric area of

the electrode, D is the diffusion constant, F is the Faraday constant, v is the kinematic viscosity and C is the bulk concentration of the analyte (O_2) in the electrolyte and ω is the angular rotation rate of the rotating ring disk electrode. The Koutecky-Levich equation can then be used to correlate the potential to the average number of electrons transferred during ORR using the polarisation curves.


Figure 5.2: Potential dependence of the average number of electrons transferred during oxygen reduction on RuO_2 and Zn, Co and Ni modified RuO_2. Data is calculated using the Koutecky-Levich equation.

At relatively low overpotentials Ni and Co modified RuO_2 has a more pronounced tendency to follow the 2-electron pathway and at high overpotentials the average number of electrons seems to converge to around 3 as seen in Figure 5.2. For RuO_2 and Zn modified RuO_2 at relatively low overpotentials both the 2-electron and the 4-electron pathway is possible and the as the potential increases the 2-electron pathway is blocked.

Based on these results, RuO_2 and Ni modified RuO_2 nanoparticles was modelled using the 110 surfaces for both conventional and modified RuO_2 are the same as described in section 4.1 with two Ni atoms on the surface of 1x3 supercell with a slab thickness of 4 atomic trilayers and smaller slab for conventional RuO_2. The theoretical analysis is based on binding energies calculated using DFT with GPAW. The active site for the ORR mechanism is still a Ru cus site on the surface. The hydrogen transfer mechanism is not valid for the potentials at which ORR occurs on RuO_2 which means that only the mononuclear mechanism is considered.

To assist the experimental finding the binding energies are computed for three different potentials; 0V, 0.5V and 0.8V versus the computational standard

52

hydrogen electrode and illustrated on Figure 5.3. Three active sites are considered, the cus site on conventional RuO_2, the Ru cus site on Ni modified RuO_2 and the Ni cus site on the Ni modified RuO_2. These active sites are chosen to investigate the observed difference between Ni modified RuO_2 and conventional RuO_2. To simulate the binding energies on Ni cus site of RuO_2 all Ru cus sites needs to blocked otherwise the intermediates on the Ni cus will migrate to the Ru cus sites during structure optimisation. So the Ru cus sites are covered with *-OH.
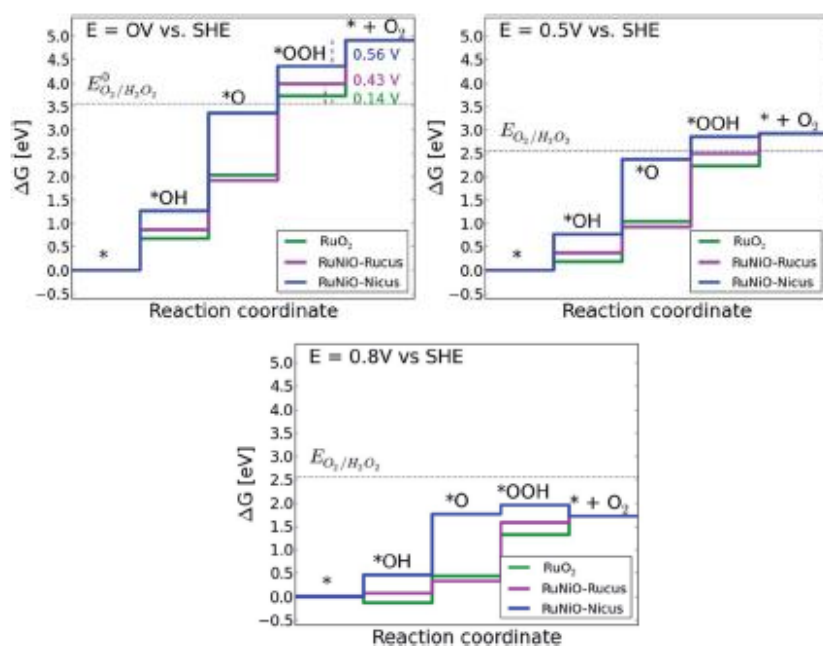
Figure 5.3: Free energy diagram at three different potentials for the oxygen reduction reaction on three active sites. Ru cus site on conventional RuO_2, the Ru cus site on the Ni modified RuO_2 and the Ni cus site on the Ni modified RuO_2.

The free energy diagrams in Figure 5.3 shows that there is basically no difference between the binding energies of *-OOH, *=O and *-OH on the Ru cus site whether it is on RuO_2 or Ni modified RuO_2. This is not surprising as it was observed for the OER described in section 4.1 as well. For Ni cus site on modified RuO_2 all energies are shifted up especially for the *=O intermediate which almost approaches the equilibrium potential between O_2 and H_2O_2. The potential difference between *-OOH and H_2O_2 can be used as a descriptor for the preference between forming H_2O_2 and H_2O. For a catalyst to be an efficient catalysts toward the formation of H_2O_2 the binding of *-OOH should be between the O_2 and the H_2O_2 and ideally the *=O intermediate should be above the energy of H_2O_2. The Ni cus site on Ni modified RuO_2 almost satisfies both conditions both require high overpotentials to be activates.

This analysis of the three active sites on RuO_2 and Ni modified RuO_2 agrees with the experimental observations in Figure 5.2 that at high overpotential the Ni modified RuO_2 nanoparticles approaches an average number of electron of 3 meaning there is equal tendency to form H_2O or H_2O_2. Co modified RuO_2 behaves like Ni modified RuO_2. For RuO_2 the average number of electrons approaches four meaning that they produce H_2O. Zn and RuO_2 behave similarly which is most likely due to Zn not being redox active. A double volcano as Figure 5.4 can be used illustrate the difference in behaviour between the two classes of catalysts based on the binding *-OOH similar to literature[71].
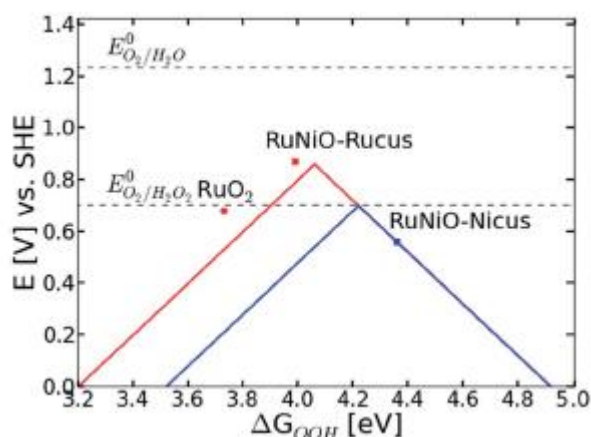
Figure 5.4: Theoretical volcanos for the 4-electron (red) and the 2-electron oxygen reduction reaction to H_2O and H_2O_2 respectively assuming a mononuclear mechanism. The binding energy of *-OOH as a descriptor. It should be noted that the binding $G_{OOH} = G_{OH} + 3.2$ eV due to the linear scaling between these intermediates in the mononuclear mechanism.

Based on the binding of *-OOH to the surface the cus Ru site should favour the 4 electron pathway. The Ni cus site there is no thermodynamic preference for either 2 or 4 electron pathway. This is not entirely what is observed in the experimental work as the thermodynamic analysis based on binding energies obtained from DFT fails to predict the hydrogen peroxide formation at low overpotentials. This apparent formation of H_2O_2 for all RuO_2 surfaces could occur from metastable intermediates due to relatively short timescales of the rotating ring-disk electrode experiments and thus oxides fail to reach the thermodynamic equilibrium which is simulating by the DFT calculations.

This study also validates the model used to simulate the Ni modified RuO_2 for both the OER and the ORR. The OER activity was promoted by either Ni or Co positioned in the bridge site and the H_2O_2 production at high overpotentials is explained by Ni or Co positioned in the cus position both of which was included in the model system.

6 Unifying oxygen electrocatalysis

Unlike a simple catalytic reaction where the catalyst increases the rate of the reaction in both directions by lowering the activation energy of the reaction, this is not the case for oxygen electrocatalysis. As mentioned in the section 3.3 the linear scaling relations between *-OH, *=O and *-OOH prevents the design of a single active site which is active towards both the OER and the ORR. So far this work has only dealt with oxide catalysts for either ORR or OER. Here another catalyst group is chosen to demonstrate the potential benefits of having an organic hydrogen acceptor in the vicinity of a transition metal atom embedded in a 2d graphene sheet. These transition metal doped graphene sheets have been studied for use in the ORR both experimentally[126]–[130] and theoretically using density functional theory on modified graphene sheets [69] or molecular compounds[68].

The special active site concept is explored on pyrrolic (5-membered N containing ring) and pyrridinic (6-membered N containing ring) modified graphene sheets with different transitional metals incorporated. The hydrogen acceptor functionality is explored separately using different organic functional groups that could be added to graphene. The two systems which for future reference will be termed functionalised graphene that will be used to model the OER and ORR are shown on figure 6.1
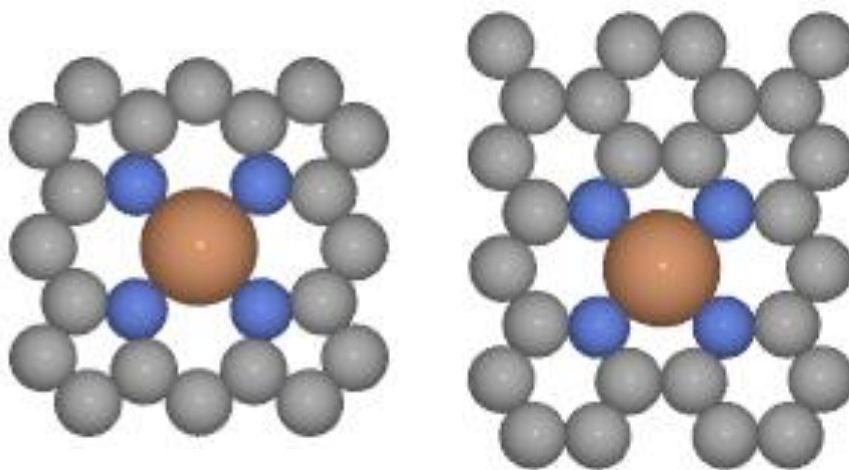
Figure 6.1: Model systems for the pyrrolic (left) and pyrridinic (right) embedding of transition metal ions. The systems are with periodic boundary conditions. Color code: Gray – carbon, blue – nitrogen, orange – transition metal in this case Fe.

The hydrogen transfer mechanism can be enabled in two different ways. Either a nearby identical active site can serve as the hydrogen acceptor or donor or a fully

independent functional group such as an amino, a carboxylic acid, an alcohol group or a pyrridinic or pyrrolic site with no transition metal formed on the graphene support during synthesis could serve the role. Two different sites for the functional group are considered the edge position and an "on top" position as seen in Figure 6.2. The R-COOH in the "on top" position is omitted the C-C distance is so long that it is desorbed.
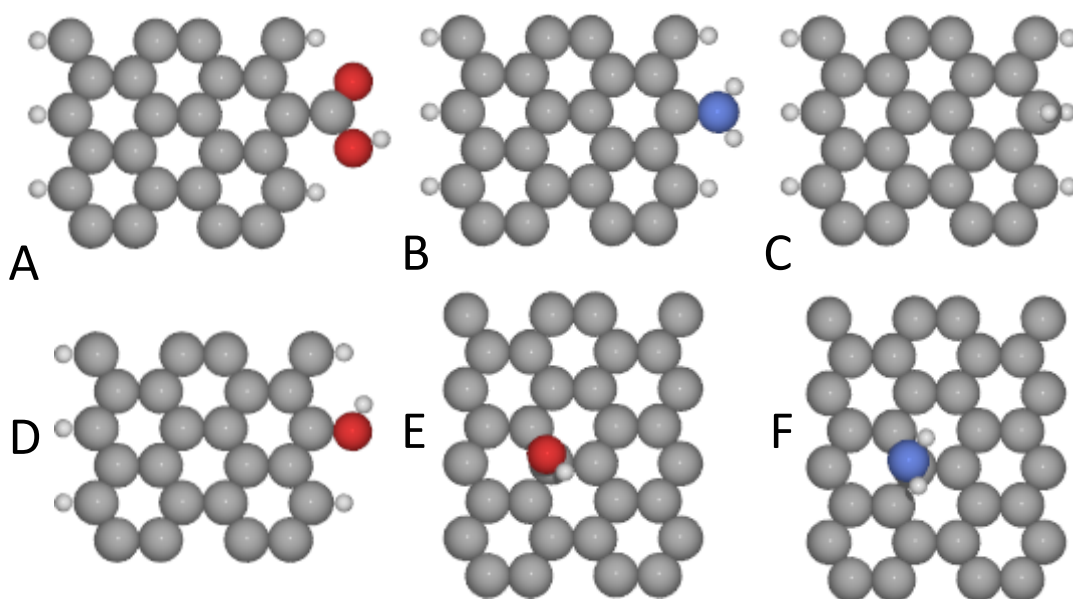
Figure 6.2: Functionalised graphene sheet considered as hydrogen transfer candidates. A) R-COOH on edge B) R-NH$_2$ on edge C) R-H$_2$ on edge D) R-OH on edge E) R-OH on top F) R-NH$_2$ on top.
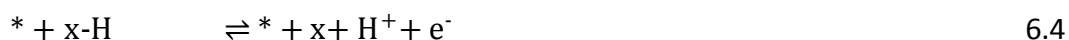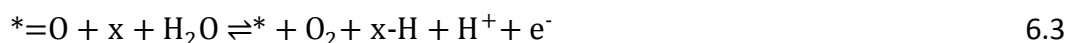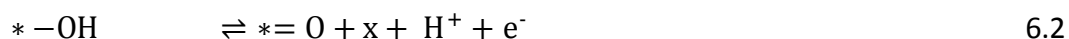
For the functional groups positioned on the edges a small nanoribbon terminated with H is used with sufficient vacuum to avoid interaction with the periodic images. The hydrogen transfer potential or oxidation potential is listed in Table 6-1 for the different functional groups and positions together with oxidation potential for a pyrridinic or pyrrolic site with no transition metal in functionalised graphene.

Table 6-1: Oxidation potential for selected hydrogen transfer candidates with different positions on the graphene sheet.

Free Pyrridinic Graphene		
System	Position	ΔG_{ox} (eV)
Pyridine-H4	Centre	-0.40
Pyridine-H3	Centre	-0.48
Pyridine-H2	Centre	1.91
Pyridine-H		2.16
Free Pyrrolic Graphene		
System	Position	ΔG_{ox} (eV)
Pyrrole-H4	Centre	0.69
Pyrrole-H3	Centre	0.59
Pyrrole-H2	Centre	1.97
Pyrrole-H	Centre	2.59
Other Organic Hydrogen Donors		
System	Position	ΔG_{ox} (eV)
R-OH	On top	1.65
	Edge	-0.60
R-NH$_2$	On top	2.52
	Edge	0.56
R-COOH	Edge	1.05
R-H$_2$	Edge	1.14

GPAW was used for calculating the oxidation potentials and the binding energies using the model systems. The parameters for the calculation were a grid-spacing of 0.15 Å and a Monkhurst-Pack2x2x1 was used for sampling the Brillouin zone. Spin was treated explicitly for all systems and allowed to relax during the convergence of the wave function. The geometries were optimised using the BFGS algorithm. The zero-point energy correction are obtained from literature [117].

As seen with the Ni and Co modified RuO_2 and the Au/MnO_x and Au/CoO^x system the scaling relations between *-OH and *-OOH can be bypassed and using a special active site with two different sites one for O containing species and one for H containing species.. This means that the volcano description of the OER and ORR based on a mononuclear mechanism which has these scaling relations is no longer are sufficient to describe the catalyst activities studied in this part. The reaction mechanism considered includes the possibility of a hydrogen transfer to a hydrogen acceptor group in the vicinity.

$$* + x + H_2O \rightleftharpoons \text{*-OH} + x + H^+ + e^- \qquad\qquad 6.1$$

$$* - OH \rightleftharpoons * = O + x + H^+ + e^- \qquad\qquad 6.2$$

$$\text{*=O} + x + H_2O \rightleftharpoons * + O_2 + \text{x-H} + H^+ + e^- \qquad\qquad 6.3$$

$$* + \text{x-H} \rightleftharpoons * + x + H^+ + e^- \qquad\qquad 6.4$$

The associated binding energies for these reactions are called G_1, G_2, G_3 and G_4 respectively. The only difference from the mononuclear mechanism is the hydrogen transfer during the third reaction step is which means that *-OOH does not form on the surface. The *-OOH intermediate is more flexible and should be more likely to position itself so the H can transfer to an adjacent hydrogen acceptor group . The *-OH could potentially also be available for a H transfer to the an adjacent hydrogen acceptor group but at least for the case of the Ni and Co doped RuO_2 this particular transfer did not make a large difference since the binding energies of *-OH and *=O x-H are very similar and within the normal DFT error of 0.1 eV.

To simplify the theoretical understanding of the influence on the hydrogen acceptor groups on the catalytic activity of the functionalised graphene sheets three approximations are made:

- The first and second reaction energies are identical meaning that $G_O = 2*G_{OH}$
- The hydrogen transfer only occurs as an alternative to the formation of *-OOH
- There is no barrier for the hydrogen transfer

With these three approximations the energy landscape for OER and ORR s shown on Figure 6.3 using the reaction energies of G_2 (eq. 9.2) and G_3 (eq. 9.3) as descriptors. For any given G_2 and G_3 the remaining reaction can be found as G_2 equals G_1 which is the only constraint used. G_4 is determined since the sum of

reaction energies equals 4.92eV. For the OER the largest of the reaction energies gives the potential and for the ORR the smallest of the reaction energies gives the potential. A double pyramid is created with this analysis as seen in Figure 6.3.
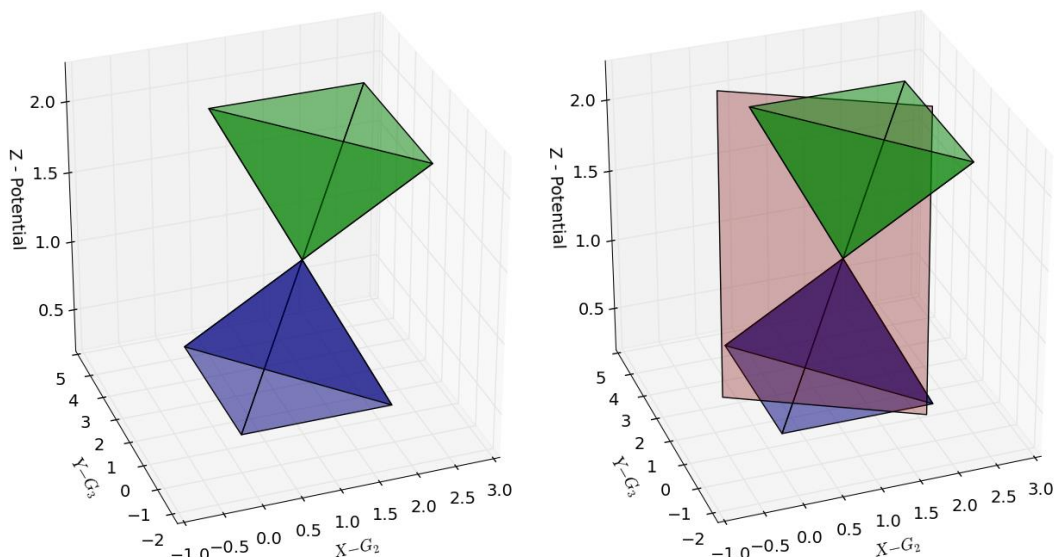
Figure 6.3: The theoretical volcano pyramids for the minimum overpotential for oxygen electrocatalysis using only the constraint that $G_O = 2 * G_{OH}$ as a function of G_2 and G_3. The ORR energy landscape is shown in blue and the OER energy landscape is shown in green. The red plane is with the additional constraint that $G_{OOH} = 3.2 + G_{OH}$.

The two volcanos in Figure 6.3 meet in a single point (1.23,1.23,1.23), demonstrating that an ideal catalyst indeed could be designed if the three approximation stated above are valid. The scaling relations between *-OH and *-OOH effectively limits this energy landscape to a plane where the catalyst with a mononuclear mechanism is positioned. The plane cutting through the two pyramids is seen to the right of Figure 6.3.

The catalysts which have a mononuclear mechanism and therefore constant offset of 3.2 eV between the *-OH and *-OOH are visualised in figure 6.4 with the volcanos for the ORR and OER. The data collected from literature for metals, metal alloys and oxides [37], [43] considered for oxygen electrocatalysis. The data obtained from the transition metal doped graphene sheets in this work is included as well assuming a mononuclear mechanism. It is important to note that while the catalysts are limited by the universal scaling relations the ORR and OER catalysts do not have the same descriptor for the volcanoes since the potential limiting step is typically G_2 or G_3 for oxygen evolution catalysts and G_1 or G_4 for the oxygen reduction catalysts. This is the reason for the scatter in the data obtained from the functionalised graphene calculations which is largest in

lower right section in Figure 6.4 which illustrate the ORR volcano. This is because G_2 is not good descriptor for ORR when dealing with functionalised graphene and in literature G_1 [68], [69] has been used for these systems. The metals follow the volcanic trend almost ideally since they follow the assumption that $G_1 = G_2$ to a satisfactory level.
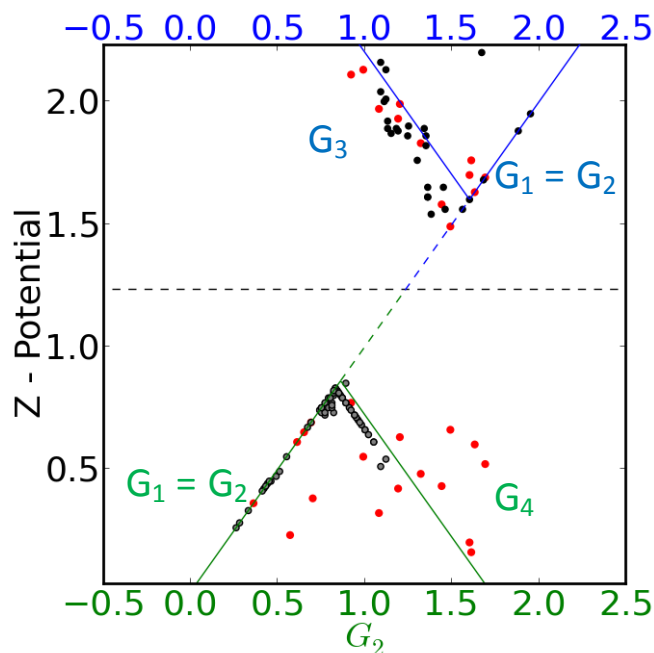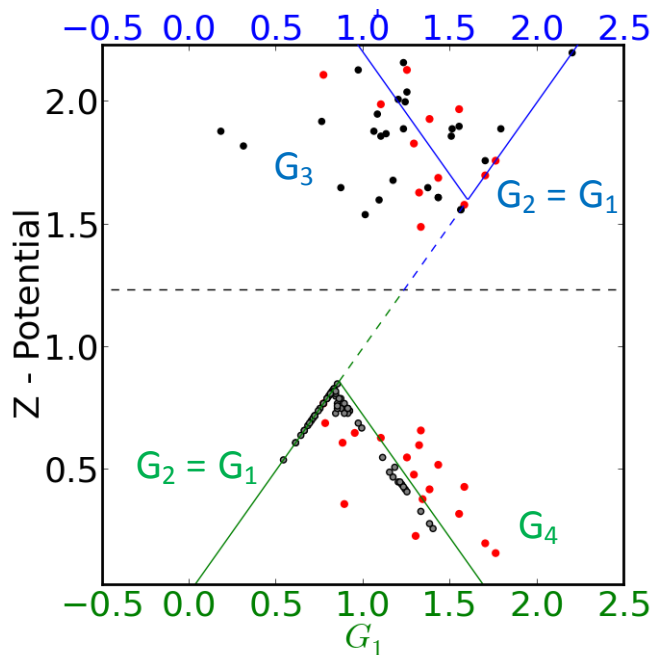

Figure 6.4: 2d cross section represented by the red plane in figure 6.3 with the green ORR volcano in the bottom and the blue OER volcano on the top using G_2 as the descriptor. The potential limiting for each legs of the volcanos are labelled. The horizontal dotted line illustrate no overpotential for oxygen electroctalysis. The other dotted line connects the two volcanos and the ideal catalyst with no overpotential is positioned at the intersect. The data illustrating the trends are obtained from literature. Gray − ORR data of metal and alloys [43]. Black − OER data from oxides [37] Red − functionalised graphene considered for both ORR and OER.

G_1 could have been chosen as a descriptor in Figure 6.4 as well however the oxides considered the assumption that $G_1 = G_2$ is not valid as seen in Figure 6.5. The choice of G_2 as a descriptor is a compromise and is selected since the metals uphold the assumption of $G_1 = G_2$ better than the oxides. For the functionalised graphene either descriptor could have been used with equally accuracy.

Figure 6.5: 2d cross section represented by the red plane in figure 6.3 with the green ORR volcano in the bottom and the blue OER volcano on the top using G_1 as the descriptor. Otherwise, the volcano is a replica of previous figure.

The principle of the double volcano has been illustrated before in literature with similar systems although in molecular form [68] and based on molecular orbital theory [62] for perovskites as illustrated in Figure 6.6. While the e_g electron filling must somehow be connected to the binding energies to the surface the correlation is not straightforward. The analysis of the OER and ORR on porphyrines and perovskites show that based on a single descriptor it is not possible to have a functional active site that has optimal catalytic activity towards both ORR and OER. This is due to the linear scaling relations between intermediates that shift the apex of the volcanoes for the OER and ORR away from the thermodynamic equilibrium potential (1.23eV) of oxygen electrocatalysis.
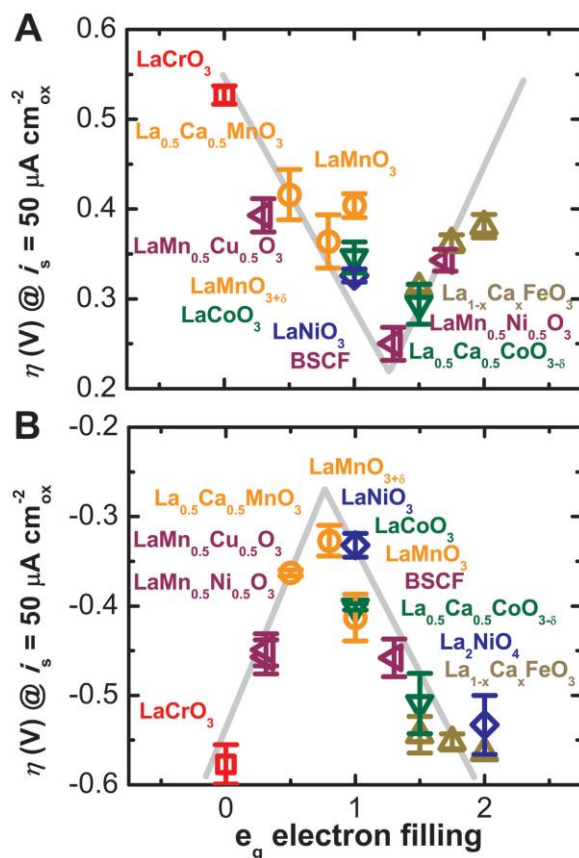
Figure 6.6: Overpotentials at 50µA/cm² as a function of the e_g electron filling on various perovskites investigated. A) as OER catalysts B) as ORR catalysts. Figure originate from [62] and is reprinted with permission from the authors.

The binding energies for the Fe, Co and Mn doped graphene in a pyrrolic (Me-pyrr) and pyrridinic environment (Me-pyri) is listed in table 6-2 assuming the mononuclear mechanism. The influence of an addition ligand coordinated to the transition metal in the form of NH_3 and NH_2 are included as well denoted Me-pyr-NH_3 and Me-pyr-NH_2.

Table 6-2: Binding energies of intermediates G_{OH}, G_O and G_{OOH}, reaction energies of the 4 steps in the reaction mechanismm G_1,G_2,G_3 and G_4 assuming a mononuclear mechanism for the test set of functionalised graphene.

System	G_{OH} [eV]	G_O [eV]	G_{OOH} [eV]	G_1	G_2	G_3	G_4
Fe-pyrr	1,34	2,04	4,54	1,34	0,7	2,5	0,38
Co-pyrr	1,58	3,02	4,49	1,58	1,44	1,47	0,43
Mn-pyrr	1,3	1,87	4,69	1,3	0,57	2,82	0,23
Fe-pyri	0,88	1,49	3,83	0,88	0,61	2,34	1,09
Co-pyri	1,33	2,82	4,26	1,33	1,49	1,44	0,66
Mn-pyri	0,89	1,25	3,9	0,89	0,36	2,65	1,02
Fe-pyrr-NH_2	0,77	1,69	3,8	0,77	0,92	2,11	1,12
Co-pyrr-NH_2	1,43	3,12	4,4	1,43	1,69	1,28	0,52
Mn-pyrr-NH_2	1,25	2,24	4,37	1,25	0,99	2,13	0,55
Fe-pyri-NH_2	0,78	1,47	3,78	0,78	0,69	2,31	1,14

System	G_{OH} [eV]	G_O [eV]	G_{OOH} [eV]	G_1	G_2	G_3	G_4
Co-pyri-NH$_2$	1,32	2,95	4,32	1,32	1,63	1,37	0,6
Mn-pyri-NH$_2$	0,95	1,6	3,99	0,95	0,65	2,39	0,93
Fe-pyrr-NH$_3$	1,29	2,61	4,44	1,29	1,32	1,83	0,48
Co-pyrr-NH$_3$	1,76	3,37	4,76	1,76	1,61	1,39	0,16
Mn-pyrr-NH$_3$	1,38	2,57	4,5	1,38	1,19	1,93	0,42
Fe-pyri-NH$_3$	1,55	2,63	4,6	1,55	1,08	1,97	0,32
Co-pyriNH$_3$	1,7	3,3	4,72	1,7	1,6	1,42	0,2
Mn-pyriNH$_3$	1,1	2,3	4,29	1,1	1,2	1,99	0,63

Table 6-3: The theoretical overpotential for OER, Over$_{OER}$ and ORR, Over$_{ORR}$ for the test set of functionalised graphene.

System	Over$_{OER}$	Over$_{ORR}$
Fe-pyrr	2,5	0,38
Co-pyrr	1,58	0,43
Mn-pyrr	2,82	0,23
Fe-pyri	2,34	0,61
Co-pyri	1,49	0,66
Mn-pyri	2,65	0,36
Fe-pyrr-NH$_2$	2,11	0,77
Co-pyrr-NH$_2$	1,69	0,52
Mn-pyrr-NH$_2$	2,13	0,55
Fe-pyri-NH$_2$	2,31	0,69
Co-pyri-NH$_2$	1,63	0,6
Mn-pyri-NH$_2$	2,39	0,65
Fe-pyrr-NH$_3$	1,83	0,48
Co-pyrr-NH$_3$	1,76	0,16
Mn-pyrr-NH$_3$	1,93	0,42
Fe-pyri-NH$_3$	1,97	0,32
Co-pyriNH$_3$	1,7	0,2
Mn-pyriNH$_3$	1,99	0,63

The energies are obtained with DFT within the GPAW code using the RPBE functional [12]. A 2x2x1 k-point set with a 0.15 Å grid spacing was employed. The DFT calculation were spinpolarised system by providing an initial magnetic moment provided on the transition metal which was allowed to relax during optimisation using the BFGS algorithm.

To obtain the free energies the zero-point energies and entropy corrections are taken from literature [124]. It should be noted that for the calculation of the G_O energy an additional correction of 0.2 eV is added to the stability of the *=O intermediate. This is done to correct for the change in the number of possible hydrogen bonds from three for the *-OH and *-OOH intermediate to two for the *=O intermediate done in literature [69] for these types of systems.

The influence of a hydrogen transfer to an organic functional group is explored using the same test-set. Since the hydrogen transfer is assumed to only influence

G$_3$ the choice of descriptor (G$_1$ or G$_2$) is irrelevant. The transition metal doped graphene sheets and the hydrogen acceptor groups are treated as separate systems. There might be barriers associated with transferring hydrogens between the hydrogen acceptor groups and the transition metal placed in the functionalised graphene but they are not considered.

The three functional groups are selected to illustrate the influence of hydrogen acceptor on the OER and ORR mechanism. R-OH in the "on top" postion has a too high oxidation potential of 1.65 V, R-NH$_2$ in the edge position has a too low oxidation potential of 0.56 V and finally the R-COOH in the edge position which has a oxidation potential of 1.05 V.

The hydrogen transfer is assumed to only occurs in the third reaction step and only if the hydrogen transfer gives a lower energy when compared to the *-OOH intermediate. This true if sum of the oxidation potential of the functional group G$_{ox}$ and G$_O$ is lower than G$_{OOH}$

The effect of two of the functional groups R-NH$_2$ and R-OHis visualised in Figure 6.7 and 6.8 respectively. It is clearly seen that the addition of the functional group only improves the catalysts that are either limited by G$_3$ or G$_4$.
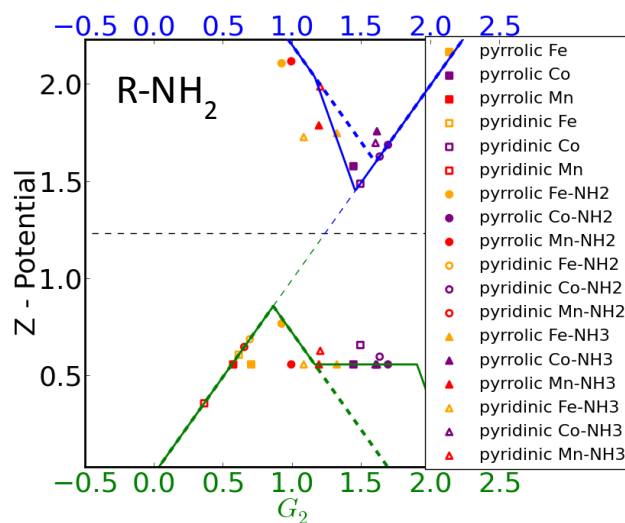
Figure 6.7 The effect of R-NH$_2$ in the edge position on the overpotential for functionalised graphene and the theoretical volcanoes for OER and ORR. The dashed lines display the theoretical volcanoes assuming the mononuclear mechanism and the continuous lines the theoretical volcanoes assuming the H transfer to the hydrogen acceptor groups.
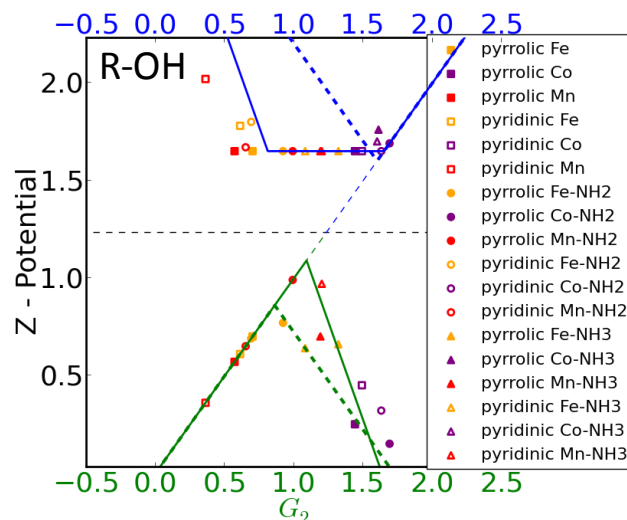
Figure 6.8: The effect of R-OH in the "on top" position on the overpotential for functionalised graphene and the theoretical volcanoes for OER and ORR. The dashed lines display the theoretical volcanoes assuming the mononuclear mechanism and the continuous lines the theoretical volcanoes assuming the H transfer to the hydrogen acceptor groups.
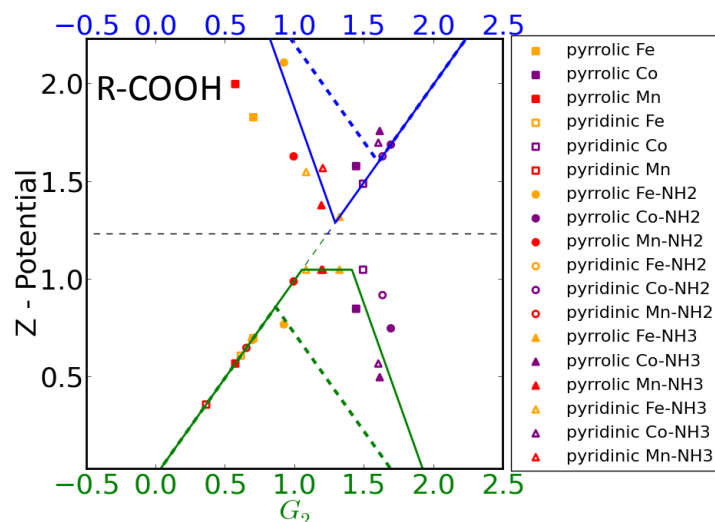
The overpotential for the oxygen reduction reaction can be improved by increasing the potential of the smallest reaction energy which explains the shoulder on the R-NH$_2$ volcano in Figure 6.7 as it enters the region where the oxidation potential of R-NH$_2$ of 0.65 eV becomes potential limiting instead of G$_3$ as seen by the dashed versus the continuous line. The low oxidation potential prevents overpotentials lower than the lowest predicted by the scaling relation. In the case of the R-OH displayed in Figure 6.8 the oxidation potential equals 1.65 eV. Here the new minimum overpotential achievable for the ORR is 1.09 V which is the case when the remaining binding energies G$_1$,G$_2$ G$_4$ are potential limiting.

For the oxygen evolution reaction another trend is observed since the overpotential since the largest binding energy in the reaction mechanism determines the overpotential. The lower oxidation potential from R-NH$_2$ gives a new minimum overpotential of 1.45V which is found when all the remaining three binding energies are potential limiting. The oxidation potential of the R-NH$_2$ almost equals the minimum overpotential dictated by the scaling relations for OER. This creates a very large range of G$_2$ (almost 1 eV) in which catalysts has a moderate overpotential.

For a more ideal oxidation potential the R-COOH positioned on the edge has an oxidation of 1.05 eV is shown in figure 6.9. This gives a much lower possible overpotential and the possibility for creating bifunctional catalysts. Pyrrolic Fe

with an additional NH_3 ligand with only a 0.1 V overpotential for ORR and a 0.2 V overpotential for the OER.

Figure 6.9: The effect of the oxidation potential of the R-COOH on the edge position on the overpotential for the functionalised graphene sheets. The dashed lines display the theoretical volcanoes assuming the mononuclear mechanism and the continuous lines the theoretical volcanoes assuming the H transfer to the hydrogen acceptor groups.

This analysis show that existing catalysts can be improved by the addition of a functional group which enables hydrogen transfers at a given potential, it also provides some interesting design options. The ideal catalyst could be achieved using by designing a functional group with the optimal oxidation potential of 1.23 eV. This would require a catalyst with optimal binding energies of G_1, G_2 and G_4 which might not be possible. It was assumed that G_1 equal G_2 is not always true so achieving the perfect catalyst might not be possible.

Another option could be to find a functional group like the R-OH for the oxygen evolution reaction which activates a large range of catalysts to a moderate overpotential, due to the large tolerance in changes to the binding energies. It also lessens the requirements for the accuracy in determining the binding energies. DFT only have a limited accuracy and more advanced methods would be required design the ideal catalyst. The functionalised graphene sheets offer some flexibility in design and could be a promising class of materials for the ORR and possibly the OER as well since they offer the possibility for insertion of functional groups during synthesis. This creates a special active site which effectively bypasses the scaling relations observed in the mononuclear mechanism. Stability is still something that needs to be investigated to truly replace noble metals and noble metal oxides for oxygen electrocatalysis.

It seems possible that photosystem II would be able to use H acceptors to tune the activity of centre Mn_4Ca cluster beyond the scaling relations, based on experimental measurements for the states Y_zS_0, Y_zS_1, Y_zS_2, Y_zS_3 [131] which thermodynamically corresponds to the adsorption energies of *, *-OH, *=O and *-OOH. The energy level are shown in Figure 6.10 at pH = 7 which is the physiological pH and pH = 0 to better compare with other inorganic OER catalysts. The conversion between pH levels is done using the Nernst equation. At pH = 7 the offset between the states Y_zS_1 and Y_zS_2 corresponding *-OH and *-OOH, equals 3.1 eV is also observed for photosystem II. The binding energy between Y_zS_2 and Y_zS_1 corresponding to the energy between G_O and G_{OH} equal 1.5 eV. This result in overpotential of 0.33V which is a little above the apex of the theoretical volcano for the mononuclear mechanism.
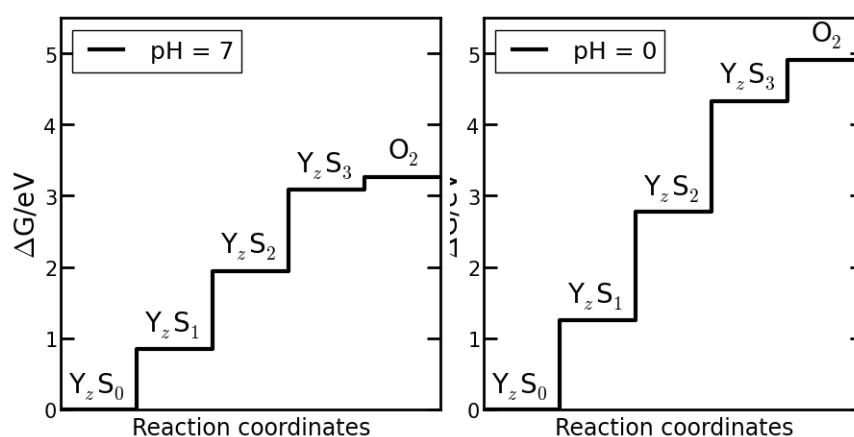
Figure 6.10: The energy levels for OER corresponding to *, *-OH, *=O, *-OOH and O$_2$. The adsorption energies compared to the reference state are at pH = 7, 0.86 eV, 1.95 eV and 3.1 eV and at pH = 0, 1.26 eV, 2.78 eV and 4.34 eV. The offset between *-OH and *-OOH or Y$_z$S$_1$ and Y$_z$S$_3$ is 3.1 eV. Data based obtained from literature[131]**.**

Photosystem II, at least according to the analysis done here and the observed overpotentials [100] of around 0.4-0.5V, obeys the scaling relations between *-OH and *-OOH. This means that Photosystem II does not utilise a hydrogen transfer mechanism to increase the efficiency of OER beyond what is possible by the mononuclear mechanism. This is despite of the nearby surroundings with all the functional sidegroups of the amino acids around the active site [132]. To compare this analysis show that a Mn ion in a pyrrolic environment with an addition ammonia ligand using a carboxylic acid as a hydrogen acceptor could have an overpotential for OER as low as 0.1 V.

Functionalised graphene have been investigated as another class of catalysts that could be used for the ORR and OER. The 3.2 eV offset between *-OH and *-OOH

can be bypassed using a hydrogen acceptor functional group which in principle should be able to be synthesised directly on the graphene sheet. Despite the catalysts similarity to proteins and Photosystem II, Photosystem II does not seem to have an activity improved by functional groups.

Based on the work on functionalised graphene sheets some design rules have been proposed for future catalyst design. In order to improve the theoretical overpotential of oxygen electrocatalysis the oxidation potential should be lower than 1.23V to improve the ORR and higher than 1.23 V to improve the OER. The optimal for both OER and ORR is exactly 1.23 V. In principle, a catalyst could be designed with exactly the right binding energies to achieve this. Another option is to have a hydrogen acceptor potential like R-OH for the OER. Using R-OH as a hydrogen acceptor does not give overpotentials lower than the 0.4 but enables several catalysts with reaction energies in a large potential range in this case of 0.6-1.6 eV to achieve reasonable overpotentials.

7 Conclusion and outlook

In this thesis it has been demonstrated that the constant offset of 3.2 eV between the *-OH and *-OOH intermediate can be bypassed by the use of specially designed active sites. A local structure motif containing an active site for O containing species and a site which can accepts H nearby creates the possibility for H transfers during OER or ORR. This changes the reaction mechanism from a mononuclear mechanism to a binuclear mechanism. The binding of *-OH and the binding *-OOH is decoupled since the *-OOH intermediate is never formed on the surface. This decoupling enables the design of catalytically active sites that have a theoretical overpotential below 0.4 V which was previously believed to be lowest achievable overpotential.

As a proof of concept, the systems; Ni and Co modified RuO_2 and MnO_x and CoO_x in the vicinity of Au was investigated. Experimental work showed an improvement towards OER and the H acceptor functionality nearby the active site was proposed as the reason for the increased activity towards OER.

The special active site concept have also been shown to explain the preference for producing H_2O_2 at high overpotential on Ni and Co modified RuO_2 compared to conventional RuO_2, further supporting the validity of the model system used in the DFT calculations.

The addition of the H acceptor functionality not only increases the OER activity it also shifts the ideal binding energies. Based on the scaling relations the ideal reaction energy for the formation of the *=O intermediate from the *-OH intermediate is 1.6 eV. This is unfortunate as it is the rare catalysts materials such as RuO_2 and IrO_2 have binding energies in that region. The addition of a H-acceptor functionality allows catalysts with lower binding energies to become activated towards oxygen evolution which raises prospect of designing a cheap, abundant and highly active OER catalyst in the near future. The principle might even be transferable to other electrocatalytic reactions such as CO_2 reduction.

Further work should focus on promoting special active sites with a very high activity towards OER or ORR on the surface relative to the bulk to further improve the overall activity of catalysts. In the case of Ni and Co modified RuO_2 the overall activity was shown to be governed by the number of these special active sites on the surface.

8 Bibliography

[1]   International Energy Agency, "Key World Energy Statistics," Paris, 2014.

[2]   N. S. Lewis and D. G. Nocera, "Correction for Lewis and Nocera, Powering the planet: Chemical challenges in solar energy utilization," *Proc. Natl. Acad. Sci.*, vol. 104, no. 50, pp. 20142–20142, Nov. 2007.

[3]   T. F. Stocker, D. Qin, G.-K. Plattner, M. Tignor, S. K. Allen, J. Boschung, A. Nauels, Y. Xia, V. Bex, and P. M. Midgley, *Climate Change 2013: The Physical Science Basis. Contribution of Working Group I to the Fifth Assessment Report of the intergovernmental Panel of Climate Change*. Cambridge and New York: Cambridge University Press, 2013, pp. 1–1535.

[4]   N. Armaroli and V. Balzani, "The future of energy supply: Challenges and opportunities.," *Angew. Chem. Int. Ed. Engl.*, vol. 46, no. 1–2, pp. 52–66, Jan. 2007.

[5]   P. C. K. Vesborg and T. F. Jaramillo, "Addressing the terawatt challenge: scalability in the supply of chemical elements for renewable energy," *RSC Adv.*, vol. 2, no. 21, p. 7933, 2012.

[6]   The Danish Government, "Energy Strategy 2050 - from coal, oil and gas to green energy," 2011.

[7]   E. Schrödinger, "An Undulatory Theory of the Mechanics of Atoms and Molecules," *Phys. Rev.*, vol. 26, no. 6, p. 1049, 1926.

[8]   M. Born and R. Oppenheimer, "Zur Quantentheorie der Molekeln," *Ann. Phys.*, vol. 84, no. 20, p. 457, 1927.

[9]   K. Hohenberg and W. Kohn, "No Title," *Inhomogeneous electron gas*, vol. 136, no. 3B, p. B864, 1964.

[10]   W. Kohn and L. J. Sham, "Self-consistent equations including exchange and correlation effects," *Phys. Rev.*, vol. 140, p. A1133, 1965.

[11]   J. P. Perdew, K. Burke, and M. Ernzerhof, "Generalized Gradient Approximation Made Simple," *Phys. Rev. Lett.*, vol. 77, no. 18, pp. 3865–3868, Oct. 1996.

[12]   B. Hammer, L. Hansen, and J. Nørskov, "Improved adsorption energetics within density-functional theory using revised Perdew-Burke-Ernzerhof functionals," *Phys. Rev. B*, vol. 59, no. 11, pp. 7413–7421, Mar. 1999.

[13]   Y. K. Zhang and W. T. Yang, "Comment on 'Generalized gradient approximation made simple,'" *Phys. Rev. Lett.*, vol. 80, no. 4, 1998.

[14]   K. Burke, *The ABC of DFT*. 2007.

[15]   F. Bloch, "Über die Quantenmechanik der Elektronen in Kristallgittern," *Zeitschrift für Phys.*, vol. 52, no. 7.8, pp. 555–600, 1929.

[16]   J. Enkovaara, C. Rostgaard, J. J. Mortensen, J. Chen, M. Dułak, L. Ferrighi, J. Gavnholt, C. Glinsvad, V. Haikola, H. A. Hansen, H. H. Kristoffersen, M. Kuisma, A. H. Larsen, L. Lehtovaara, M. Ljungberg, O. Lopez-Acevedo, P. G. Moses, J. Ojanen, T. Olsen, V. Petzold, N. A. Romero, J. Stausholm-Møller, M. Strange, G. A. Tritsaris, M. Vanin, M. Walter, B. Hammer, H. Häkkinen, G. K. H. Madsen, R. M. Nieminen, J. K. Nørskov, M. Puska, T. T. Rantala, J. Schiøtz, K. S. Thygesen, and K. W. Jacobsen, "Electronic structure calculations with GPAW: a real-space implementation of the projector augmented-wave method.," *J. Phys. Condens. Matter*, vol. 22, no. 25, p. 253202, Jun. 2010.

[17]   P. E. Blochl, "Projector Augmented Wave-method," *Phys. Rev. B*, vol. 50, no. 24, pp. 17953 – 17979, 1994.

[18]   D. Vanderbilt, "Soft Self-consistent Pseudopotentials in a Generalized Eigenvalue Formalism," *Phys. Rev. B*, vol. 41, no. 11, pp. 7892 – 7895, 1990.

[19]   W. R. Fawcett, "The ionic work function and its role in estimating absolute electrode potentials.," *Langmuir*, vol. 24, no. 17, pp. 9868–75, Sep. 2008.

[20]   A. A. Isse and A. Gennaro, "Absolute potential of the standard hydrogen electrode and the problem of interconversion of potentials in different solvents.," *J. Phys. Chem. B*, vol. 114, no. 23, pp. 7894–9, Jun. 2010.

[21]   P. Atkins and J. de Paula, *Atkins' Physical Chemistry*, 6th editio. Oxford University Press, 2002.

[22]   S. Kurth, J. P. Perdew, and P. Blaha, "Molecular and solid-state tests of density functional approximations: LSD, GGAs, and meta-GGAs," *Int. J. Quantum Chem.*, vol. 75, no. 4-5, p. 889, 1999.

[23]   A. Kirubakaran, S. Jain, and R. K. Nema, "A review on fuel cell technologies and power electronic interface," *Renew. Sustain. Energy Rev.*, vol. 13, no. 9, pp. 2430–2440, Dec. 2009.

[24]   Y. Wang, K. S. Chen, J. Mishler, S. C. Cho, and X. C. Adroher, "A review of polymer electrolyte membrane fuel cells: Technology, applications, and

needs on fundamental research," *Appl. Energy*, vol. 88, no. 4, pp. 981–1007, Apr. 2011.

[25] A. Ursúa, L. M. Gandia, and P. Sanchis, "Hydrogen Production from Water Electrolysis : Current Status and Future Trends," *Proc. IEEE*, vol. 100, no. 2, pp. 410–426, 2012.

[26] J. R. Varcoe and R. C. T. Slade, "Prospects for Alkaline Anion-Exchange Membranes in Low Temperature Fuel�Cells," *Fuel Cells*, vol. 5, no. 2, pp. 187–200, Apr. 2005.

[27] K. E. Ayers, E. B. Anderson, C. Capuano, B. Carter, L. Dalton, G. Hanlon, J. Manco, and M. Niedzwiecki, "Research Advances towards Low Cost, High Efficiency PEM Electrolysis," in *POLYMER ELECTROLYTE FUEL CELLS 10, PTS 1 AND 2*, 2010, vol. 33, no. 1, pp. 3–15.

[28] T. Gierke, "Ionic clustering in Nafion perfluorosulfonic acid and its relationship to hydroxyl rejection and chlor-alkali current efficiency," *J. Electrochem. Soc.*, vol. 124, no. 8, pp. C319–C319, 1977.

[29] M. Carmo, D. L. Fritz, J. Mergel, and D. Stolten, "A comprehensive review on PEM water electrolysis," *Int. J. Hydrogen Energy*, vol. 38, no. 12, pp. 4901–4934, Apr. 2013.

[30] S. Trasatti, "Electrocatalysis: understanding the success of DSA (R)," *Electrochim. Acta*, vol. 45, no. 15–16, pp. 2377 – 2385, 2000.

[31] F. Barbir, "PEM electrolysis for production of hydrogen from renewable energy sources," *Sol. Energy*, vol. 78, no. 5, pp. 661–669, May 2005.

[32] T. Tingelöf, L. Hedström, N. Holmström, P. Alvfors, and G. Lindbergh, "The influence of CO2, CO and air bleed on the current distribution of a polymer electrolyte fuel cell," *Int. J. Hydrogen Energy*, vol. 33, no. 8, pp. 2064–2072, Apr. 2008.

[33] A. Marshall, B. Børresen, G. Hagen, M. Tsypkin, and R. Tunold, "Hydrogen production by advanced proton exchange membrane (PEM) water electrolysers—Reduced energy consumption by improved electrocatalysis," *Energy*, vol. 32, no. 4, pp. 431–436, Apr. 2007.

[34] M. G. Walter, E. L. Warren, J. R. McKone, S. W. Boettcher, Q. Mi, E. A. Santori, and N. S. Lewis, "Solar water splitting cells.," *Chem. Rev.*, vol. 110, no. 11, pp. 6446–73, Nov. 2010.

[35] R. V., "Fuel Cells," *Electrochem. Soc. Interface*, vol. 15, no. 1, pp. 41–44, 2006.

[36] J. K. Nørskov, J. Rossmeisl, A. Logadottir, L. Lindqvist, J. R. Kitchin, T. Bligaard, and H. Jónsson, "Origin of the Overpotential for Oxygen Reduction at a Fuel-Cell Cathode," *J. Phys. Chem. B*, vol. 108, no. 46, pp. 17886–17892, Nov. 2004.

[37] I. C. Man, H.-Y. Su, F. Calle-Vallejo, H. A. Hansen, J. I. Martínez, N. G. Inoglu, J. Kitchin, T. F. Jaramillo, J. K. Nørskov, and J. Rossmeisl, "Universality in Oxygen Evolution Electrocatalysis on Oxide Surfaces," *ChemCatChem*, vol. 3, no. 7, pp. 1159–1165, Jul. 2011.

[38] J. Rossmeisl, K. Chan, R. Ahmed, V. Tripković, and M. E. Björketun, "pH in atomic scale simulations of electrochemical interfaces.," *Phys. Chem. Chem. Phys.*, vol. 15, no. 25, pp. 10321–5, Jul. 2013.

[39] H. a. Gasteiger, S. S. Kocha, B. Sompalli, and F. T. Wagner, "Activity benchmarks and requirements for Pt, Pt-alloy, and non-Pt oxygen reduction catalysts for PEMFCs," *Appl. Catal. B Environ.*, vol. 56, no. 1–2, pp. 9–35, Mar. 2005.

[40] M. Piana, S. Catanorchi, and H. A. Gasteiger, "Kinetics of Non-Platinum Group Metal Catalysts for the Oxygen Reduction Reaction in Alkaline Medium," in *ECS Transactions*, 2008, vol. 16, no. 2, pp. 2045–2055.

[41] T. R. Cook, D. K. Dogutan, S. Y. Reece, Y. Surendranath, T. S. Teets, and D. G. Nocera, "Solar energy supply and storage for the legacy and nonlegacy worlds.," *Chem. Rev.*, vol. 110, no. 11, pp. 6474–502, Nov. 2010.

[42] J. K. Nørskov, J. Rossmeisl, A. Logadottir, L. Lindqvist, J. R. Kitchin, T. Bligaard, and H. Jónsson, "Origin of the Overpotential for Oxygen Reduction at a Fuel-Cell Cathode," *J. Phys. Chem. B*, vol. 108, no. 46, pp. 17886–17892, Nov. 2004.

[43] V. Viswanathan, H. A. Hansen, J. Rossmeisl, and J. K. Nørskov, "Universality in Oxygen Reduction Electrocatalysis on Metal Surfaces," *ACS Catal.*, vol. 2, no. 8, pp. 1654–1660, Aug. 2012.

[44] J. Nørskov, "Universality in Heterogeneous Catalysis," *J. Catal.*, vol. 209, no. 2, pp. 275–278, Jul. 2002.

[45] J. K. Nørskov, T. Bligaard, J. Rossmeisl, and C. H. Christensen, "Towards the computational design of solid catalysts.," *Nat. Chem.*, vol. 1, no. 1, pp. 37–46, Apr. 2009.

[46] A. J. Medford, J. Wellendorff, A. Vojvodic, F. Studt, F. Abild-Pedersen, K. W. Jacobsen, T. Bligaard, and J. K. Nørskov, "Catalysis. Assessing the

reliability of calculated catalytic ammonia synthesis rates.," *Science*, vol. 345, no. 6193, pp. 197–200, Jul. 2014.

[47]   B. Hammer and J. K. Nørskov, "Electronic factors determining the reactivity of metal surfaces," *Surf. Sci.*, vol. 343, no. 3, pp. 211–220, Dec. 1995.

[48]   B. Hammer and J. K. Nørskov, "Why Gold is the Noblest of all the Metals," *Nature*, vol. 376, no. 6537, pp. 238 – 240, 1995.

[49]   J. K. Nørskov, T. Bligaard, B. Hvolbaek, F. Abild-Pedersen, I. Chorkendorff, and C. H. Christensen, "The nature of the active site in heterogeneous metal catalysis.," *Chem. Soc. Rev.*, vol. 37, no. 10, pp. 2163–71, Oct. 2008.

[50]   I. E. L. Stephens, A. S. Bondarenko, U. Grønbjerg, J. Rossmeisl, and I. Chorkendorff, "Understanding the electrocatalysis of oxygen reduction on platinum and its alloys," *Energy Environ. Sci.*, vol. 5, no. 5, p. 6744, 2012.

[51]   M. Escudero-Escribano, A. Verdaguer-Casadevall, P. Malacrida, U. Grønbjerg, B. P. Knudsen, A. K. Jepsen, J. Rossmeisl, I. E. L. Stephens, and I. Chorkendorff, "Pt5Gd as a highly active and stable catalyst for oxygen electroreduction.," *J. Am. Chem. Soc.*, vol. 134, no. 40, pp. 16476–9, Oct. 2012.

[52]   P. Strasser, S. Koh, T. Anniyev, J. Greeley, K. More, C. Yu, Z. Liu, S. Kaya, D. Nordlund, H. Ogasawara, M. F. Toney, and A. Nilsson, "Lattice-strain control of the activity in dealloyed core-shell fuel cell catalysts.," *Nat. Chem.*, vol. 2, no. 6, pp. 454–60, Jun. 2010.

[53]   N. Danilovic, R. Subbaraman, K.-C. Chang, S. H. Chang, Y. J. Kang, J. Snyder, A. P. Paulikas, D. Strmcnik, Y.-T. Kim, D. Myers, V. R. Stamenkovic, and N. M. Markovic, "Activity–Stability Trends for the Oxygen Evolution Reaction on Monometallic Oxides in Acidic Environments," *J. Phys. Chem. Lett.*, vol. 5, no. 14, pp. 2474–2478, Jul. 2014.

[54]   J. Durst, M. Lopez-Haro, L. Dubau, M. Chatenet, Y. Soldo-Olivier, L. Guétaz, P. Bayle-Guillemaud, and F. Maillard, "Reversibility of Pt-Skin and Pt-Skeleton Nanostructures in Acidic Media," *J. Phys. Chem. Lett.*, vol. 5, no. 3, pp. 434–439, Feb. 2014.

[55]   J. R. Kitchin, J. K. Nørskov, M. A. Barteau, and J. G. Chen, "Role of strain and ligand effects in the modification of the electronic and chemical Properties of bimetallic surfaces," *Phys. Rev. Lett.*, vol. 93, no. 15, 2004.

[56]   H. Hartmann, T. Diemant, J. Bansmann, and R. J. Behm, "Chemical properties of structurally well-defined PdRu/Ru(0001) surface alloys –

Interaction with CO," *Surf. Sci.*, vol. 603, no. 10–12, pp. 1456–1466, Jun. 2009.

[57]   S. Kumar and S. Zou, "Electrooxidation of carbon monoxide and methanol on platinum-overlayer-coated gold nanoparticles: effects of film thickness.," *Langmuir*, vol. 23, no. 13, pp. 7365–71, Jun. 2007.

[58]   L. Gan, M. Heggen, S. Rudi, and P. Strasser, "Core-shell compositional fine structures of dealloyed Pt(x)Ni(1-x) nanoparticles and their impact on oxygen reduction catalysis.," *Nano Lett.*, vol. 12, no. 10, pp. 5423–30, Oct. 2012.

[59]   C. C. Chang and T. C. Wen, "Kinetics of oxygen reduction at IrO2-coated titanium electrode in alkaline solution," *J. Electrochem. Soc.*, vol. 143, no. 5, pp. 1485 – 1491, 1996.

[60]   C. C. Chang and T. C. Wen, "Kinetics of oxygen reduction at RuO2-coated titanium electrode in alkaline solution," *J. Appl. Electrochem.*, vol. 27, no. 3, pp. 355 – 363, 1997.

[61]   N. Yoshinaga, W. Sugimoto, and Y. Takasu, "Oxygen reduction behavior of rutile-type iridium oxide in sulfuric acid solution," *Electrochim. Acta*, vol. 54, no. 2, pp. 566–573, Dec. 2008.

[62]   J. Suntivich, K. J. May, H. A. Gasteiger, J. B. Goodenough, and Y. Shao-Horn, "A perovskite oxide optimized for oxygen evolution catalysis from molecular orbital principles.," *Science*, vol. 334, no. 6061, pp. 1383–5, Dec. 2011.

[63]   F. Cheng, J. Shen, B. Peng, Y. Pan, Z. Tao, and J. Chen, "Rapid room-temperature synthesis of nanocrystalline spinels as oxygen reduction and evolution electrocatalysts.," *Nat. Chem.*, vol. 3, no. 1, pp. 79–84, Jan. 2011.

[64]   M. Hamdani, "Co3O4 and Co- Based Spinel Oxides Bifunctional Oxygen Electrodes," *Int. J. Electrochem. Sci.*, vol. 5, no. 4, pp. 556 – 577, 2010.

[65]   H. S. Horowitz, J. M. Longo, and H. H. Horowitz, "OXYGEN ELECTROCATALYSIS ON SOME OXIDE PYROCHLORES," *J. Electrochem. Soc.*, vol. 130, no. 9, pp. 1851 – 1859, 1983.

[66]   J. P. Collman, L. L. Chng, and D. A. Tyvoll, "Electroctalytic Reduction of Dioxygen to Water by Iridium Porphyrines Adsorbed on Edge Plane Graphite Electrodes," *Inorg. Chem.*, vol. 34, no. 6, pp. 1311 – 1324, 1995.

[67]   A. Choi, H. Jeong, S. Kim, S. Jo, and S. Jeon, "Electrocatalytic reduction of dioxygen by cobalt porphyrin-modified glassy carbon electrode with

single-walled carbon nanotubes and nafion in aqueous solutions," *Electrochim. Acta*, vol. 53, no. 5, pp. 2579–2584, Jan. 2008.

[68]   J. D. Baran, H. Grönbeck, and A. Hellman, "Analysis of Porphyrines as Catalysts for Electrochemical Reduction of," *J. Am. Chem. Soc.*, vol. 136, pp. 1320–1326, 2014.

[69]   F. Calle-Vallejo, J. I. Martínez, and J. Rossmeisl, "Density functional studies of functionalized graphitic materials with late transition metals for Oxygen Reduction Reactions.," *Phys. Chem. Chem. Phys.*, vol. 13, no. 34, pp. 15639–43, Sep. 2011.

[70]   H. He, Y. Lei, C. Xiao, D. Chu, R. Chen, and G. Wang, "Molecular and Electronic Structures of Transition-Metal Macrocyclic Complexes as Related to Catalyzing Oxygen Reduction Reactions: A Density Functional Theory Study," *J. Phys. Chem. C*, vol. 116, no. 30, pp. 16038–16046, Aug. 2012.

[71]   S. Siahrostami, A. Verdaguer-Casadevall, M. Karamad, D. Deiana, P. Malacrida, B. Wickman, M. Escudero-Escribano, E. a Paoli, R. Frydendal, T. W. Hansen, I. Chorkendorff, I. E. L. S. Stephens, I. E. Stephens, and J. Rossmeisl, "Enabling direct H2O2 production through rational electrocatalyst design.," *Nat. Mater.*, vol. 12, no. 12, pp. 1137–43, Dec. 2013.

[72]   D. H. Lee, W. J. Lee, W. J. Lee, S. O. Kim, and Y.-H. Kim, "Theory, Synthesis, and Oxygen Reduction Catalysis of Fe-Porphyrin-Like Carbon Nanotube," *Phys. Rev. Lett.*, vol. 106, no. 17, p. 175502, Apr. 2011.

[73]   M. H. Miles and M. A. Thomason, "Periodic Variations of Overvoltages for Water Electrolysis in Acid Solutions from Cyclic Voltammetry Studies," *J. Electrochem. Soc.*, vol. 123, no. 10, pp. 1459 – 1461, 1976.

[74]   S. Cherevko, A. R. Zeradjanin, A. A. Topalov, N. Kulyk, I. Katsounaros, and K. J. J. Mayrhofer, "Dissolution of Noble Metals during Oxygen Evolution in Acidic Media," *ChemCatChem*, vol. 6, no. 8, p. n/a–n/a, Jul. 2014.

[75]   S. Trasatti, "Electrocatalysis in the Anodic Evolution of Ozygen and Chlorine," *Electrochim. Acta*, vol. 29, no. 11, pp. 1503 – 1512, 1984.

[76]   Y. Matsumoto and E. Sato, "Electrocatalytic Properties of Transition-metal Oxides for Oxygen Evolution Reaction," *Mater. Chem. Phys.*, vol. 14, no. 5, pp. 397 – 426, 1986.

76

[77] O. Diaz-Morales, F. Calle-Vallejo, C. de Munck, and M. T. M. Koper, "Electrochemical water splitting by gold: evidence for an oxide decomposition mechanism," *Chem. Sci.*, vol. 4, no. 6, p. 2334, 2013.

[78] S. Trasatti, "Electrocatalysis: understanding the success of DSA®," *Electrochim. Acta*, vol. 45, no. 15–16, pp. 2377–2385, May 2000.

[79] R. D. L. Smith, M. S. Prévot, R. D. Fagan, Z. Zhang, P. A. Sedach, M. K. J. Siu, S. Trudel, and C. P. Berlinguette, "Photochemical route for accessing amorphous metal oxide materials for water oxidation catalysis.," *Science*, vol. 340, no. 6128, pp. 60–3, Apr. 2013.

[80] R. Subbaraman, D. Tripkovic, K.-C. Chang, D. Strmcnik, A. P. Paulikas, P. Hirunsit, M. Chan, J. Greeley, V. Stamenkovic, and N. M. Markovic, "Trends in activity for the water electrolyser reactions on 3d M(Ni,Co,Fe,Mn) hydr(oxy)oxide catalysts.," *Nat. Mater.*, vol. 11, no. 6, pp. 550–7, Jun. 2012.

[81] E. M. Fernández, P. G. Moses, A. Toftelund, H. a Hansen, J. I. Martínez, F. Abild-Pedersen, J. Kleis, B. Hinnemann, J. Rossmeisl, T. Bligaard, and J. K. Nørskov, "Scaling relationships for adsorption energies on transition metal oxide, sulfide, and nitride surfaces.," *Angew. Chem. Int. Ed. Engl.*, vol. 47, no. 25, pp. 4683–6, Jan. 2008.

[82] A. Vojvodic, C. Ruberto, and B. I. Lundqvist, "Atomic and molecular adsorption on transition-metal carbide (111) surfaces from density-functional theory: a trend study of surface electronic factors.," *J. Phys. Condens. Matter*, vol. 22, no. 37, p. 375504, Sep. 2010.

[83] A. Grimaud, K. J. May, C. E. Carlton, Y.-L. Lee, M. Risch, W. T. Hong, J. Zhou, and Y. Shao-Horn, "Double perovskites as a family of highly active catalysts for oxygen evolution in alkaline solution.," *Nat. Commun.*, vol. 4, no. May, p. 2439, Jan. 2013.

[84] J. Bockris and T. Otagawa, "The electrocatalysis of oxygen evolution on perovskites," *J. Electrochem. Soc.*, vol. 131, no. 2, pp. 290–302, 1984.

[85] J. Suntivich, K. J. May, H. a Gasteiger, J. B. Goodenough, and Y. Shao-Horn, "A perovskite oxide optimized for oxygen evolution catalysis from molecular orbital principles.," *Science*, vol. 334, no. 6061, pp. 1383–5, Dec. 2011.

[86] Y.-F. Li and A. Selloni, "Mechanism and Activity of Water Oxidation on Selected Surfaces of Pure and Fe-Doped NiO x," *ACS Catal.*, vol. 4, no. 4, pp. 1148–1153, Apr. 2014.

[87]   P. Liao, J. A. Keith, and E. A. Carter, "Water Oxidation on Pure and Doped Hematite (0001) Surfaces : Prediction of Co and Ni as E ff ective Dopants for Electrocatalysis," no. 0001, 2012.

[88]   M. Bajdich, M. García-Mota, A. Vojvodic, J. K. Nørskov, and A. T. Bell, "Theoretical investigation of the activity of cobalt oxides for the electrochemical oxidation of water.," *J. Am. Chem. Soc.*, vol. 135, no. 36, pp. 13521–30, Sep. 2013.

[89]   M. García-Mota, M. Bajdich, V. Viswanathan, A. Vojvodic, A. T. Bell, and J. K. Nørskov, "Importance of Correlation in Determining Electrocatalytic Oxygen Evolution Activity on Cobalt Oxides," *J. Phys. Chem. C*, vol. 116, no. 39, pp. 21077–21082, Oct. 2012.

[90]   A. I. Liechtenstein, V. I. Anisimov, and J. Zaanen, "Density-functional theory and strong interactions: Orbital ordering in Mott-Hubbard insulators," *Phys. Rev. B*, vol. 52, no. 8, pp. R5467–R5470, 1995.

[91]   L. Wang, T. Maxisch, and G. Ceder, "Oxidation energies of transition metal oxides within the GGA+U framework," *Phys. Rev. B*, vol. 73, no. 19, p. 195107, May 2006.

[92]   M. Cococcioni and S. de Gironcoli, "Linear response approach to the calculation of the effective interaction parameters in the LDA+U method," *Phys. Rev. B*, vol. 71, no. 3, p. 035105, Jan. 2005.

[93]   C. C. L. McCrory, S. Jung, J. C. Peters, and T. F. Jaramillo, "Benchmarking heterogeneous electrocatalysts for the oxygen evolution reaction.," *J. Am. Chem. Soc.*, vol. 135, no. 45, pp. 16977–87, Nov. 2013.

[94]   R. Frydendal, E. A. Paoli, B. P. Knudsen, B. Wickman, P. Malacrida, I. E. L. Stephens, and I. Chorkendorff, "Benchmarking the Stability of Oxygen Evolution Reaction Catalysts: The Importance of Monitoring Mass Losses," *ChemElectroChem*, p. n/a–n/a, Oct. 2014.

[95]   E. a. Paoli, F. Masini, R. Frydendal, D. Deiana, C. Schlaup, M. Malizia, T. W. Hansen, S. Horch, I. E. L. Stephens, and I. Chorkendorff, "Oxygen evolution on well-characterized mass-selected Ru and RuO 2 nanoparticles," *Chem. Sci.*, vol. 6, pp. 190–196, Sep. 2014.

[96]   H. N. Nong, L. Gan, E. Willinger, D. Teschner, and P. Strasser, "IrOx core-shell nanocatalysts for cost- and energy-efficient electrochemical water splitting," *Chem. Sci.*, vol. 5, no. 8, p. 2955, 2014.

[97] Z. Zhuang, W. Sheng, and Y. Yan, "Synthesis of monodispere Au@Co3O4 core-shell nanocrystals and their enhanced catalytic activity for oxygen evolution reaction.," *Adv. Mater.*, vol. 26, no. 23, pp. 3950–5, Jun. 2014.

[98] K. A. Stoerzinger, L. Qiao, M. D. Biegalski, and Y. Shao-horn, "Orientation-Dependent Oxygen Evolution Activities of Rutile IrO 2," no. 110, pp. 0–5, 2014.

[99] J. Yano, J. Kern, K. Sauer, M. J. Latimer, Y. Pushkar, J. Biesiadka, B. Loll, W. Saenger, J. Messinger, A. Zouni, and V. K. Yachandra, "Where water is oxidized to dioxygen: structure of the photosynthetic Mn4Ca cluster.," *Science*, vol. 314, no. 5800, pp. 821–5, Nov. 2006.

[100] F. Rappaport, M. Guergova-Kuras, P. J. Nixon, B. A. Diner, and J. Lavergne, "Kinetics and Pathways of Charge Recombination in Photosystem II †," *Biochemistry*, vol. 41, no. 26, pp. 8518–8527, Jul. 2002.

[101] F. M. Toma, A. Sartorel, M. Iurlo, M. Carraro, P. Parisse, C. Maccato, S. Rapino, B. R. Gonzalez, H. Amenitsch, T. Da Ros, L. Casalis, A. Goldoni, M. Marcaccio, G. Scorrano, G. Scoles, F. Paolucci, M. Prato, and M. Bonchio, "Efficient water oxidation at carbon nanotube-polyoxometalate electrocatalytic interfaces.," *Nat. Chem.*, vol. 2, no. 10, pp. 826–31, Oct. 2010.

[102] E. M. Aro, I. Virgin, and B. Anderson, "Photoinhibition of Photosystem II. Inactivation, protein damage and turnover.," *Biochim. Biophys. Acta*, vol. 1143, no. 2, pp. 113 – 134, 1993.

[103] D. G. Nocera, "The artificial leaf.," *Acc. Chem. Res.*, vol. 45, no. 5, pp. 767–76, May 2012.

[104] H. Dau and I. Zaharieva, "Principles, efficiency, and blueprint character of solar-energy conversion in photosynthetic water oxidation.," *Acc. Chem. Res.*, vol. 42, no. 12, pp. 1861–70, Dec. 2009.

[105] M. M. Najafpour, T. Ehrenberg, M. Wiechen, and P. Kurz, "Calcium manganese(III) oxides (CaMn2O4.xH2O) as biomimetic oxygen-evolving catalysts.," *Angew. Chem. Int. Ed. Engl.*, vol. 49, no. 12, pp. 2233–7, Mar. 2010.

[106] R. E. Hansen and S. Das, "Biomimetic di-manganese catalyst cage-isolated in a MOF: robust catalyst for water oxidation with Ce(iv), a non-O-donating oxidant," *Energy Environ. Sci.*, vol. 7, no. 1, p. 317, 2014.

[107] D. Shevchenko, M. F. Anderlund, S. Styring, H. Dau, I. Zaharieva, and A. Thapper, "Water oxidation by manganese oxides formed from

tetranuclear precursor complexes: the influence of phosphate on structure and activity.," *Phys. Chem. Chem. Phys.*, vol. 16, no. 24, pp. 11965–75, Jun. 2014.

[108] H. Dau, C. Limberg, T. Reier, M. Risch, S. Roggan, and P. Strasser, "The Mechanism of Water Oxidation: From Electrolysis via Homogeneous to Biological Catalysis," *ChemCatChem*, vol. 2, no. 7, pp. 724–761, Jun. 2010.

[109] M. Dincă, Y. Surendranath, and D. G. Nocera, "Nickel-borate oxygen-evolving catalyst that functions under benign conditions.," *Proc. Natl. Acad. Sci. U. S. A.*, vol. 107, no. 23, pp. 10337–41, Jun. 2010.

[110] D. A. Lutterman, Y. Surendranath, and D. G. Nocera, "A self-healing oxygen-evolving catalyst.," *J. Am. Chem. Soc.*, vol. 131, no. 11, pp. 3838–9, Mar. 2009.

[111] M. Huynh, D. K. Bediako, and D. G. Nocera, "A functionally stable manganese oxide oxygen evolution catalyst in acid.," *J. Am. Chem. Soc.*, vol. 136, no. 16, pp. 6002–10, Apr. 2014.

[112] Y. Su, Y. Zhu, H. Jiang, J. Shen, X. Yang, W. Zou, J. Chen, and C. Li, "Cobalt nanoparticles embedded in N-doped carbon as an efficient bifunctional electrocatalyst for oxygen reduction and evolution reactions.," *Nanoscale*, vol. 6, no. 24, pp. 15080–9, Dec. 2014.

[113] J. Jung, H. Jeong, and J. Lee, "A Bifunctional Perovskite Catalyst for Oxygen Reduction and Evolution," *Angew. Chemie*, vol. 53, no. 18, pp. 4582–6, Apr. 2014.

[114] V. Petrykin, Z. Bastl, J. Franc, K. Macounova, M. Makarova, S. Mukerjee, N. Ramaswamy, I. Spirovova, and P. Krtil, "Local Structure of Nanocrystalline Ru 1− x Ni x O 2−δ Dioxide and Its Implications for Electrocatalytic Behavior—An XPS and XAS Study," *J. Phys. Chem. C*, vol. 113, no. 52, pp. 21657–21666, Dec. 2009.

[115] K. Macounova, M. Makarova, and P. Krtil, "Oxygen evolution on nanocrystalline RuO2 and Ru0.9Ni0.1O2−δ electrodes – DEMS approach to reaction mechanism determination," *Electrochem. commun.*, vol. 11, no. 10, pp. 1865–1868, Oct. 2009.

[116] M. V. Makarova, J. Jirkovský, M. Klementová, I. Jirka, K. Macounová, and P. Krtil, "The electrocatalytic behavior of Ru0.8Co0.2O2−x—the effect of particle shape and surface composition," *Electrochim. Acta*, vol. 53, no. 5, pp. 2656–2664, Jan. 2008.

[117] J. Rossmeisl, Z. W. Qu, H. Zhu, G. J. Kroes, and J. K. Nørskov, "Electrolysis of water on oxide surfaces," *J. Electroanal. Chem.*, vol. 607, pp. 83–89, 2007.

[118] M. García-Mota, A. Vojvodic, H. Metiu, I. C. Man, H.-Y. Su, J. Rossmeisl, and J. K. Nørskov, "Tailoring the Activity for Oxygen Evolution Electrocatalysis on Rutile TiO2(110) by Transition-Metal Substitution," *ChemCatChem*, vol. 3, no. 10, pp. 1607–1611, Oct. 2011.

[119] B. S. Yeo and A. T. Bell, "Enhanced activity of gold-supported cobalt oxide for the electrochemical evolution of oxygen.," *J. Am. Chem. Soc.*, vol. 133, no. 14, pp. 5587–93, Apr. 2011.

[120] Y. Gorlin, C.-J. Chung, J. D. Benck, D. Nordlund, L. Seitz, T.-C. Weng, D. Sokaras, B. M. Clemens, and T. F. Jaramillo, "Understanding interactions between manganese oxide and gold that lead to enhanced activity for electrocatalytic water oxidation.," *J. Am. Chem. Soc.*, vol. 136, no. 13, pp. 4920–6, Apr. 2014.

[121] X. Lu, Y. H. Ng, and C. Zhao, "Gold nanoparticles embedded within mesoporous cobalt oxide enhance electrochemical oxygen evolution.," *ChemSusChem*, vol. 7, no. 1, pp. 82–6, Jan. 2014.

[122] B. S. Yeo and A. T. Bell, "Enhanced activity of gold-supported cobalt oxide for the electrochemical evolution of oxygen.," *J. Am. Chem. Soc.*, vol. 133, no. 14, pp. 5587–93, Apr. 2011.

[123] H.-Y. Su, Y. Gorlin, I. C. Man, F. Calle-Vallejo, J. K. Nørskov, T. F. Jaramillo, and J. Rossmeisl, "Identifying active surface phases for metal oxide electrocatalysts: a study of manganese oxide bi-functional catalysts for oxygen reduction and water oxidation catalysis.," *Phys. Chem. Chem. Phys.*, vol. 14, no. 40, pp. 14010–22, Oct. 2012.

[124] J. Rossmeisl, a. Logadottir, and J. K. Nørskov, "Electrolysis of water on (oxidized) metal surfaces," *Chem. Phys.*, vol. 319, no. 1–3, pp. 178–184, Dec. 2005.

[125] A. J. Bard and L. R. Faulkner, *Electrochemical Methods: Fundamentals and Applications*, 2nd editio. New York: John Wiley & Sons Inc, 2001.

[126] M. Ferrandon, A. J. Kropf, D. J. Myers, K. Artyushkova, U. Kramm, P. Bogdanoff, G. Wu, C. M. Johnston, and P. Zelenay, "Multitechnique Characterization of a Polyaniline–Iron–Carbon Oxygen Reduction Catalyst," *J. Phys. Chem. C*, vol. 116, no. 30, pp. 16001–16013, Aug. 2012.

[127] U. I. Kramm, I. Abs-Wurmbach, S. Fiechter, I. Herrmann, J. Radnik, and P. Bogdanoff, "New Insight into the Nature of Catalytic Activity of Pyrolysed Iron Porphyrin Based Electro-Catalysts for the Oxygen Reduction Reaction (ORR) in Acidic Media," in *ECS Transactions*, 2009, vol. 25, no. 1, pp. 93–104.

[128] I. Herrmann, U. I. Kramm, S. Fiechter, and P. Bogdanoff, "Oxalate supported pyrolysis of CoTMPP as electrocatalysts for the oxygen reduction reaction," *Electrochim. Acta*, vol. 54, no. 18, pp. 4275–4287, Jul. 2009.

[129] J. Herranz, F. Jaouen, M. Lefèvre, U. I. Kramm, E. Proietti, J.-P. Dodelet, P. Bogdanoff, S. Fiechter, I. Abs-Wurmbach, P. Bertrand, T. M. Arruda, and S. Mukerjee, "Unveiling N-protonation and anion-binding effects on Fe/N/C-catalysts for O2 reduction in PEM fuel cells.," *J. Phys. Chem. C. Nanomater. Interfaces*, vol. 115, no. 32, pp. 16087 – 16097, Nov. 2011.

[130] J. Tian, A. Morozan, M. T. Sougrati, M. Lefèvre, R. Chenitz, J.-P. Dodelet, D. Jones, and F. Jaouen, "Optimized Synthesis of Fe/N/C Cathode Catalysts for PEM Fuel Cells: A Matter of Iron-Ligand Coordination Strength," *Angew. Chemie*, vol. 125, no. 27, pp. 7005–7008, Jul. 2013.

[131] G. Renger, "Primary processes of photosynthesis . Part 2, Principles and apparatus," in *Principles And Apparatus*, The Royal Society of Chemistry, 2008.

[132] P. E. M. Siegbahn, "Substrate water exchange for the oxygen evolving complex in PSII in the S1, S2, and S3 states.," *J. Am. Chem. Soc.*, vol. 135, no. 25, pp. 9442–9, Jun. 2013.

Paper 1

Beyond the volcano limitions in electrocatalysis – oxygen evolution reaction

Niels Bendtsen Halck, Valery Petrykin, Petr Krtil and Jan Rossmeisl.

PAPER

Beyond the volcano limitations in electrocatalysis – oxygen evolution reaction†

Niels Bendtsen Halck,[a] Valery Petrykin,[b] Petr Krtil*[b] and Jan Rossmeisl*[a]

Oxygen evolution catalysis is restricted by the interdependence of adsorption energies of the reaction intermediates and the surface reactivity. The interdependence reduces the number of degrees of freedom available for catalyst optimization. Here it is demonstrated that this limitation can be removed by active site modification. This can be achieved on ruthenia by incorporation of Ni or Co into the surface, which activates a proton donor−acceptor functionality on the conventionally inactive *bridge* surface sites. This enhances the actual measured oxygen evolution activity of the catalyst significantly compared to conventional ruthenia.

Introduction

Electrocatalytic energy conversion and storage have gained in importance recently mainly in connection with the growing role of renewable energy sources.[1] Fundamentally, the underlying electrocatalytic reactions are redox processes of multi-electron nature and can be perceived as a sequence of single electron charge transfer steps. These processes are also – as a rule – kinetically hindered and require a substantial energetic driving force to proceed at technologically acceptable rates.

Regardless of the nature of the electrocatalytic process, it has to follow through surface confined reaction intermediates. This means that the driving force can be minimized and the catalyst activity thereby optimized if the binding of the reaction intermediates is matched. The ideal catalyst is showing appreciable activity at virtually zero driving force. Such an "ideal electrocatalyst" needs to have equidistant distribution of the free energy in each individual charge transfer step of the whole reaction sequence. Rational catalyst design, therefore, can be viewed as an attempt to fine-tune the energetics of the charge transfer reactions to achieve the equal distribution of the free energy in all steps of the reaction sequence.[2] This is equivalent to optimization of the relative strength of the intermediate(s) bonding to the catalyst surface, which can be theoretically assessed using density functional theory (DFT).[3] Consequently DFT can be

used to estimate the driving forces needed in each individual charge transfer step. This represents the thermodynamic limit of the overall reaction kinetics. The catalyst design is, therefore, reduced to finding a material featuring optimal binding of all intermediates and consequently an optimal activity.

The real catalyst's design is, however, hindered by the interdependence of two or more reaction steps. The binding of the intermediates tends to show the same linear scaling with the catalyst's reactivity, which reduces the number of degrees of freedom (tuneable parameters) available for the catalyst's optimization. The reactivity which is the only tuneable parameter can therefore be used as an activity descriptor. Because only one tuneable parameter is available one can doubt the possibility to design catalysts approaching the thermodynamic limit.

This conceptual restriction, often described as the universality of the scaling relationship, has been verified for various electrocatalytic processes including oxygen evolution,[4] oxygen reduction,[5] and methanol oxidation[6] as well as for various classes of the electrocatalytic materials including metals,[7] oxides (sulfides, nitrides),[8] and molecular catalysts.[9] Therefore it seems to be an inherent limit of the rational design of electrocatalysts for the multiple electron redox processes. Breaking the scaling relationship(s) allowing for independent binding energy optimization of the reaction intermediates represents in this respect a major challenge for both theoretical and synthetic chemistry. It also represents the only way for qualitative improvement of the catalytic performance beyond the state of the art. The most intuitive approach to break the scaling relationships is to modify the active site by changing it from a surface catalyst to a three dimensional active site.[4] However, so far none of the suggestions has been successfully realized.

The oxygen evolution reaction (OER) serves as a suitable model system. It combines sufficient simplicity with practical importance as OER represents the limiting process in the

[a] *Center for Atomic-Scale Materials Design, Department of Physics, Technical University of Denmark, Building 307, 2800 Kgs. Lyngby, Denmark. E-mail: jross@fysik.dtu.dk*

[b] *Department of Electrocatalysis, J. Heyrovský Institute of Physical Chemistry, Academy of Sciences of the Czech Republic, Dolejškova 3, 18223 Prague, Czech Republic. E-mail: Petr.Krtil@jh-inst.cas.cz*

† Electronic supplementary information (ESI) available: Experimental procedure, active site model formulation, catalytic characterization and a theoretical model of the oxygen evolution reaction. See DOI: 10.1039/c4cp00571f

13682 | *Phys. Chem. Chem. Phys.,* 2014, **16**, 13682–13688

This journal is © the Owner Societies 2014

generation of hydrogen in electrochemical or photo-electrochemical water splitting.[10]

The oxygen evolution process is a four electron oxidation process driven by a transfer of 4.92 eV per oxygen molecule, *i.e.*, 1.23 eV per electron. Experiments identify the second or third electron transfer as the rate limiting step regardless of the nature of the electrode material.[11] The theoretical analysis of the problem concurs with the experimental assessment. The free energy required for the second charge transfer step is identified as an universal single descriptor of the oxygen evolution process.[4] The definition of the descriptor reflects the fact that the intermediates obtained in the first and third charge transfer step show the same scaling with the surface reactivity.

Regardless of the catalyst, the free energies of the *OH and *OOH intermediates show a constant difference of approximately 3.2 eV.[4,12] This constant difference is *ca.* 0.8 eV higher than the desired 2.46 eV of an ideal catalyst with equidistant free energy steps. This defines the smallest theoretically conceivable over-potential needed to drive the oxygen evolution to approximately 0.4 V. Although the theoretical description in principle allows for catalyst design and optimization, the 0.4 V penalty represents a limitation applicable to all the catalysts considered so far.[4,13,14] It needs to be stressed that the studies reported so far on the rational design (*i.e.* a combination of the theoretical prediction and targeted synthesis) to optimize the electrocatalytic activity in oxygen evolution remain within this paradigm and utilize combinatorial screening to optimize a single descriptor of the surface reactivity. The resulting materials – although offering a variability of the catalysts' electronic structure – cannot break the limitation put forward by the scaling relationship described above and their activities are summarized in the volcano curves.

Restricting the considerations to rutile type oxide catalysts, which represent industrial benchmark materials for OER, one may confine the actual activity to the so-called coordination unsaturated sites (*cus*) present on the surface.[15] The *cus* sites can be identified with surface metal cations which form $(n - 1)$ bonds with oxygen (where n is the number of oxygen bonds formed by the given cation in the bulk). Only *cus* sites allow for formation of reactive "*atop*" positions essential for the formation of strongly adsorbed intermediates.[15] Of the rutile oxides ruthenia (RuO$_2$) is known to be particularly active in the oxygen evolution as the theoretical analysis also confirms which places this oxide close to the top of the volcano. It was reported that even in the case of ruthenia based catalysts the activity is improved by a controlled incorporation of the heterovalent cations.[16] It may be envisaged that the *cus* site architecture may be artificially modified by the incorporation of heterovalent cations. This communication elaborates the possible effects of the local structure modifications on the resulting oxygen evolution activity and presents a general approach capable of breaking the universal scaling relationship of the OER. The general nature of this approach is demonstrated by a DFT based theoretical analysis of the OER activity of modified ruthenia catalysts combined with their experimental behaviour.

Methods

Ni and Co incorporated nanocrystalline ruthenia catalysts were prepared by co-precipitation of alcohol based solution of ruthenium(III) nitrosyl nitrate with a stoichiometric amount of Ni(NO$_3$)$_2$ or Co(NO$_3$)$_2$ by tetramethylammonium hydroxide. The precipitate was aged in a PTFE lined autoclave at 120 °C for 24 hours. The resulting precursor was filtered, dried and annealed at 400° for 3 hours to obtain crystalline catalysts. Details of the synthesis and characterization can be found in ref. 17 and 18. The reference samples of IrO$_2$ and MnO$_2$ were prepared by hydrothermal synthesis from iridium(III) acetylacetonate (Alfa Aesar) and potassium permanganate (Aldrich), respectively. The electrodes for electrochemical experiments were prepared from synthesized materials by sedimentation of nanocrystalline powder from a water based suspension (5 g L^{-1}) on Ti mesh (open area 20%, Goodfellow) to obtain the surface coverage of about 1–2 mg cm^{-2} of active oxide. The deposited layers were stabilized by annealing the electrodes for 20 min at 400 °C in air. The electrocatalytic activity of the prepared materials with respect to oxygen evolution was studied in potentiostatic experiments in a 0.1 M HClO$_4$ solution. All experiments were performed in a home-made Kel-F single compartment three-electrode cell controlled by a PAR 263A potentiostat. Pt and saturated calomel electrodes (SCE) were used as auxiliary and reference electrodes, respectively. All potentials shown in the text are recalculated and quoted with respect to RHE.

The model structures used in DFT calculations were based on the local structure as obtained by the refinement of extended X-ray absorption fine structure (EXAFS) functions processed from the X-ray absorption spectra (XAS) measured on Ru, Ni and Co K absorption edges. Details of these experiments are given in ESI.†

The DFT binding energies are calculated using a software program in which the valence electronic states are described by a plane wave basis and the core–electron interactions with Vanderbilt ultrasoft pseudopotentials.[19] For all surfaces the exchange–correlation functional Revised Perdew–Burke–Ernzerhof (RPBE) was used.[20] The planewave basis used a cutoff of 350 eV for the kinetic energy and a 500 eV cutoff for the density. A 4 × 4 × 1 Monkhorst–Pack grid was used to sample the Brillouin zone of the system. The conventional rutile ruthenia {110} surface is modelled using a 1 × 2 supercell with 4 atomic trilayers as described in the literature.[4] The Ni modified {110} surface is modelled using a larger 1 × 3 supercell with 1 Ni in the *bridge* row and 1 Ni in the *cus* row as shown in Fig. 1 together with other possible local arrangements. The calculations are spin polarized.

Results and discussion

The Ni[17] and Co[18] incorporated ruthenia conforms apparently to a single phase rutile structure featuring an uneven distribution of the structure incorporated cation. EXAFS based structural studies prove that the Ni and Co cations show a strong tendency to form clusters coordinated along the (111) direction
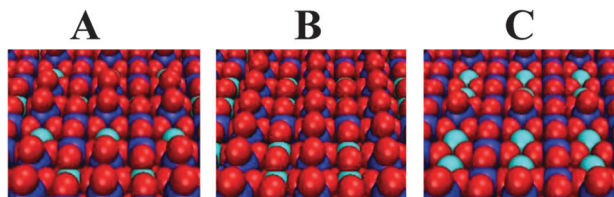
Fig. 1 Three possible schematic representations of the modified oxygen evolution active site in the Ni modified ruthenia with different placements of Ni on the rutile ruthenia {110} surface: (A) one *bridge* and one *cus* Ni, (B) two *bridge* Ni and (C) two *cus* Ni. The structures were based on EXAFS refinement.[4] Representation A was used for the DFT calculations. Color coding of the atoms: Ru – blue, Ni – green, and O – red.

of the rutile structure rather than distribute homogeneously in the ruthenium rich oxide framework. Despite the apparently intact translational order of the Ni and Co modified oxides, the cation introduction alters the local structure of the catalyst in the way shown in Fig. S1 (ESI†). Regardless of the nature of the incorporated cation, the mechanism compensating for the lower charge of the Ni and Co cations suppresses the clustering of cations along the (001) direction. Assuming a surface structure conforming to this constraint one can construct three principal arrangements shown in Fig. 1. These may feature isolated heteroatoms in either *cus* or *bridge* position (Fig. 1A) separated by cationic sites occupied by Ru atoms. Alternatively one may assume the presence of short chains of the heteroatoms (2–3) stacking along the (001) direction in either *bridge* or *cus* position forming an isolated island in the surface (Fig. 1B and C).[17]

The functionality of these principal arrangements is visualized in the DFT calculations assuming the smallest unit cell featuring all needed local arrangements (see Fig. 1A). The overall energetics of the oxygen evolution process on the Ni modified ruthenia (see Fig. 2) shows a significant deviation from that of conventional ruthenia. The potential controlling step that requires the highest driving force has changed from the third electron removal for conventional ruthenia to the second electron removal for the Ni modified ruthenia and the first electron removal for the Co modified ruthenia. The biggest free energy step amounts to 1.49 eV and 1.33 eV for the Ni and Co modified ruthenia, respectively, (see Fig. 2) as compared to 1.65 eV for conventional ruthenia. This allows us to estimate the thermodynamic limit of the overpotential of the whole process to ~0.3 V for Ni modified ruthenia and ~0.1 V for Co modified ruthenia. These overpotentials are significantly lower than the minimum overpotential of 0.4 V predicted previously[4] which is mainly due to lowering of the energy of the S_3 state compared to conventional ruthenia as shown in Fig. 3. In the experiments (see Fig. 4) cation modified ruthenia materials show a greater activity compared with conventional ruthenia.[21]
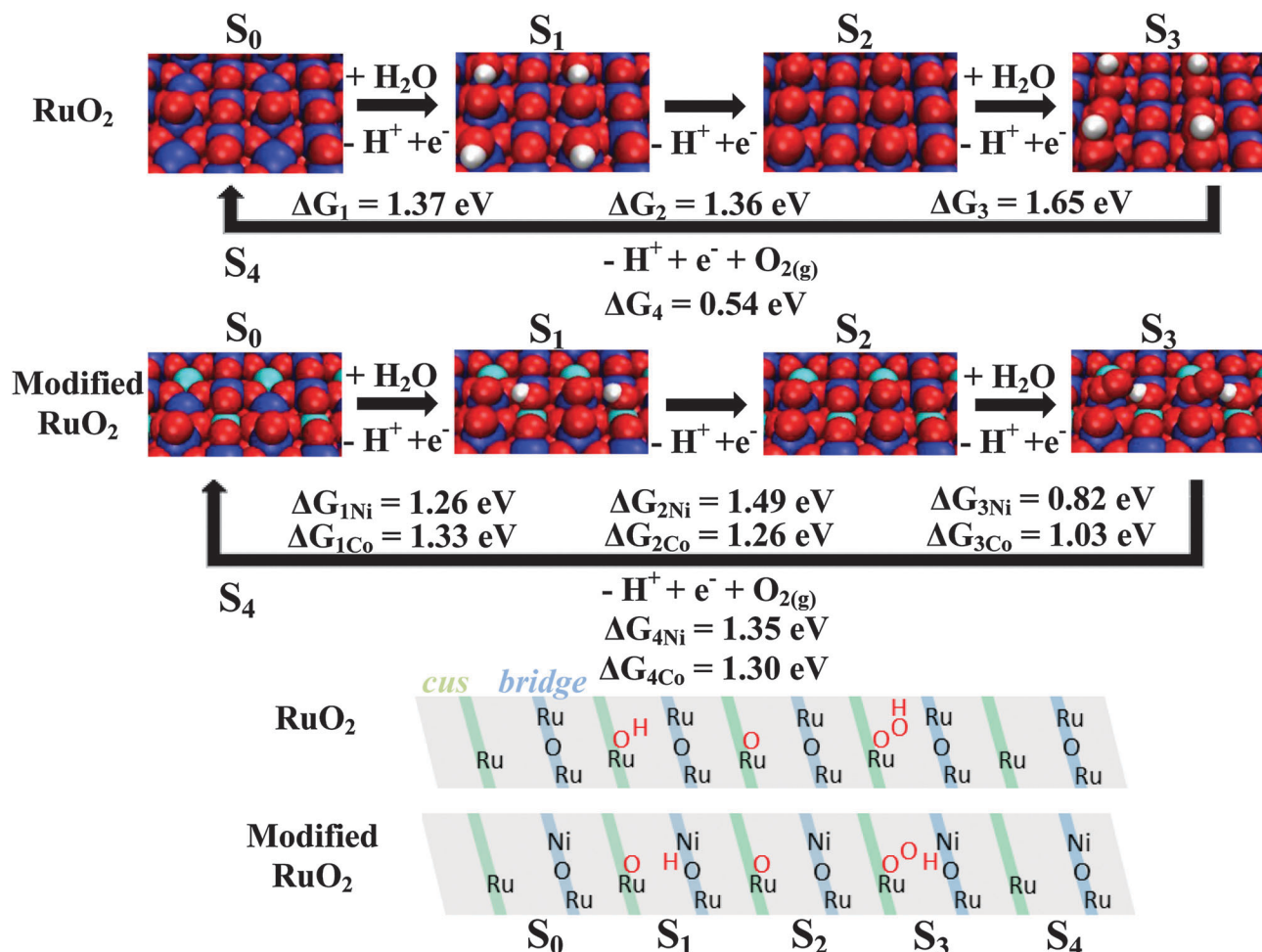
The results of the DFT modelling rationalize the effect of the introduction of Ni or Co on the ruthenia surface. The presence of Ni or Co at the *cus* positions has only negligible effect on the binding properties of the predominantly Ru composed surface. The binding energy of oxygen on the catalytically active Ru *cus* site is 2.75 and 2.59 eV for Ni and Co in the bridge site, respectively, while for conventional ruthenia the binding of O in the same position is 2.73 eV (see Table S1, ESI† and Fig. 3).

In this way the presence of Ni or Co in the *cus* site cannot be related to the observed increase in the oxygen evolution activity of Ni or Co modified ruthenia. The available *bridge* positions generally deemed non-participating in the oxygen evolution process get activated by the presence of Ni or Co, which allows for simultaneous electron–proton transfer at the potential close to the standard potential of the oxygen evolution reaction. The activation of the *bridge* site as a proton donor–acceptor effectively introduces a second tuneable parameter of the oxygen evolution process as the bridging O adsorbs hydrogen from the *OH in S_1 and *OOH species in S_3 (Fig. 2) which lowers the energies of these states compared to conventional ruthenia. The reactivity of the surface *cus* sites and the *bridge* site proton donor–acceptor potential are still weakly correlated *via* a hydrogen bond, which affects the oxidation potential of the *bridge* site if oxygen is present on the adjacent *cus* site. For Ni and Co modified ruthenia the potential for removing the proton from the bridging oxygen with oxygen present on the ruthenium *cus* site is 1.33 V and 1.49 V, respectively, and without oxygen on the *cus* site the potential for removing the proton is 1.23 and 1.33 V respectively (see Table S1 in ESI†). An improvement in the oxygen evolution related catalytic activity in hematite with Ni and Co doping has also been reported but the observed effect is rather moderate which is likely due to the semiconducting nature of hematite.[22]

The DFT calculations show that the Ni and Co modified ruthenia still do? lag behind the performance of an ideal catalyst. It is essential to stress, however, that the activation of the *bridge* sites removes the problem of the same free energy scaling of different intermediates providing the necessary degree of freedom to approach a global optimum *via* a new reaction pathway. Note that an adjustment of the donor–acceptor levels of the introduced cation is prerequisite for the oxygen evolution enhancement. Fig. 5 shows that the apex of the "volcano curve" based on the scaling relationship appears at 1.6 eV, *i.e.* at somewhat higher descriptor value than that of the ideal catalysts (1.23 eV). The theoretical activity predicted for Ni and Co modified ruthenia appears significantly above the apex of the conventional "volcano curve". These catalysts apparently being to the weak binding leg of the volcano, which depicted by the dashed line in Fig. 5, despite their descriptor belonging to the strong binding region.

This situation can be rationalized keeping in mind that the proton/acceptor functionality represents an additional descriptor not reflected in Fig. 5. Fig. 5, therefore, represents a one-dimensional reduction of a two dimensional volcano surface. In this two-dimensional approach the predicted catalytic activities would form the surface of a pyramid where the base is described by the reactivity of the surface *cus* sites and the *bridge* site proton donor–acceptor potential forming the x and y axes. In practical terms the introduction of the second parameter as seen for the oxygen evolution on Ni modified ruthenia, essentially outlines the simplest multi-dimensional approach allowing us to improve the electrocatalyst's behavior beyond the limitations of a single descriptor "volcano curve".

Although the experimental results do reflect an increase of the oxygen evolution activity upon modifying ruthenia with Ni or Co the observed effect (see Fig. 4) seems to be less significant than the theoretical predictions.

13684 | *Phys. Chem. Chem. Phys.*, 2014, **16**, 13682–13688

This journal is © the Owner Societies 2014

Fig. 2 Reaction mechanism of the oxygen evolution reaction on conventional rutile ruthenia and Ni and Co modified ruthenia on the {110} surface. The Gibbs free energies obtained from DFT calculations for each of the reaction steps are included. For Ni and Co modified ruthenia the first and third step deviate in energy due to the activating bridging O atom which binds the proton. Color coding of the atoms: O – red, Ru – blue, Ni or Co – cyan, and H – white. Below is a schematic figure of the role of the two binding sites for ruthenia and Ni modified ruthenia. The green row represents the *cus* row and the blue row represents the *bridge* row and the red color indicates intermediates.

This discrepancy can be qualified realizing the conceptual difference between real catalysts and their model representation in the DFT calculations. While the DFT calculations are created by periodic replications of the modified active site (see Fig. 1) the real catalysts feature only a limited number of the modified active sites diluted in the ruthenia matrix. A correct correlation in such a case can be obtained if one uses the measured current density per active site which is corrected for the contribution of the regions containing no dopant.

These current densities can be calculated using a simple formalism anticipating that the presence of each dopant atom in the *bridge* or *cus* site is proportional to the total dopant concentration. In this case the site normalized current for cobalt modified ruthenia can be written as:

$$J(\text{RuMe}_{\text{site}}) = \frac{J(\text{RuMe}_x) - (1 - x)J(\text{Ru})}{x} \qquad (1)$$

where x stands for the Ni or Co fraction, $J(\text{RuMe}_x)$ and $J(\text{Ru})$ represent experimentally measured current density for modified and conventional ruthenia, respectively, and $J(\text{RuMe}_{\text{site}})$ stands for the site normalized current density.

While the site normalized current densities of the Co modified catalysts calculated for different overall Co content according to eqn (1) are independent of concentration, the site normalized current densities of the Ni modified materials remain concentration dependent as shown in Fig. 6. This behavior is caused by the concentration dependence of the Ni local environment. In the particular case of modified ruthenia, the Co modification forms a cluster structure which is independent of concentration whereas the Ni modified ruthenia tend to form clusters protruding preferentially in the {110} surfaces with increasing Ni content.

This clustering tendency violates the assumption expressed in eqn (1) since the probability of Ni entering the activated *bridge* position increases above the proportionality if the total Ni content x exceeds 0.05. The deviation from the proportionality may be corrected if the structure of the cluster is taken into account. EXAFS based cluster structures applicable to Co and
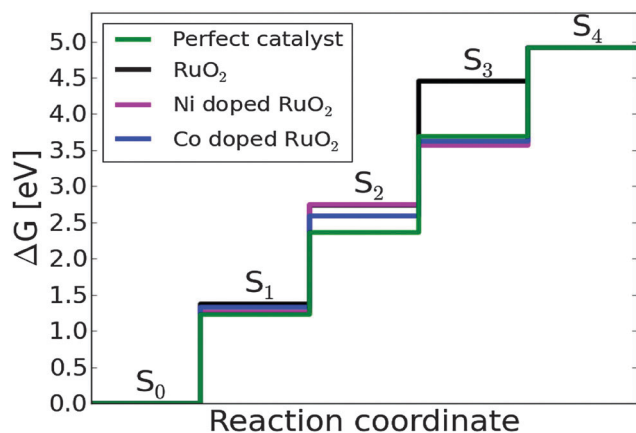
Fig. 3 Free energy diagram based on DFT calculations for conventional, Ni and Co modified ruthenia and the perfect catalyst for the four steps in the oxygen evolution reaction mechanism. The modified ruthenia catalysts have significantly stronger binding in S_3 which is the potential limiting step for ruthenia.
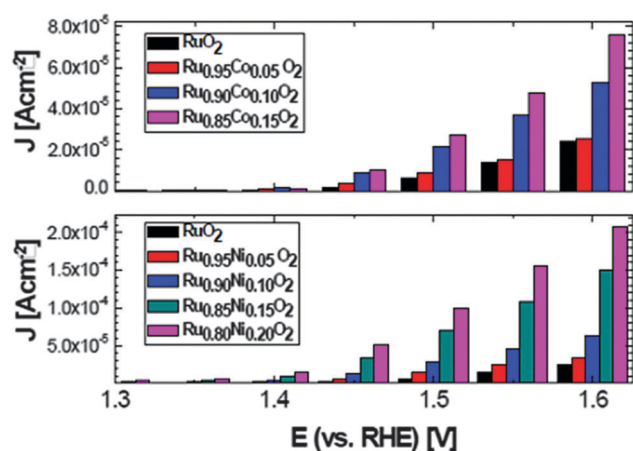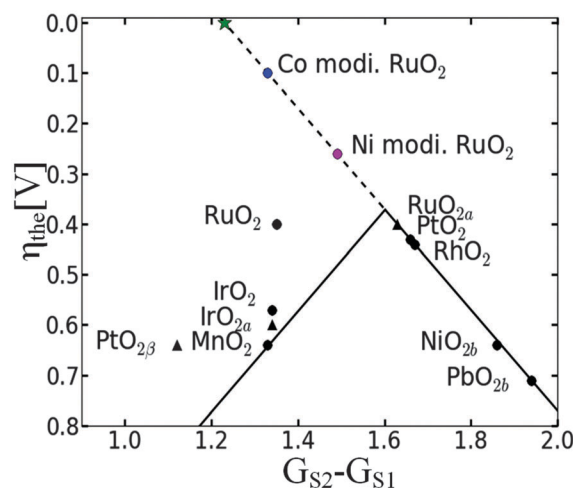

Fig. 5 Volcano curve of the theoretical overpotential for oxygen evolution processes based on the DFT calculations described in the literature[4] using the second charge transfer reaction as a descriptor. The star marks the position of an ideal catalyst, the magenta circle corresponds to Ni modified ruthenia and the blue circle to Co modified ruthenia.

Fig. 4 The current density of oxygen evolution on Ni and Co modified ruthenia in 0.1 M HClO$_4$. The data were extracted from potentiostatic experiments 40 s after potential application.
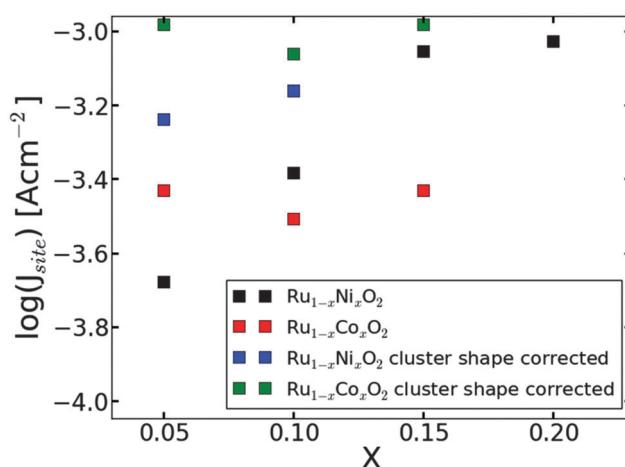
Fig. 6 Site normalized oxygen evolution activity of Ni and Co modified ruthenia Ru$_{1-x}$Ni$_x$O$_2$ as a function of the Ni and Co content with (blue and green squares) and without cluster shape correction (red and black squares). The term log denotes the base 10 logarithm.

Ni modified structures are shown in Fig. S1 of the ESI.† While the structure shown in Fig. S1a (ESI†) applies to all Co modified ruthenia, it only applies for the modified structures with low Ni content ($x = 0.05$). The structure shown in Fig. S1b (ESI†) is valid for Ni modified ruthenia with higher Ni content ($x = 0.1$). The cluster size can be conservatively estimated to be 3 and 5 Ni atoms, respectively. The orientation of the clusters with respect to the {110} surface of the nanoparticles sets a correction factor y complementing eqn (1), which reflects the fraction of the cluster atoms possibly residing in the {110} oriented surface.

$$J(\text{RuNi}_{\text{site}}) = \frac{J(\text{RuNi}_x) - (1 - x)J(\text{Ru})}{xy} \qquad (2)$$

This correction factor is equal to 1/3 and 3/5 for the structures shown in Fig. S1a and b (ESI†), respectively. The site normalized current densities reflecting the structure of the Co or Ni clusters are shown in Fig. 6 (blue and green symbols). The correction for

the size and shape suppresses the concentration dependence of Ni clusters' site normalized activity. It needs to be noted that the site normalized activity of the Co modified materials remains higher than that of the Ni counterparts, although this difference decreases with increasing concentration of the dopant. Superiority of the Co modified materials – particularly at low x – generally agrees with the results of the DFT calculations.

DFT predicted thermodynamic limits to the overpotentials are often compared with the parameters used to describe the electrode kinetics – e.g. current density at the chosen electrode potential. It has to be borne in mind that DFT does not provide overpotential values that directly can be compared to experiments. Only the trends in results should be compared. This fact can be explored to compare the theoretically limiting

13686 | Phys. Chem. Chem. Phys., 2014, 16, 13682–13688
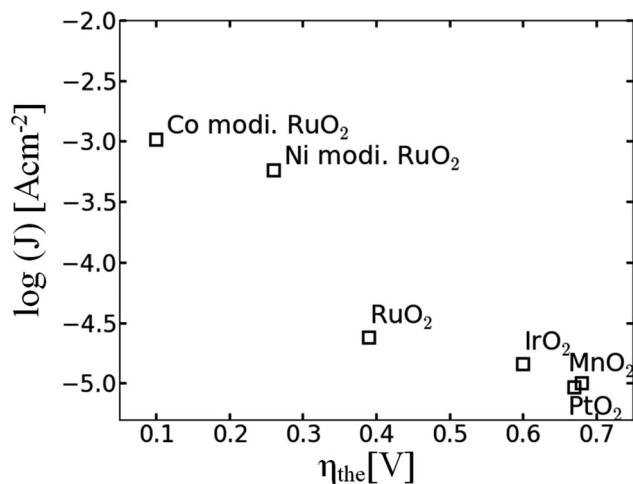
This journal is © the Owner Societies 2014

Fig. 7 The correlation between the measured current density measured at 1.6 V (vs. RHE) and the theoretical overpotential for different oxides. For the mixed oxides a concentration of Ni or Co of 0.05 is chosen to represent the activity per site for the cation modified ruthenia. More detailed information is available in the ESI.†

overpotentials with the experimental current densities taken for different catalysts at the same electrode potential. Provided that electrode reaction on all compared electrode materials follows the same reaction mechanism one should reasonably assume the experimental current density to be an exponential function of the DFT predicted limiting overpotential which is shown in Fig. 7 where the dependence of the experimental current density at 1.6 V (vs. RHE) of several known oxide electrocatalysts on the limiting activation barrier is compared. The significant increase in the site normalized oxygen evolution activity, however, also suggests rather low stability of the catalyst namely in the acid media which is indeed confirmed by the spectroscopic measurements.[17]

Regardless of the low stability of the Ni or Co modified ruthenia, these catalysts are the first examples of circumventing the limitations set by the scaling relationship. In this respect it needs to be accentuated that the observed phenomenon (introduction of proton acceptor–donor sites), although being an intrinsic catalyst property in this particular case, can in principle also be triggered by alternative mechanisms like, e.g. by anion[23,24] or CO[25,26] adsorption. This fact allows for a transfer of this approach to other electrocatalytic processes in aqueous media like, e.g. oxygen reduction[27] or CO[28] and CO₂ reduction,[29] if the electronic properties of the modified active site are fine-tuned with respect to the standard potential of the overall process. It also gives a clear indication that the rational design of the catalysts should aim at modifying the local structure of the catalytically active materials which is likely to result in metastable structures rather in stable ones which were in the center of exploration, so far.

Conclusions

Theoretical analysis of the oxygen evolution on Ni and Co modified ruthenia catalysts shows that the proton donor–acceptor functionality of the *bridge* site can be optimized independently of

the surface reactivity at the *cus* sites, which results in a significant reduction of the theoretical overpotential compared to the conventional ruthenia which is also reflected in the experimental work as Ni modified ruthenia is observed to be far more active than conventional ruthenia beyond which the scaling relationship predicts.

The addition of a proton donor–acceptor functionality to the oxygen evolution reaction represents a simple multidimensional optimization of multi-electron electrocatalytic processes in aqueous media. This principle can be likely extended to other electrocatalytic processes and may represent a general concept of the rational catalyst design.

The comparison between experimental and theoretical work on modified ruthenia is complicated by the structural differences between Ni and Co clusters formed in the ruthenia matrix which is why the per site normalization and the cluster correction are needed to be applied before the experimental results can be compared to the per site activity obtained from DFT calculations.

Acknowledgements

Notes and references

1 N. S. Lewis and D. G. Nocera, *Proc. Natl. Acad. Sci. U. S. A.*, 2006, **103**, 15729.
2 J. Rossmeisl, *et al.*, *J. Electroanal. Chem.*, 2007, **607**, 83.
3 J. K. Norskov, *et al.*, *Nat. Chem.*, 2009, **1**, 37.
4 I. C. Man, *et al.*, *ChemCatChem*, 2011, **3**, 1159.
5 I. E. L. Stephens, *et al.*, *Energy Environ. Sci.*, 2012, **5**, 6744.
6 J. Rossmeisl, *et al.*, *Energy Environ. Sci.*, 2012, **5**, 8335.
7 F. Abild-Petersen, *et al.*, *Phys. Rev. Lett.*, 2007, **99**, 016105.
8 E. Fernandez, *et al.*, *Angew. Chem., Int. Ed.*, 2008, **47**, 4683.
9 F. Calle-Vallejo, *et al.*, *Phys. Chem. Chem. Phys.*, 2011, **13**, 15639.
10 G. M. Whitesides and G. W. Crabtree, *Science*, 2007, **315**, 796.
11 S. Trasatti, *Electrochim. Acta*, 2000, **45**, 2377.
12 M. T. M. Koper, *J. Electroanal. Chem.*, 2011, **660**, 254.
13 J. Suntivich, *et al.*, *Science*, 2011, **334**, 1383.
14 M. W. Kanan and D. G. Nocera, *Science*, 2008, **321**, 1072.
15 H. A. Hansen, *et al.*, *Phys. Chem. Chem. Phys.*, 2010, **12**, 283.
16 V. Petrykin, K. Macounova, O. A. Shlyakhtin and P. Krtil, *Angew. Chem., Int. Ed.*, 2010, **49**, 4813.
17 V. Petrykin, *et al.*, *J. Phys. Chem. C*, 2009, **113**, 21657.

This journal is © the Owner Societies 2014

Phys. Chem. Chem. Phys., 2014, **16**, 13682–13688 | **13687**

18 V. Petrykin, *et al.*, *Catal. Today*, 2013, **202**, 63.

19 http://wiki.fysik.dtu.dk/dacapo.

20 B. Hammer, *et al.*, *Phys. Rev. B: Condens. Matter Mater. Phys.*, 1999, **59**, 7413.

21 J. Jirkovský, *et al.*, *Electrochem. Comm.*, 2006, **8**, 1417.

22 P. Liao, *et al.*, *J. Am. Chem. Soc.*, 2012, **134**, 13296.

23 D. Strmcnik, *et al.*, *Nat. Chem.*, 2009, **1**, 472.

24 R. Subbaraman, *et al.*, *Nat. Mater.*, 2012, **11**, 550.

25 P. Rodriguez, A. A. Koverga and M. T. M. Koper, *Angew. Chem., Int. Ed.*, 2010, **49**, 1241.

26 P. Rodriguez, Y. Kwon and M. T. M. Koper, *Nat. Chem.*, 2012, 177.

27 V. Stamenkovic, *et al.*, *Angew. Chem., Int. Ed.*, 2006, **45**, 2897.

28 A. A. Peterson and J. K. Norskov, *J. Phys. Chem. Lett.*, 2012, **3**, 251.

29 K. J. P. Schouten, *et al.*, *Chem. Sci.*, 2011, **2**, 1902.

Paper 2

Enhancing activity for the oxygen evolution reaction: The beneficial interaction of Au with Mn and Co oxides

Rasmus Frydendal, Michael Busch, <u>Niels Bendtsen Halck</u>, Elisa A. Paoli, Petr Krtil, Ib Chorkendorff and Jan Rossmeisl.

Enhancing Activity for the Oxygen Evolution Reaction: The Beneficial Interaction of Gold with Manganese and Cobalt Oxides

Rasmus Frydendal,[a] Michael Busch,[b] Niels B. Halck,[b] Elisa A. Paoli,[a] Petr Krtil,[c] Ib Chorkendorff,[a] and Jan Rossmeisl*[b]

Electrochemical production of hydrogen, facilitated in electrolyzers, holds great promise for energy storage and solar fuel production. A bottleneck in the process is the catalysis of the oxygen evolution reaction, involving the transfer of four electrons. The challenge is that the binding energies of all reaction intermediates cannot be optimized individually. However, experimental investigations have shown that drastic improvements can be realized for manganese and cobalt-based oxides if gold is added to the surface or used as substrate. We propose an explanation for these enhancements based on a hydrogen acceptor concept. This concept comprises a stabilization of an *—OOH intermediate, which effectively lowers the potential needed for breaking bonds to the surface. On this basis, we investigate the interactions between the oxides and gold by using DFT calculations. The results suggest that the oxygen evolution reaction overpotential decreases by 100–300 mV for manganese oxides and 100 mV for cobalt oxides.

Introduction

The sustainable production of hydrogen is a promising route for intermittent energy sources such as wind and solar power.[1] The electrochemical splitting of water is facilitated in electrolyzers, in which hydrogen is evolved at the cathode and oxygen at the anode. The overall efficiency of such cells is severely hindered by losses at the anode,[2,3] at which the complicated oxygen evolution reaction (OER) introduces a large overpotential. This process has been the focus of many studies, both theoretical[4–10] and experimental,[11–17] but despite the keen attention, the state-of-the-art OER catalysts still exhibit large overpotentials. In OER, four electrons and protons are removed from two water molecules. The proton and electron most difficult to remove determine the overpotential. The four reaction steps are shown in Equations (1)–(4).

$$*-OH_2 \rightarrow *-OH + H^+ + e^- \tag{1}$$

[a] R. Frydendal, E. A. Paoli, Prof. I. Chorkendorff
Center for Individual Nanoparticle Functionality
Department of Physics
Technical University of Denmark
DK-2800 Kongens Lyngby (Denmark)

[b] Dr. M. Busch, N. B. Halck, Prof. J. Rossmeisl
Center for Atomic-Scale Materials Design
Department of Physics
Technical University of Denmark
DK-2800 Kgs. Lyngby (Denmark)
E-mail: jross@fysik.dtu.dk

[c] Dr. P. Krtil
Department of Electrocatalysis
J. Heyrovský Institute of Physical Chemistry
Academy of Sciences of the Czech Republic
Dolejškova 3, 18223 Prague (Czech Republic)

$$*-OH \rightarrow *=O + H^+ + e^- \tag{2}$$

$$*=O + H_2O \rightarrow *-OOH + H^+ + e^- \tag{3}$$

$$*-OOH \rightarrow * + O_2 + H^+ + e^- \tag{4}$$

in which * represents an active surface site. This reaction pathway is valid for acidic solutions but changing to an alkaline environment does not change the thermodynamic analysis presented herein. The potential-determining step indicates the potential needed to have all steps downhill in free energy. From a thermodynamic point of view, the potential for removing protons and electrons is given by differences in free energy between reaction intermediates.[18] Therefore, minimizing the overpotential is firstly a matter of binding the reaction intermediates with the right strength to the catalyst surface, making the largest free energy difference for any oxidation step as small as possible. Unfortunately, the binding energies of the different intermediates cannot be varied independently from each other; in general binding energies of similar intermediates scale with each other.[19–21] This phenomenon has been established for reaction intermediates such as SH_x, NH_x, and OH_x on a variety of surfaces including metals, sulfides, nitrides, and oxides and is known as scaling relations. The two OER intermediates *—OH and *—OOH therefore interact in a similar way with any catalyst surface, which limits the activity of even the best performing catalysts. For the OER (proceeding via *—OH and *—OOH intermediates), a minimal overpotential of 0.3–0.4 V is needed owing to a constant difference in free energy of 3.2 eV for the $2e^-/H^+$ oxidation from *—OH to *—OOH.[9,10] The minimum overpotential can be found from the energy difference of 3.2 eV by dividing with two elementary charges and subtracting the equilibrium potential for oxygen

evolution at standard conditions of 1.23 V.[9] Thus, the two proton–electron transfers both proceed at 1.6 V, equivalent to an overpotential of 0.37 V. By changing from one catalyst to another and thereby changing the binding strength, there is little hope to break this fundamental limitation for OER. For catalyst surfaces that bind too strongly (which is the situation on Mn, Co, Ir, and Ru oxides), the overpotential originates from breaking a bond between the intermediates and the surface [Eq. (3)].

For surfaces that bind too weakly, such as NiO or TiO$_2$, the overpotential is related to bonds forming to the surface [Eqs. (1) or (2)]. This simple relationship between catalytic activity and binding of intermediates illustrates the Sabatier principle.[22] For the OER a suitable descriptor for the activity is the reaction energy of the second step [Eq. (2)], $\Delta G_{*=O} - \Delta G_{*-OH}$. Through the linear scaling relation between *–OH and *–OOH, this single descriptor can describe the potential-determining step for both strong and weak binding catalysts towards the OER.[10]

For catalyst surfaces on which reaction (3) is potential-determining, the activity could be enhanced by stabilizing the *–OOH intermediate relative to *=O and *–OH, as reaction (3) would then require a lower potential. A strategy and example on this concept have recently been demonstrated for mixtures with RuO$_2$ and either Co or Ni.[23] The idea is to introduce a hydrogen acceptor on the RuO$_2$ surface, in this case an oxygen atom, near Co or Ni so that *–OOH forms a strong hydrogen bond to this acceptor or even donates the hydrogen, forming *–OH$_{acceptor}$ and O$_2$ on the surface rather than the *–OOH intermediate. Experimentally, several studies have reported activities that oxides based on Ru–Co or Ru–Ni mixtures are more active than pure RuO$_2$.[24–26]

Decoupling the *–OOH binding energy from the *–OH binding makes it possible to tune the catalytic properties by varying the hydrogen acceptor. Reaction (3) is therefore changed into reaction (5):

$$*=O + H_2O + *=O_{acceptor} \rightarrow *-O_2 + *-OH_{acceptor} + H^+ + e^- \quad (5)$$
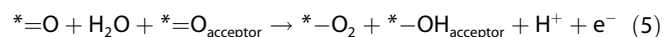
In this case the thermodynamic restrictions owing to the linear scaling relationships between *–OH and *–OOH binding no longer hold, that is, formally the OER may proceed at potentials closer to the thermodynamic limit.[23] The desirable property of the acceptor site is a suitable potential at which *=O$_{acceptor}$→*–OH$_{acceptor}$ can proceed and regenerate. For oxygen evolution, the optimal potential for this hydrogen acceptor process would be near 1.23 V.

Manganese and cobalt oxides have been studied extensively in recent years[6–8,13,27–31] as alternatives to the commonly used Ru or Ir-based catalysts.[11] Besides being abundant and benign elements, they have been proven active in the OER[32–35] and, in the case of MnO$_x$, also in the oxygen reduction reaction.[36,37] It has recently been shown that the activity of MnO$_x$ nanoparticles towards oxygen evolution can be drastically increased in the presence of Au.[38] From those results, a combination of MnO$_x$ and Au nanoparticles showed a 20-fold increase in turnover frequency at 400 mV overpotential. The enhanced activity

was also obtained by adding Au as H[AuCl$_4$] to the electrolyte. A similar effect was found earlier by El-Deab, Mohammad et al. by using Au as substrate for nano-MnOOH, reducing the overpotential by more than 200 mV compared to that found on Pt or glassy carbon substrates.[39,40]

Similarly, for CoO$_x$ it has been found that depositing 0.4 monolayers of CoO$_x$ on Au results in a higher activity than pure CoO$_x$.[41] It was even shown that Au-supported CoO$_x$ was more active than Pt, Pd, and Cu-supported CoO$_x$. From those results the authors suggested that the effect of the metal support was related to the electronegativity affecting the binding to oxygen.[41] Another interpretation could be that the metal support was directly involved in the OER mechanism, as the effect was most pronounced for submonolayer films. Furthermore, in a recent study Au nanoparticles embedded in mesoporous Co$_3$O$_4$ were found to enhance the activity towards OER.[30] In Figure 1, the experimental observations from[30,38,41] have been summarized in a Tafel plot. For MnO$_x$ nanoparticles, the decrease in overpotential due to presence of Au varied from 100 to 150 mV, whereas for CoO$_x$ the decrease varied from 20 to 100 mV.
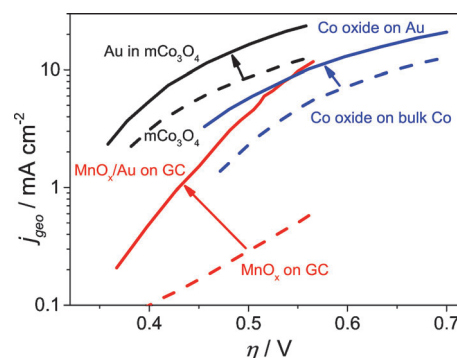


Figure 1. Experimental data summarized in a Tafel plot, showing recent reports of OER activity enhancements due to the presence of Au. For MnO$_x$/Au and MnO$_x$ the data is taken from Ref. [38]. For CoO$_x$ on Au and on bulk Co the data is from Ref. [41], and for Au in mesoporous (m-) Co$_3$O$_4$ and Co$_3$O$_4$ the data is from Ref. [30].

In this work we propose an explanation for these activity enhancements on the basis of the recently proposed hydrogen transfer from *OOH to an adjacent acceptor site.[23] By using DFT, the binding energies to the OER intermediates have been calculated on both rutile MnO$_2$ and Mn$_2$O$_3$ and the effect of Au interaction is explored. These two oxides are chosen due to their stability at OER relevant potentials.[27,42] Data for CoO$_x$ are taken from Ref. [43].

Results and discussion

First, we focus on MnO$_x$ and later extend the conceptual understanding to CoO$_x$. Water oxidation on pure Mn$_2$O$_3$ (and Co$_3$O$_4$) via *–OOH is thermodynamically limited by the formation of the *–OOH intermediate, as seen in the free energy diagram in Figure 2a. The free energy diagrams in Figure 2 are all shown at 0 V and depict the energy levels for each reaction

These are not the final page numbers! ↗↗
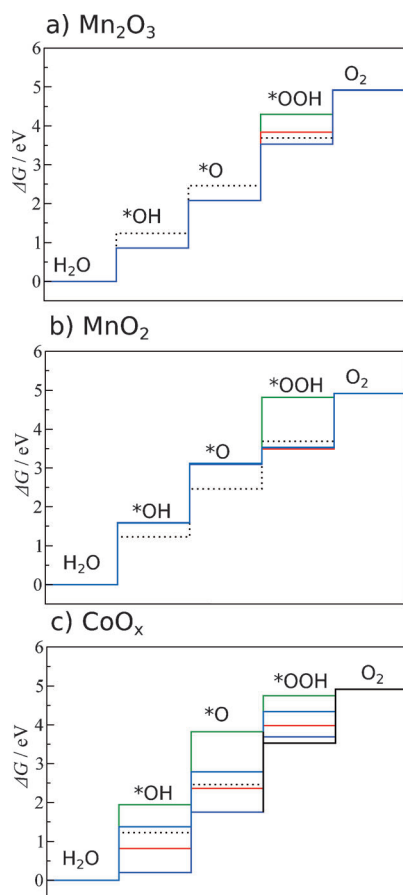
Figure 2. Free energy diagrams for the OER at zero applied potential. a) Mn_2O_3 without H transfer (——), with H transfer (——), and with H transfer to an adjacent Au=O site (——). b) Rutile MnO_2 without H transfer (——), with H transfer (——), with H transfer to an adjacent Au=O acceptor (——), and with H transfer to an Mn—O—Au site (——); blue and purple lines coincide. c) CoOOH (0 1 1 2) (——), (0 1 1 4) (——), and (0 0 0 1) (——) surfaces, Co_3O_4 (——), and Co_3O_4 with H transfer to a Au=O acceptor (——). CoOOH data are taken from Ref. [43]. •••••: Energy levels for an ideal catalyst.

step [Eqs. (1)–(4)] with and without the hydrogen transfer mechanism. The overpotential for Mn_2O_3 is estimated to be 1.0 V, rendering this oxide inert for water oxidation. The overpotential is lowered significantly with a rutile-type MnO_2 catalyst, the surface Mn atoms of which are more oxidized. This weakens the Mn=O bond so that it breaks more easily on formation of the Mn—OOH intermediate, thus, the related overpotential decreases (see Figure 2b). Even in this case the formation of Mn—OOH remains potential-determining but the critical Mn=O intermediate is significantly destabilized, lowering the potential required to form the O—O bond to 1.7 eV. This corresponds to an overpotential of 0.5 V.

In both cases a stabilization of the *—OOH would result in a decrease of overpotential. Such an effect may be obtained by a hydrogen transfer from *—OOH to an adjacent acceptor site.[23] The hydrogen transfer could occur either to a Au=O acceptor site at an adjacent nanoparticle or, assuming the possibility of incorporating Au into the surface, to a Mn—O—Au site. Notably, the *—OH binding energy for a Au nanoparticle is modelled by the binding energy to Au(111). A visualization of

these effects can be seen in Figure 3, with the hydrogen transfer to a nearby Au nanoparticle shown at the top and the incorporated Au site at the bottom. Additionally, the possibility of hydrogen transfer to a Mn=O unit needs to be considered. The latter situation may also be present in pure MnO_2.
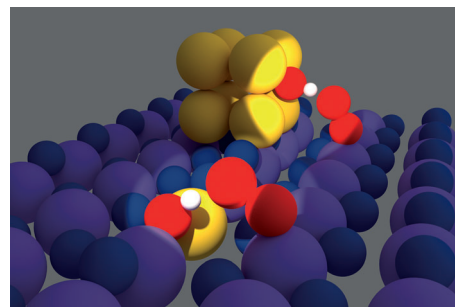

Figure 3. Model showing two different pathways for hydrogen transfer during OER on a rutile (1 1 0) MnO_2 surface. ●: Au, ●: Mn, ●: lattice O, ●: reacting O, and ○: H atoms. In the first pathway (upper highlight), the hydrogen transfer is facilitated by an adjacent Au nanoparticle. In the second pathway (lower highlight), the Mn—O—Au site functions as hydrogen acceptor, requiring Au to be incorporated into the MnO_2. A similar situation is possible for Co_3O_4 or the (0 1 1 4) facet of β-CoOOH, which both benefit from Au=O as hydrogen acceptor.

Including hydrogen transfer to an adjacent Mn=O site on MnO_2 in the reaction mechanism results in the free energy diagram shown in Figure 2b (——). There is a clear stabilization of the Mn—OOH binding, the energy of which becomes 3.5 eV. At this point, only 0.3 eV is required to facilitate O—O bond formation. Correspondingly, the oxidation of water to a hydroxide [Eq. (1)] becomes potential-determining, resulting in a decrease in the overall overpotential to only 0.4 V. Although the assumed hydrogen transfer is thermodynamically favorable, it would likely be blocked under the reaction conditions as the required adjacent Mn=O sites are involved in the OER and thus unavailable.

This is in contrast to the case with Au=O and Mn—O—Au sites, which are both inactive for water oxidation[39] but show favorable energetics as hydrogen acceptors. The cost for recovery of Au=O species, assuming an *=O coverage of 1/3 at a face-centered cubic (111) surface was reported to be 1.4 eV.[4] In fact, there is likely a variety of different sites available on Au nanoparticles that could act as hydrogen acceptors, however, treating a full Au nanoparticle is outside the scope of this investigation. Correspondingly, the binding energy of the *—OOH species decreases to 3.5 eV, rendering the initial formation of *—OH [Eq. (2)] potential-determining. Again the overpotential is lowered to 0.4 V. Incorporation of Au into the MnO_2 lattice, depicted in the lower highlight in Figure 3, can result in the formation of a Mn—O—Au site. In such a configuration the Au is located in a bridging position.[10] Assuming hydrogen transfer to a Mn—O—Au site again renders the oxidation of water to Mn—OH potential-determining by lowering the binding energy of Mn—OOH to 3.5 eV. Therefore, reaction (1) determines the theoretical overpotential, which becomes 0.4 V.

These are not the final page numbers! ↗↗

In the case of Mn_2O_3 the binding to all the intermediates are stronger, resulting in a close to ideal binding of the *O and *OH intermediates. Upon assuming hydrogen transfer to an adjacent Au=O site at a Au nanoparticle, the overpotential is lowered to only 0.2 V. Here the recovery of the hydrogen acceptor unit and the O—O bond formation step require approximately the same potentials. Further improvements are only possible with a more ideal hydrogen acceptor. This analysis is summarized in Figure 4, which includes the volcano plot showing the activity dependence based on a single descriptor, $\Delta G_{*=O} - \Delta G_{*-OH}$. This volcano arises from limitations of the scaling relations that result in an overpotential of 0.3–0.4 V at the peak, as described in the Introduction. Pure Mn_2O_3 is predicted to be less active than pure MnO_2, but with Au as hydrogen acceptor the order shifts as more ideal binding energies are available for reactions (1) and (2) on Mn_2O_3.
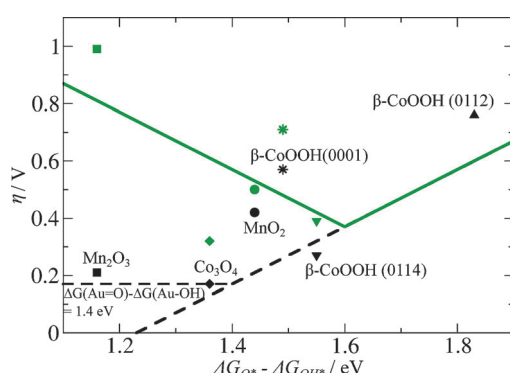
Figure 4. The theoretical volcano plot obtained for OER proceeding via *—OH and *—OOH (——) by using the difference in binding free energies between the *=O and the *—OH, established in Ref. [10] as a descriptor for the theoretical overpotential in [V]. -----: Potential of a Au=O hydrogen acceptor that is also the lower limit for overpotentials obtained from interaction with such a site. *: Theoretical overpotential without a hydrogen acceptor, *: overpotential including the hydrogen acceptor. Mn_2O_3 (■/■), MnO_2 (●/●), and Co_3O_4 (♦/♦) are placed on the strong binding branch of the volcano. For β-CoOOH only the (0 1 1 4) facet (▼/▼) is on the strong binding, for which an effect of Au interaction can be expected.

Thermodynamically it is expected that MnO_2 is the most stable phase at OER-relevant potentials, at which a Mn_2O_3 surface would be oxidized.[27,42] For Mn_2O_3, reaction (3) is potential-determining and essentially corresponds to a reduction of the active site. However, as the binding energy to *—OOH is so weak, the lowest potential path for OER on Mn_2O_3 is through an oxidation to MnO_2. In the presence of Au (hydrogen acceptors), the lowest potential would instead occur in the OER on the Mn_2O_3 site itself. This suggests that during OER the Mn_2O_3 sites near Au could exist simply because they can perform the reduction of the catalytic site. This reducing effect agrees with the indication from ex situ X-ray absorption spectroscopy that a lower oxidation state of Mn forms in the vicinity of the Au.[38] It also indicates that a very small subset of improved sites are responsible for the overall increase in current, meaning that these special sites must be very active. Unfortunately, it is difficult to assess the quantity of sites with improved catalytic ac-

tivity due to the presence of Au, which complicates estimations of the real decrease in overpotential.

Extending the concept to CoO_x, Co_3O_4 binds the intermediates similarly to MnO_2, which results in a very similar reaction profile. Due to some scatter in the binding energies, the overpotential for the reaction proceeding via Co—OOH becomes only 0.3 eV.[10] This is lowered to 0.2 V on assuming a hydrogen transfer to Au=O. Under OER conditions the most stable phase for CoO_x is β-CoOOH and the most active of the facets is (0 1 1 4).[43] Despite significant structural differences between these cobalt oxides and hydroxides, the redox potentials for the different oxidation steps are very similar, that is, an overpotential of 0.40 V is found on assuming a Co—OOH intermediate. This is lowered to 0.3 V when considering the possibility of hydrogen transfer to Au=O. Similar results are also found for the (0 0 0 1) facet. In case of (0 1 1 2) the oxidation of water to *O is potential-determining. Correspondingly, no improvements can be achieved by stabilizing the *OOH intermediate.

Similar to CoO_x and MnO_x, improvements from using a Au support have also been reported for nickel oxides.[44] For NiO and NiO_2, which lie on the weak binding side of the volcano plot, reaction (2) is potential-determining. Thus, stabilization of the Ni—OOH intermediate through a hydrogen acceptor no longer results in a lower overpotential. Instead, an improvement could originate from the same property of Au, that is, the oxidation potential at which a Au site forms Au=O. Alternatively, Au can act as an electron sea so that reaction (2) can proceed at a lower potential. This would be similar to the effect of doping in, for example, TiO_2.[45]

Conclusions

We propose that hydrogen transfer to an adjacent site significantly improves catalytic activity in the oxygen evolution reaction (OER) on Mn and Co oxides. Such an effect can explain the beneficial interactions between Au and the oxides reported experimentally. The absolute values of potentials described here may not be directly transferable to the experimental conditions, however, the trends indicate enhancements in overpotential in the order of 100 mV for MnO_2 and 300 mV for Mn_2O_3. For both Co_3O_4 and CoOOH the enhancement is approximately 100 mV. These trends are qualitatively consistent with the experimental results. As an unknown fraction of the total amount of sites is affected by the addition of Au it is complicated to compare these results directly to experimental work. It is likely that, since a small subset of sites is improved, the experimental enhancement is dampened in comparison to what the theoretical calculations suggest. Potentially, the OER sites on Mn and Co oxides close to Au approach the thermodynamic limit for OER just like the special sites that have an increased OER activity due to the Ni and Co incorporation on Ni and Co-modified RuO_2.[23] Therefore, a huge challenge remains in increasing the density of these special catalytic sites and stabilizing the surface.

4

These are not the final page numbers! ↗↗

Computational Data

All MnO_x were modeled by using periodic boundary conditions. The calculations were performed with the GPAW[46,47] DFT code (version 0.9.0.8965) at the generalized gradient approximation level of theory. DFT using the revised Perdew–Burke–Ernerhof functional[48] in combination with a finite difference grid (grid spacing: 0.15 Å) and $2\times2\times1$ k point set were employed. For the Au doped system the k point set was reduced to $2\times1\times1$ owing to a larger unit cell and a set containing only the gamma point was used for the considered molecules. The inner electrons were approximated by projector augmented wavefunctions[49] (version 0.9.9672). Spin was treated explicitly by assuming a high spin electron configuration with ferromagnetic coupling between the Mn ions. A similar procedure has been employed for a number of systems.[6,8,14] Geometries were relaxed by using the Broyden–Fletcher–Goldfarb–Shanno algorithm as implemented into ASE 3.6.0.[50] Convergence of the structure was assumed complete if the forces were below 0.05 eV Å^{-1}. Zero-point energies and entropy effects were included by adding constant corrections as described previously.[10] All adsorption energies were calculated by following the procedure described by Man et al. under standard conditions (pH 0 and $T = 283.15$ K).[10]

MnO_2 was modeled by using a 2×1 unit cell for the non-Au-doped case and a 3×1 unit cell for the Au-doped case of the (110) surface combined with a 2 monolayer (ML)-thick slab. In agreement with previous work[27] the surface was assumed to be fully oxidized, that is, all surface manganese atoms had a formal oxidation state of $+5$. The slab was terminated on the "bulk" side by *—OH species to model the bulk $+4$ oxidation state. Convergence of the slab was ensured by comparison with a 3 ML slab. No significant differences were found.

The Mn_2O_3 model was constructed by employing a slightly simplified Mn_2O_3 unit cell similar to that used by Su et al. containing $2 Mn_2O_3$ units.[27] The 2 ML slab was cut in the (110) direction and terminated such that all "bulk" manganese atoms were in a formal oxidation state of $+3$. Again, no differences with the results obtained on a 3 ML Mn_2O_3 slab were found.

All binding energies used are shown in the Supporting Information with the zero-point energy and entropy corrections. From the calculated free energies, predictions of overpotentials were made by using a previously reported method.[4,5,18] The basis of this method was to set the reference potential to that of the standard hydrogen electrode and model the electrode potential (U) by shifting the energy levels by $-eU$. The lowest theoretical overpotential was then the difference between U, with all steps downhill in energy, and the equilibrium of water oxidation, 1.23 V.

Acknowledgements

[1] J. Greeley, N. M. Markovic, *Energy Environ. Sci.* **2012**, *5*, 9246–9256.

[2] A. Marshall, B. Børresen, G. Hagen, M. Tsypkin, R. Tunold, *Energy* **2007**, *32*, 431–436.

[3] M. G. Walter, E. L. Warren, J. R. McKone, S. W. Boettcher, Q. Mi, E. A. Santori, N. S. Lewis, *Chem. Rev.* **2010**, *110*, 6446–6473.

[4] J. Rossmeisl, A. Logadottir, J. K. Nørskov, *Chem. Phys.* **2005**, *319*, 178–184.

[5] J. Rossmeisl, Z.-W. Qu, H. Zhu, G.-J. Kroes, J. K. Nørskov, *J. Electroanal. Chem.* **2007**, *607*, 83–89.

[6] M. Busch, E. Ahlberg, I. Panas, *Phys. Chem. Chem. Phys.* **2011**, *13*, 15069–15076.

[7] M. Busch, E. Ahlberg, I. Panas, *J. Phys. Chem. C* **2013**, *117*, 288–292.

[8] M. Busch, E. Ahlberg, I. Panas, *Catal. Today* **2013**, *202*, 114–119.

[9] M. T. M. Koper, *J. Electroanal. Chem.* **2011**, *660*, 254–260.

[10] I. C. Man, H.-Y. Su, F. Calle-Vallejo, H. A. Hansen, J. I. Martínez, N. G. Inoglu, J. Kitchin, T. F. Jaramillo, J. K. Nørskov, J. Rossmeisl, *ChemCatChem* **2011**, *3*, 1159–1165.

[11] S. Trasatti, *J. Electroanal. Chem.* **1980**, *111*, 125–131.

[12] R. Subbaraman, D. Tripkovic, K.-C. Chang, D. Strmcnik, A. P. Paulikas, P. Hirunsit, M. Chan, J. Greeley, V. Stamenkovic, N. M. Markovic, *Nat. Mater.* **2012**, *11*, 550–557.

[13] A. Grimaud, K. J. May, C. E. Carlton, Y.-L. Lee, M. Risch, W. T. Hong, J. Zhou, Y. Shao-Horn, *Nat. Commun.* **2013**, *4*, 2439.

[14] P. Steegstra, M. Busch, I. Panas, E. Ahlberg, *J. Phys. Chem. C* **2013**, *117*, 20975–20981.

[15] T. Reier, M. Oezaslan, P. Strasser, *ACS Catal.* **2012**, *2*, 1765–1772.

[16] H. Dau, C. Limberg, T. Reier, M. Risch, S. Roggan, P. Strasser, *ChemCatChem* **2010**, *2*, 724–761.

[17] J. Suntivich, K. J. May, H. A. Gasteiger, J. B. Goodenough, Y. Shao-horn, *Science* **2011**, *334*, 1383–1385.

[18] J. K. Nørskov, J. Rossmeisl, A. Logadottir, L. Lindqvist, J. R. Kitchin, T. Bligaard, H. Jónsson, *J. Phys. Chem. B* **2004**, *108*, 17886–17892.

[19] E. M. Fernández, P. G. Moses, A. Toftelund, H. A. Hansen, J. I. Martínez, F. Abild-Pedersen, J. Kleis, B. Hinnemann, J. Rossmeisl, T. Bligaard, J. K. Nørskov, *Angew. Chem. Int. Ed.* **2008**, *47*, 4683–4686; *Angew. Chem.* **2008**, *120*, 4761–4764.

[20] F. Abild-Pedersen, J. Greeley, F. Studt, J. Rossmeisl, T. Munter, P. Moses, E. Skúlason, T. Bligaard, J. Nørskov, *Phys. Rev. Lett.* **2007**, *99*, 016105.

[21] H. A. Hansen, I. C. Man, F. Studt, F. Abild-Pedersen, T. Bligaard, J. Rossmeisl, *Phys. Chem. Chem. Phys.* **2010**, *12*, 283–290.

[22] P. Sabatier, *Ber. Dtsch. Chem. Ges.* **1911**, *44*, 1984–2001.

[23] N. B. Halck, V. Petrykin, P. Krtil, J. Rossmeisl, *Phys. Chem. Chem. Phys.* **2014**, *16*, 13682–13688.

[24] R. Forgie, G. Bugosh, K. C. Neyerlin, Z. Liu, P. Strasser, *Electrochem. Solid-State Lett.* **2010**, *13*, B36–B39.

[25] K. Macounová, J. Jirkovský, M. V. Makarova, J. Franc, P. Krtil, *J. Solid State Electrochem.* **2009**, *13*, 959–965.

[26] K. Juodkazis, J. Juodkazytė, R. Vilkauskaitė, B. Šebeka, V. Jasulaitienė, *Chemija* **2008**, *19*, 1–6.

[27] H.-Y. Su, Y. Gorlin, I. C. Man, F. Calle-Vallejo, J. K. Nørskov, T. F. Jaramillo, J. Rossmeisl, *Phys. Chem. Chem. Phys.* **2012**, *14*, 14010–14022.

[28] M. M. Najafpour, T. Ehrenberg, M. Wiechen, P. Kurz, *Angew. Chem. Int. Ed.* **2010**, *49*, 2233–2237; *Angew. Chem.* **2010**, *122*, 2281–2285.

[29] J. Blakemore, H. Gray, J. Winkler, A. Müller, *ACS Catal.* **2013**, *3*, 2497–2500.

[30] X. Lu, Y. H. Ng, C. Zhao, *ChemSusChem* **2014**, *7*, 82–86.

[31] F. Jiao, H. Frei, *Angew. Chem. Int. Ed.* **2009**, *48*, 1841–1844; *Angew. Chem.* **2009**, *121*, 1873–1876.

[32] M. Wiechen, I. Zaharieva, H. Dau, P. Kurz, *Chem. Sci.* **2012**, *3*, 2330–2339.

[33] K. Mette, A. Bergmann, J.-P. Tessonnier, M. Hävecker, L. Yao, T. Ressler, R. Schlögl, P. Strasser, M. Behrens, *ChemCatChem* **2012**, *4*, 851–862.

[34] D. M. Robinson, Y. B. Go, M. Mui, G. Gardner, Z. Zhang, D. Mastrogiovanni, E. Garfunkel, J. Li, M. Greenblatt, G. C. Dismukes, *J. Am. Chem. Soc.* **2013**, *135*, 3494–3501.

[35] M. Huynh, D. Bediako, D. Nocera, *J. Am. Chem. Soc.* **2014**, *136*, 6002–6010.

[36] Y. Gorlin, T. F. Jaramillo, *J. Am. Chem. Soc.* **2010**, *132*, 13612–13614.

[37] Y. Gorlin, C. Chung, D. Nordlund, *ACS Catal.* **2012**, *2*, 2687–2694.

[38] Y. Gorlin, C.-J. Chung, J. D. Benck, D. Nordlund, L. Seitz, T.-C. Weng, D. Sokaras, B. M. Clemens, T. F. Jaramillo, *J. Am. Chem. Soc.* **2014**, *136*, 4920–4926.

These are not the final page numbers! ↗↗

[39] M. S. El-Deab, M. I. Awad, A. M. Mohammad, T. Ohsaka, *Electrochem. Commun.* **2007**, *9*, 2082–2087.

[40] A. M. Mohammad, M. I. Awad, M. S. El-Deab, T. Okajima, T. Ohsaka, *Electrochim. Acta* **2008**, *53*, 4351–4358.

[41] B. S. Yeo, A. T. Bell, *J. Am. Chem. Soc.* **2011**, *133*, 5587–5593.

[42] M. Pourbaix, *Atlas of Electrochemical Equilibria in Aqueous Solutions*, Pergamon Press, **1966**.

[43] M. Bajdich, M. García-Mota, A. Vojvodic, J. K. Nørskov, A. T. Bell, *J. Am. Chem. Soc.* **2013**, *135*, 13521–13530.

[44] B. S. Yeo, A. T. Bell, *J. Phys. Chem. C* **2012**, *116*, 8394–8400.

[45] M. García-Mota, A. Vojvodic, H. Metiu, I. C. Man, H.-Y. Su, J. Rossmeisl, J. K. Nørskov, *ChemCatChem* **2011**, *3*, 1607–1611.

[46] J. Mortensen, L. Hansen, K. Jacobsen, *Phys. Rev. B* **2005**, *71*, 1–11.

[47] J. Enkovaara, C. Rostgaard, J. J. Mortensen, J. Chen, M. Dułak, L. Ferrighi, J. Gavnholt, C. Glinsvad, V. Haikola, H. A. Hansen, H. H. Kristoffersen, et al., *J. Phys. Condens. Matter* **2010**, *22*, 253202.

[48] B. Hammer, L. B. Hansen, J. K. No, J. Nørskov, *Phys. Rev. B* **1999**, *59*, 7413–7421.

[49] P. E. Blöchl, *Phys. Rev. B* **1994**, *50*, 17953–17979.

[50] S. Bahn, K. Jacobsen, *Comput. Sci. Eng.* **2002**, *4*, 56–66.

These are not the final page numbers! ↗↗

FULL PAPERS

Beyond the scaling relations: Enhancing the activity of electrocatalysts for the oxygen evolution reaction is complicated owing to non-optimal binding energies of the intermediates. We present a strategy to circumvent this problem by introducing gold as a hydrogen acceptor on catalytically active surfaces. This leads to lower theoretical overpotentials for manganese and cobalt oxides.
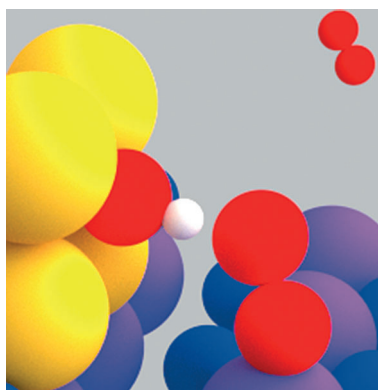
R. Frydendal, M. Busch, N. B. Halck, E. A. Paoli, P. Krtil, I. Chorkendorff, J. Rossmeisl*

■■ – ■■

Enhancing Activity for the Oxygen Evolution Reaction: The Beneficial Interaction of Gold with Manganese and Cobalt Oxides

These are not the final page numbers! ↗↗

Paper 3

Oxygen reduction on nanocrystalline ruthenia – local structure effects

Daniel F. Abbott, Sanjeev Mukerjee, Valery Petrykin, Zdeněk Bastl, Niels Bendtsen Halck, Jan Rossmeisl and Petr Krtil.

Oxygen reduction on nanocrystalline ruthenia – local structure effects†

Daniel F. Abbott,[ab] Sanjeev Mukerjee,[b] Valery Petrykin,[a] Zdeněk Bastl,[a] Niels Bendtsen Halck,[c] Jan Rossmeisl[c] and Petr Krtil*[a]

Nanocrystalline ruthenium dioxide and doped ruthenia of the composition $Ru_{1-x}M_xO_2$ (M = Co, Ni, Zn) with $0 \leq x \leq 0.2$ were prepared by the spray-freezing freeze-drying technique. The oxygen reduction activity and selectivity of the prepared materials were evaluated in alkaline media using the RRDE methodology. All ruthenium based oxides show a strong preference for a 2-electron oxygen reduction pathway at low overpotentials. The catalysts' selectivity shifts towards the 4-electron reduction pathway at high overpotentials (*i.e.* at potentials below 0.4 V *vs.* RHE). This trend is particularly noticeable on non-doped and Zn-doped catalysts; the materials containing Ni and Co produce a significant fraction of hydrogen peroxide even at high overpotentials. The suppression of the 4-electron reduction pathway on Ni and Co-doped catalysts can be accounted for by the presence of the Ni and Co cations in the *cus* binding sites as shown by the DFT-based analyses on non-doped and doped catalysts.

Introduction

The fuel cell related electrocatalytic processes based on controlled hydrogen oxidation and oxygen reduction have recently gained importance mainly in connection with the increasing utilization of renewable energy sources. Despite efforts devoted to the optimization of existing systems, the performance of real fuel cells still lags behind the expectations and the cathodic oxygen reduction is seen as the performance limiting process. The electrochemical fuel cell reactions can also be generally employed in the energy storage mode using the excess electricity or solar energy to generate energetically useful hydrogen (produced along with the oxygen), leading to the introduction of the regenerative fuel cell concept.[1,2] It also needs to be stressed that the regenerative fuel cell applications have sparked extensive catalyst development primarily for the oxygen evolution/reduction processes.

Oxygen electrochemistry, including oxygen evolution as well as reduction, represents the simplest example of multiple electron charge transfer processes which have been extensively studied both experimentally as well as theoretically.[3,4] In contrast to the development of suitable catalysts for

independent oxygen evolution (OER) or oxygen reduction (ORR), the catalysts' application in regenerative fuel cells faces significant restrictions in terms of minimizing the energetic barriers of both kinetically irreversible processes. The fact that the oxygen evolution reaction proceeds solely on oxide covered surfaces disfavors the use of metal catalysts which are reported to be of superior activity in oxygen reduction. The oxide activity in the oxygen evolution was investigated in both acidic as well as alkaline media on various systems based on oxides of ruthenium,[5–8] iridium,[5,7–9] cobalt[5,10] or manganese.[5] Oxygen reduction studies on oxides are less frequent and are generally restricted to alkaline media. Oxygen reduction has been studied on rutile,[11,12] spinel,[13,14] perovskite[15] and pyrochlore[16,17] structural types based on ruthenium, manganese, nickel, cobalt and iridium oxides. The investigated oxide catalysts were the subject of electrochemical characterization which was phenomenologically analyzed in order to explain the possible reaction pathways leading to both 4-electron and 2-electron oxygen reduction processes. In contrast to the studies of oxygen evolution, no detailed investigations aiming at the role of the catalyst structure, including the local structure of the oxygen reduction active site, have been reported so far.

The theoretical approach allowing for the generalization of oxygen electrochemistry on oxides based on DFT calculations was recently reported.[4,18,19] The DFT calculations identify the active sites for oxygen activation and the charge transfer to so-called coordination unsaturated sites (*cus*), the surface population of which is a function of the surface orientation. The *cus* surface sites feature $(n-1)$ oxygen bonding partners, where n is equal to number of metal–oxygen bonds present in the oxide bulk. It is believed that only *cus* sites can form the atop reaction

aDepartment of Electrocatalysis, J. Heyrovský Institute of Physical Chemistry, Academy of Sciences of the Czech Republic, Dolejškova 3, 18223 Prague, Czech Republic. E-mail: Petr.Krtil@jh-inst.cas.cz

bDepartment of Chemistry and Chemical Biology, Northeastern University, 360 Huntington Ave., Boston, MA 02115, USA

cCenter for Atomic-Scale Materials Design, Department of Physics, Technical University of Denmark, Building 307, 2800 Kgs. Lyngby, Denmark

† Electronic supplementary information (ESI) available. See DOI: 10.1039/c4ra10001h

intermediate(s), which are essential in the oxygen electrochemistry. In this respect one can easily predict that the catalytic activity and selectivity of oxide catalysts may be altered if one controls the population and stacking of the *cus* sites at the oxide surface. This trend has been shown for oxygen evolution on heterostatically doped ruthenia when the incorporation of lower valency cations, such as Ni,[20–23] Co,[24–27] Fe[28] or Zn[29,30] into ruthenia framework resulted in changes to both the activity and selectivity of anodic processes including oxygen and chlorine evolution. Similar systematic studies focused on other oxide systems are, so far, lacking.

This paper focuses on the role of the local structure of the oxide catalysts in the oxygen reduction reaction. We report on the ORR activity of model nanocrystalline ruthenia based catalysts with local structure controlled by doping with Ni, Co and Zn. The observed electrocatalytic activity and selectivity are related to the actual local structures and rationalized using DFT-based thermodynamic analysis of the oxygen reduction process.

Methods

Material preparation

Ruthenium dioxide and doped samples of the composition $Ru_{1-x}M_xO_2$ (M = Co, Ni, Zn) were synthesized using the spray-freezing freeze-drying method as described in ref. 30 and 31. Generally, an 8 mM solution was prepared by dissolving the appropriate amount of $Ru(NO)(NO_3)_3$ (31.3% Ru, Alfa Aesar) in 100 mL of Millipore H_2O. In the case of doped materials, a stoichiometric amount of the appropriate transition metal salt was added to the solution. Zinc-doped samples were prepared from the acetate precursor, $Zn(C_2H_3O_2)_2 \cdot 2H_2O$ (99.5% ACS reagent grade, Fluka). Cobalt- and nickel-doped samples were prepared from the nitrate salts, $Co(NO_3)_2 \cdot 6H_2O$ and $Ni(NO_3)_2 \cdot 6H_2O$ (99.999% trace metal basis, Sigma Aldrich), respectively. The starting solution was then sprayed into liquid N_2. The resulting ice slurry was collected in an aluminum tray pre-cooled with liquid N_2 and quickly transferred to a freeze-dryer (FreeZone Triad Freeze Dry System 7400030, Labconco) pre-cooled to -30 °C. The frozen solvent was sublimated at reduced pressure (≈ 1.0 Pa) while the temperature was ramped according to the following program: -30 °C (1 h), -25 °C (5 h), -20 °C (4 h), -15 °C (6 h), 30 °C (4 h). After drying, the resulting powder was annealed in air at 400 °C for 1 hour.

XRD, XPS and SEM characterization

The crystallinity of sample powders was characterized using a Rigaku Miniflex 600 powder X-ray diffractometer with $Cu_{K\alpha}$ radiation operating at 40 kV and 15 mA. The average sample compositions were evaluated with X-ray energy dispersive spectroscopy using a Hitachi S4800 scanning electron microscope (SEM) equipped with a Nanotrace EDX detector (Thermo Electron). Sample compositions did not deviate significantly from the projected ones. Particle size was evaluated by analyzing SEM images and averaging the size of 300 randomly chosen particles. The X-ray photoelectron spectra (XPS) of the

prepared materials were measured using a modified ESCA 3 MkII multitechnique spectrometer equipped with a hemispherical electron analyzer operating in the fixed transmission mode. Al Kα radiation was used for electron excitation. The binding energy scale was calibrated using the Au $4f_{7/2}$ (84.0 eV) and Cu $2p_{3/2}$ (932.6 eV) photoemission lines. The spectra were collected at a detection angle of 45° with respect to the macroscopic surface normal. The studied materials were characterized using survey scan spectra and high resolution spectra of overlapping Ru 3d + C 1s photoelectrons, Ru 4s, Zn 2s and O 1s photoelectrons. The spectra were curve fitted after subtraction of Shirley background using the Gaussian–Lorentzian line shape and nonlinear least-squares algorithms. Quantification of the elemental concentrations was accomplished by correcting the photoelectron peak intensities for their cross sections and for the analyzer transmission function. The typical error of quantitative analysis by XPS is $\sim$10%.

Electrochemical measurements

The electrochemical oxygen reduction activity of the prepared materials was assessed in a three-electrode single-compartment cell with a rotating ring-disk electrode (RRDE) setup (Pine Instruments, USA). The potential was controlled using an Autolab PGSTAT30 (EcoChemie, The Netherlands). Catalyst ink suspensions were prepared by sonicating 9.8 mg RuO_2 or $Ru_{1-x}M_xO_2$ (M = Co, Ni, Zn) with 5.00 mL Millipore water, 4.95 mL isopropyl alcohol, and 50 μL of 5 wt% Nafion® ionomer solution until the suspension was well dispersed. A 10.0 μL aliquot of the ink was drop cast on a 0.196 cm^2 glassy carbon disk electrode equipped with a platinum ring to yield a total catalyst loading of approximately 50 μg cm^{-2}. All experiments were conducted at room temperature in 0.1 M NaOH prepared from sodium hydroxide pellets (semiconductor grade, 99.99%, Sigma-Aldrich). A platinum wire served as the counter electrode and a saturated calomel electrode (SCE) served as the reference electrode. All potentials reported are quoted against RHE. Electrolyte solutions were saturated with O_2 for 30 minutes prior to oxygen reduction measurements. The measured oxygen reduction currents were corrected for the contribution of the capacitive current by subtracting the cyclic voltammograms obtained under identical conditions in Ar saturated solution. Cyclic voltammograms were recorded at a scan rate of 20 mV s^{-1} and the potential of the platinum ring electrode was held at 1.1 V *vs.* RHE during all measurements. The ring collection efficiency was determined to be 0.275 according to the procedure described in ref. 32.

DFT analysis of oxygen reduction

The thermodynamic analysis of the ORR on ruthenia based [110] surfaces was addressed using GPAW (grid-based projector-augmented wave) a DFT based code[33] together with the ASE (atomic simulation environment).[34] For all surfaces the exchange correlation functional, revised Perdew Burke Ernzerhof,[35] was used. The grid spacing selected was 0.18 and the Brillouin zone was sampled using a 4 × 4 × 1 Monkhorst–Pack grid. The two model systems, the non-doped and Ni-doped

ruthenia [110], were approximated using a 2×1 and a 3×1 supercell, respectively, with four atomic trilayers and with the bottom two trilayers fixed. The remaining layers and adsorbates were relaxed until the residual forces in all directions were less than 0.05 eV $Å^{-1}$. The positions of the Ni atoms were modeled using the approach described in ref. 33. The calculations containing Ni were spin-polarized.

Results and discussion

XRD and SEM characterization

X-ray diffraction patterns of all studied materials are shown in Fig. 1. In all cases the recorded patterns conform to a single phase tetragonal structure of the rutile type identical with that of RuO_2 (PDF file #431027). The average size of coherent crystallite domains was evaluated using the Scherrer formula:

$$D_i = \frac{\lambda}{\beta_i \cos \theta_i} \tag{1}$$

where D_i is the size of the crystallite domain, λ is the wavelength of the incident radiation ($Cu_{K\alpha} = 1.540598$ Å), β_i is the width of the diffraction peak at half maximum intensity measured in radians, and θ_i is the angle of the hkl reflection.

The average coherent domain size ranged between 4.3 and 5.7 nm (see Table 1). Representative SEM images of the doped ruthenia are summarized in Fig. 2. The particle sizes evaluated from SEM micrographs agree with the coherent domain size values (see Table 1). Average sample compositions did not deviate significantly from the projected ones and are listed in Table 1.
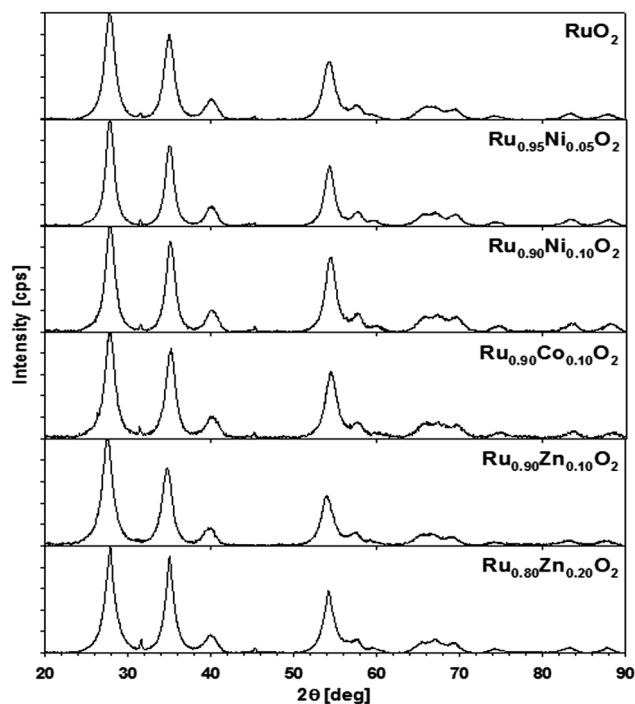

Fig. 1 Powder X-ray diffraction patterns for nanocrystalline RuO_2 and $Ru_{1-x}M_xO_2$ (M = Ni, Co, Zn) after annealing in air for 1 hour at 400 °C.

Surface composition of all doped samples reflects the metastable character of the materials and previous thermal treatment which result in a dopant enrichment of the surface layer.[21,37] This effect is most pronounced in the case of the Zn doped materials when the actual surface compositions of both studied materials correspond to $Ru_{0.73}Zn_{0.27}O_{2.43}$ and to $Ru_{0.63}Zn_{0.37}O_{2.23}$ for the materials with nominal Zn contents of 0.1 and 0.2, respectively. It needs to be noted that the apparent excess of the oxygen in the surface composition can attributed to surface OH groups as well as to adsorbed water.

Electrochemical measurements

All prepared ruthenia materials are active ORR catalysts in alkaline media. The ORR polarization curves for RuO_2 and $Ru_{1-x}M_xO_2$ (M = Ni, Co, Zn) samples are shown in Fig. 3. The disk current (i_D) which reflects the oxygen reduction shows a pronounced peak at approximately 0.40 V to 0.55 V before approaching a mass transport controlled region. The disk current feature can be tentatively associated with a change in the Ru oxidation state from Ru(IV) to Ru(III).[11,36] This process is usually connected with cation insertion into the oxide structure to balance the charge in cationic and anionic sub-lattices.[37] The behavior giving rise to the peak in the disk current is also manifested in the ring current, indicating a pronounced formation of hydrogen peroxide in this potential region. The hydrogen peroxide formation in the 0.40 V to 0.55 V interval seems to be unaffected by the chemical composition of the catalyst. The formation of hydrogen peroxide seems to be suppressed with increasing rotation rate. The precise mechanism of this reduction process is, however, not evident.

The overall ORR activity of the doped ruthenia catalysts is lower than that of the non-doped ruthenia. The ORR activity as reflected in the disk currents (i_D) generally decreases for the Co- and Ni-doped samples. There is no apparent effect of the actual dopant concentration on the oxygen reduction disc currents. The corresponding ring currents (i_R) are, however, higher than that of the non-doped ruthenia, particularly at high overpotentials (*i.e.* at potentials negative to 0.4 V *vs.* RHE). This shows a pronounced tendency of Co and Ni-doped materials to produce H_2O_2 namely at high overpotentials (n ranging between 3.0 and 3.4). In contrast, the Zn-doped materials show a preference for the 4-electron reduction pathway with n values ranging between approximately 3.6 and 3.8 while the activity remains comparable to that of the non-doped ruthenia. Also the selectivity of the doped ruthenia in oxygen reduction is controlled rather by the doping process itself than by the actual dopant content.

The observed behavior reflects the surface sensitivity of oxygen reduction on oxide surfaces, which can be related to the surface local structure. Quantitative visualization of this behavior is shown in Fig. 4, which plots the potential dependence of the average number of electrons transferred to an oxygen molecule on different doped ruthenium dioxide materials as calculated from the Koutecky–Levich equation:[38]

Table 1 Results of the analysis of the powder diffraction data for RuO_2 and doped RuO_2 samples

Actual composition	Coherent domain size [nm]	Strain [%]	a [Å]	c [Å]	Particle size [nm]
RuO_2	5.7	0.46	4.470	3.120	7.6 ± 2.2
$Ru_{0.9}Zn_{0.1}O_{2-z}$	4.9	0.61	4.526	3.108	8.9 ± 2.2
$Ru_{0.82}Zn_{0.18}O_{2-z}$	5.5	0.00	4.519	3.099	5.8 ± 1.5
$Ru_{0.95}Ni_{0.05}O_{2-z}$	5.3	0.00	4.515	3.096	7.2 ± 1.4
$Ru_{0.91}Ni_{0.09}O_{2-z}$	5.0	0.00	4.501	3.079	7.9 ± 2.3
$Ru_{0.9}Co_{0.10}O_{2-z}$	4.3	0.21	4.505	3.081	7.4 ± 1.8

$$\frac{1}{i} = \frac{1}{i_k} - \frac{1}{0.62nFAD_{O_2}^{\frac{2}{3}}\nu^{-\frac{1}{6}}C_{O_2}^{*}\omega^{\frac{1}{2}}} \qquad (2)$$

where F is Faraday's constant, A is the geometric area of the electrode, D is the diffusion coefficient (1.90×10^{-5} cm^2 s^{-1}), ν is the kinematic viscosity (8.70×10^{-3} cm^2 s^{-1}), and C is the bulk concentration of O_2 (1.22×10^{-6} mol cm^{-3}).[39]

It has to be stressed that in contrast to the behavior known for metal electrocatalysts in acid media, the oxygen reduction on ruthenia based catalysts apparently forms primarily hydrogen peroxide, namely at low overpotentials. The observed selectivity of ruthenia-based catalysts in ORR shows a complex potential dependence which can be treated either by a phenomenological or a local structure sensitive approach.

Assuming a general phenomenological model of the oxygen reduction mechanism as proposed previously (see Fig. 5),[40,41] oxygen can be reduced to water (4-electron pathway) either directly or sequentially with H_2O_2 as the main adsorbed intermediate.

In principle, H_2O_2 either desorbs and can be detected on the ring or can be further reduced to water in the second 2-electron reduction process. The measured disk current summarizes the current contributions from the complete 4-electron reduction to H_2O and the 2-electron reduction to H_2O_2 while the recorded ring current is proportional only to the amount of oxygen reduced to H_2O_2. In this respect a ratio of i_D/i_R can be used as an indicator of the actual mechanism which should yield a straight line proportional to k_1/k_2 when plotted against $\omega^{-1/2}$ (see Fig. 6).[40]

The actual i_D/i_R data deviate from linearity (see Fig. 6) as can be expected since the formalism incorporated in the scheme depicted in Fig. 5 disregards the nature of the individual reaction steps composing both 2- and 4-electron reduction pathways and their different dependence on the electrode potential.

The individual rate constants k_1, k_2 and k_3 were evaluated from ORR data assuming that all three processes proceed simultaneously and that the values of k_{-1}, k_{-2}, and k_{-3}, corresponding to reversed reactions, are negligible. The adsorption of oxygen on the electrode surface is also assumed to proceed sufficiently fast. The potential dependence of the rate constants for all considered catalysts in the overall oxygen reduction mechanism is shown in Fig. 7.
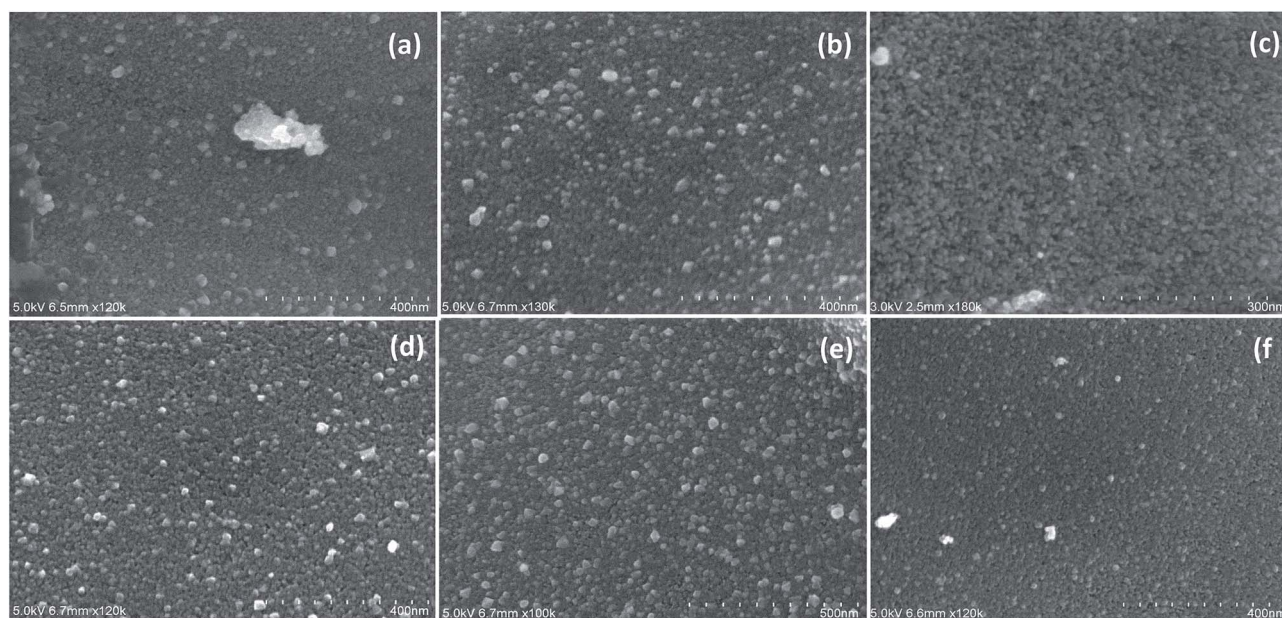
Fig. 2 SEM images of nanocrystalline (a) RuO_2, (b) $Ru_{0.90}Zn_{0.10}O_2$, (c) $Ru_{0.80}Zn_{0.20}O_2$, (d) $Ru_{0.95}Ni_{0.05}O_2$, (e) $Ru_{0.90}Ni_{0.10}O_2$, and (f) $Ru_{0.90}Co_{0.10}O_2$ after annealing at 400 °C in air for 1 hour.
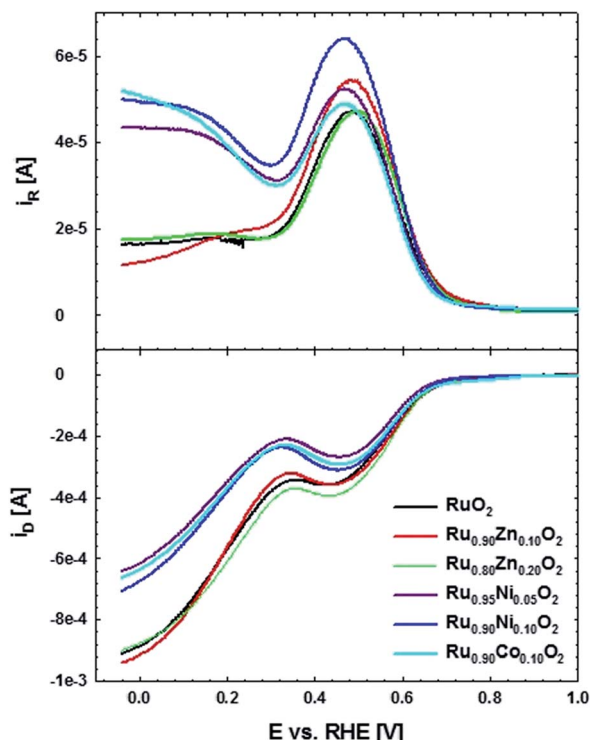
Fig. 3 ORR polarization curves and ring currents at 1600 rpm for RuO_2 and $Ru_{1-x}M_xO_2$ (M = Ni, Co, Zn) electrodes at 20 mV s^{-1} in O_2 saturated 0.1 M NaOH. E_{ring} = 1.1 V vs. RHE.

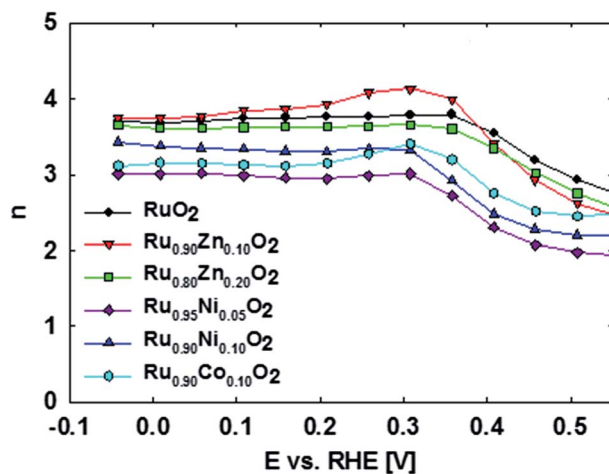
Fig. 4 Potential dependence of the average number of electrons transferred during oxygen reduction on RuO_2 and $Ru_{1-x}M_xO_2$ (M = Ni, Co, Zn) electrodes. Presented data were calculated using Koutecky–Levich equation.

It seems that the conversion of H_2O_2 to H_2O through the series pathway (k_3) is negligible on all electrode surfaces at high overpotentials. It has to be noted, that although the k_3 values are negligible with respect to k_1 and k_2 there is a significant difference between k_3 of the Zn-doped and non-doped samples and those obtained for the Ni- and Co-doped samples. The values of k_3 observed for Ni- and Co-doped samples are

approximately one order of magnitude lower and seem to correspond to decreased tendency of these materials to reduce oxygen through the 4-electron pathway.

As follows from Fig. 7, the conversion of O_2 to H_2O_2 appears to be the dominant process on ruthenium based oxides at low overpotentials. In this respect the reduction behavior of the ruthenia differs significantly from that of metals which prefer the 4-electron reduction at low overpotentials. The role of the chemical composition in selectivity of doped catalysts towards 2- and 4-electron reduction pathways can be visualized by the potential at which the catalytic system shows the same preference for the 4-electron and 2-electron reaction pathways, i.e. potential at which $k_1/k_2 = 1$ (see Fig. 8).

A fundamental description of the oxygen reduction on oxide surfaces can be based on the thermodynamic analysis of the observed trend, which highlights the enhanced tendency of the Ni- and Co-doped materials to form hydrogen peroxide and reflects the local structure of the doped ruthenium oxides.

DFT analysis of oxygen reduction

A fundamental description of the oxygen reduction on oxide surfaces can be based on the thermodynamic analysis of the process utilizing the DFT modeling. Reverting to the formalism used for the oxygen evolution reaction we can describe the overall reduction process as a sequence of four consecutive concerted electron/proton transfers – if one aims for the complete 4-electron reduction – or of two consecutive electron/proton transfers if hydrogen peroxide is considered as the reaction product. The results of the DFT investigations of ORR reduction on ruthenium dioxide based catalysts are summarized in Fig. 9–12.

A systematic description of the stable surface structures at different potentials represents a prerequisite step in the theoretical investigation of oxygen reduction on an oxide surface, which in this case is the [110] rutile surface of ruthenia. This procedure results in computational Pourbaix diagrams where the stable surface at any given potential features the highest stabilization (i.e. the most negative surface energy) of the system (see ESI† for details of the Pourbaix diagram construction).

Bearing in mind that the [110] oriented surface of a rutile type oxide features the transition metal cations in two local environments, cus and bridge, one can visualize the surface of non-doped ruthenium dioxide as changing from the surface structure characterized by protonated oxygen on cus sites and deprotonated oxygens in bridge sites (region C in Fig. 9) to the surface featuring vacant cus and protonated oxygens in bridge sites (region A in Fig. 9). Since the ORR was not observed at potentials positive to 0.7 V (vs. RHE) one can restrict the DFT investigations of the oxygen reduction on conventional RuO_2 to the surface stable in the region A. In the case of doped ruthenia (as shown in the case of the Ni doped material presented in Fig. 10) one needs to consider the complexity arising from the chemical composition when both types of transition metal cations enter the cus and bridge positions. This variability in the chemical composition also increases the number of distinctive
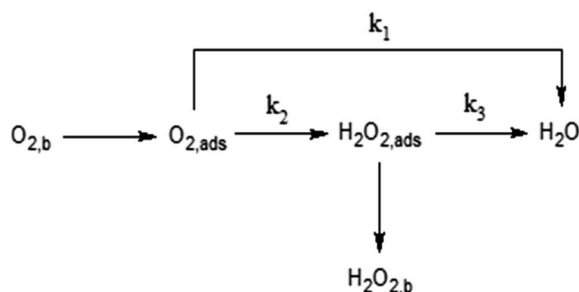
Fig. 5 Phenomenological mechanism of oxygen reduction according to ref. 40.

Fig. 7 Potential dependence of the rate constants for the reduction of O_2 to H_2O (k_1), of O_2 to H_2O_2 (k_2), and H_2O_2 to O_2 (k_3) on nanocrystalline ruthenia based catalysts. The presented data correspond to experiments carried out in O_2 saturated 0.1 M NaOH at 1600 rpm.

oxygen atoms available at the surface, the binding energy of which depends on their nearest neighbors. Although the electrode potential dependent variability of the surface structure is more pronounced in this case, the stable structure predicted for the potential range in which the ORR proceeds is qualitatively the same and corresponds to vacant *cus* sites complemented by protonated oxygen atoms connecting the *bridge* sites (see structure D in Fig. 10).

The DFT models predict that the entire process begins with oxygen adsorption at coordination unsaturated (*cus*) cationic sites. The behavior of both the non-doped and the doped ruthenia catalysts is controlled by the local structure and depends on the nature of the cation residing in the *cus* site as well as on the electrode potential. In the case that the *cus* site is occupied by a ruthenium cation (which are present on all investigated catalysts) the first electron reduction forms a rather strongly bound *OOH intermediate, which is more stable than the hydrogen peroxide at most reasonable electrode potentials (see Fig. 11). Consequently, the further reduction of the *OOH intermediate located on Ru *cus* site cannot form hydrogen peroxide unless one uses an rather strong external electric field to weaken the *OOH binding to the surface. The actual potential(s) at which hydrogen peroxide formation becomes thermodynamically allowed are indicated in the legend of the Fig. 11.

In the case that the *cus* site is occupied by an heteroatom, *e.g.* Ni or Co, (see Fig. 11) one observes a significantly weaker
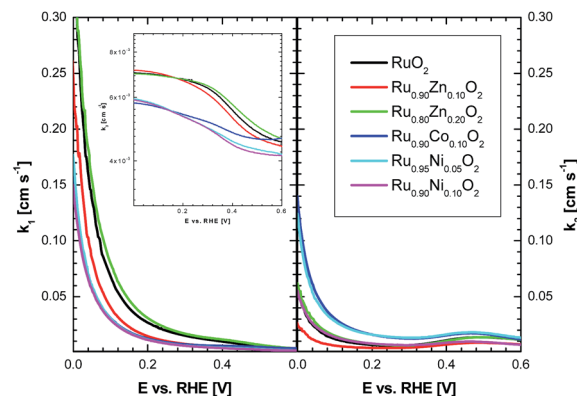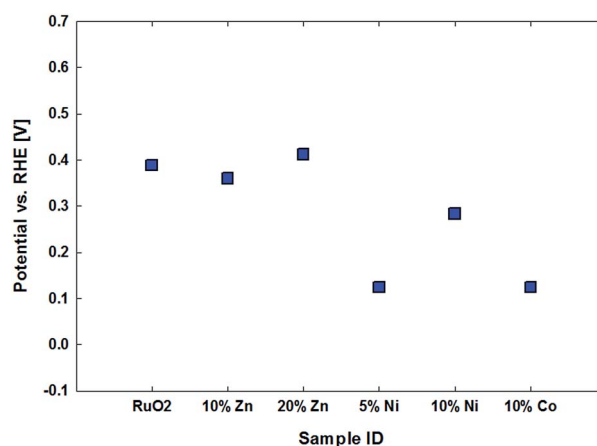

Fig. 8 The potential of equal rate in 2- and 4-electron reduction for different ruthenia based catalysts.

binding of the *OOH and *O compared with the Ru occupied *cus* sites. This fact decreases the potential at which the reduction on Ni_{cus} starts to contribute to the overall reduction
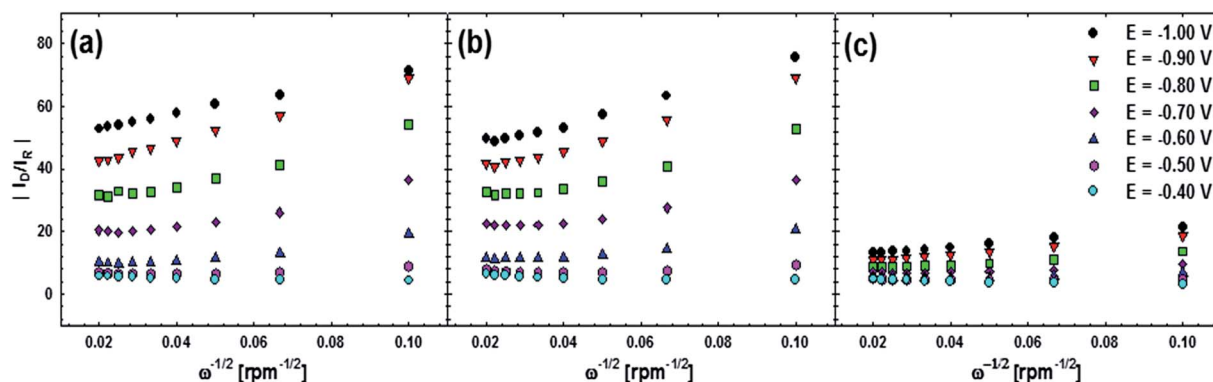

Fig. 6 $|I_D/I_R|$ vs. $\omega^{-1/2}$ plots for (a) RuO_2, (b) $Ru_{0.80}Zn_{0.20}O_2$, and (c) $Ru_{0.90}Ni_{0.10}O_2$ presented data were extracted from RRDE experiments carried out in O_2 saturated 0.1 M NaOH.
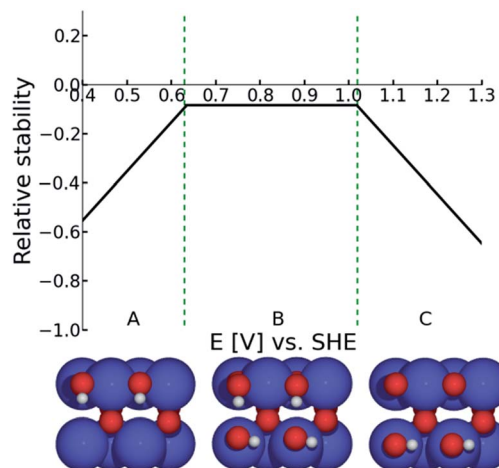
Fig. 9 Surface Pourbaix diagram for RuO₂. Detailed description of the diagram construction is given in the ESI.†
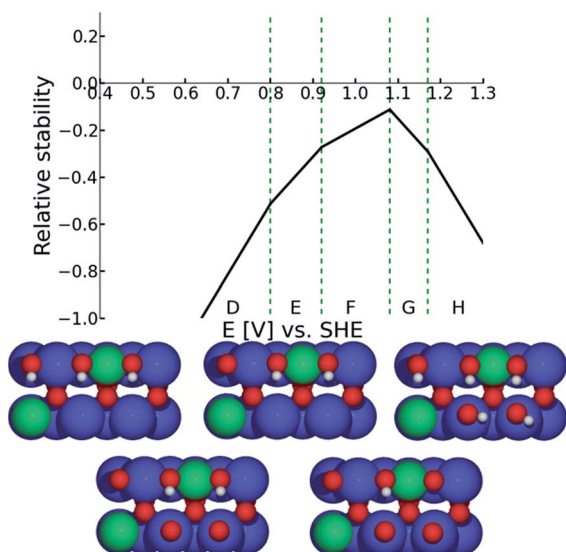

Fig. 12 Volcano plot for the 2-electron (blue) and 4-electron (red) reduction of O₂ to H₂O₂ and H₂O, respectively, using the binding energy of OOH as a descriptor. The dotted lines represent the equilibrium potentials for the reduction products. In the case of the Ni-doped ruthenia the limiting over-potential for both possible reaction sites (Ru$_{cus}$ and Ni$_{cus}$) are shown along with that of conventional ruthenia.

Fig. 10 Surface Pourbaix diagram for Ni-doped RuO₂. Detailed description of the diagram/s construction is given in the ESI.†

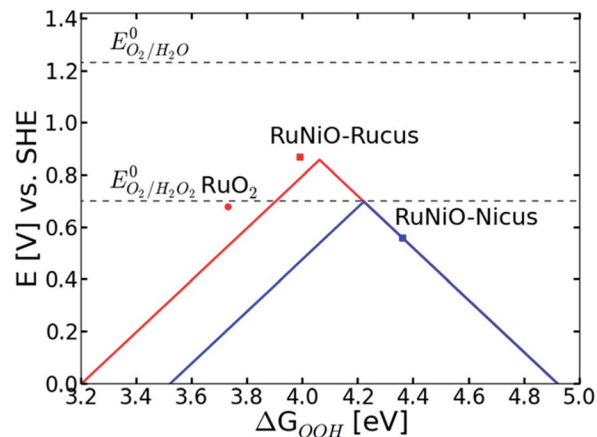process. The weak interaction of the *OOH with the heteroatom-containing cus site restricts the presence of such an adsorbate in the potential region with low total surface coverage, i.e. to relatively high over-potentials. It needs to be noted though, that the formation of hydrogen peroxide from *OOH confined on a heteroatom occurs at much more positive potentials than in the case of *OOH confined to Ru-containing cus sites and further reduction of the *OOH intermediate can proceed via the 4-electron or 2-electron reduction pathway with approximately the same probability.

Fig. 12 shows the dependence of the electrode potential needed to drive the oxygen reduction on oxide based surfaces either via the 4-electron (red) or 2-electron (blue) reaction pathway as a function of the reaction descriptor – i.e. adsorption energy of the *OOH intermediate. It needs to be noted that in a similar manner one may describe the reaction with the adsorption of *OH due to the interdependence of the adsorption energies of the intermediate formed in the first and third charge transfer step.[3,33]
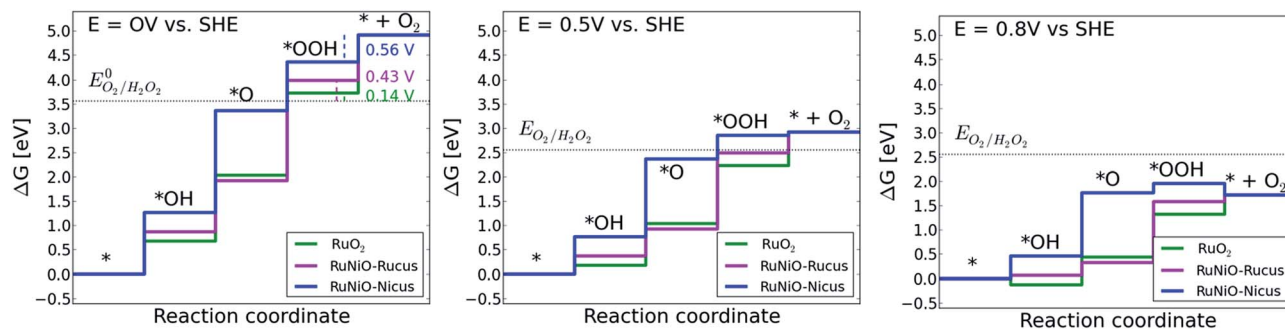

Fig. 11 Free energy diagrams for the reduction of O₂ on three catalytic active sites, the Ru cus site on conventional ruthenia (green), the cus Ru site on Ni doped RuO₂ (magenta) and the cus Ni site on Ni doped RuO₂ (blue). The dotted line represents the equilibrium potential of the reduction O₂ to H₂O₂. The key difference is the binding of O on the Ni cus site compared to the Ru cus sites.

Such a dual volcano plot has been used with great success in literature.[42,43] The volcano curves presented in Fig. 12 clearly show a quantitative prediction of the thermodynamic preference of the 4-electron reduction pathway over the 2-electron reduction on strongly adsorbing *cus* sites. As follows from Fig. 11, oxygen reduction on Ni-doped ruthenia should proceed at slightly more positive potentials compared with the non-doped ruthenia as long as the *cus* sites are occupied with Ru cations. The reduction process on Ru occupied *cus* sites should show a pronounced preference for 4-electron reduction and the formation of hydrogen peroxide should be excluded for potentials positive of 0.14 V or 0.43 V (*vs.* RHE) for non-doped ruthenia and the Ni-doped material, respectively (see Fig. 11). The easier formation of hydrogen peroxide on the Ni-doped material should be compensated by an earlier onset of the oxygen reduction process as predicted for Ni-doped material. In the case of weakly adsorbing sites, *e.g.*, in the case of Ni *cus* sites – there is no apparent thermodynamic preference for either the 4- or 2-electron reduction pathway. The DFT model predicts the onset of the oxygen reduction process to occur at potentials comparable with the ORR on non-doped ruthenia. The formation of hydrogen peroxide is possible at significantly more positive potentials (see Fig. 11).

Analyzing the experimental behavior of the ruthenium dioxide based catalysts for the oxygen reduction process in the light of the DFT results one can qualify the existence of two classes of catalysts – one favoring the 4-electron reduction (non-doped RuO_2 and Zn-doped RuO_2) and another showing significant activity in hydrogen peroxide production (Ni- and Co-doped ruthenia). Realizing that the Zn present in the Zn-doped ruthenia is itself redox inactive one can assume that the catalysts in the first group have all active *cus* sites occupied by Ru regardless of the actual chemical composition. The confinement of the catalytic activity to Ru itself justifies the selectivity towards 4-electron reduction pathway as it is shown in Fig. 4 and 8. In the case of the Co- and Ni-doped ruthenia the significant amount of hydrogen peroxide formed in the process can be attributed primarily to the Ni/Co *cus* sites although the Ru *cus* sites also contribute to the hydrogen peroxide formation at lower potentials. In contrast to the complementary oxygen evolution process, the Ni (or Co) ions located in the *bridge* sites, which play crucial role in the complementary anodic process,[33] apparently have no effect on the oxygen reduction activity of these materials. A different role of the catalysts local structure in oxygen reduction is not entirely surprising given the irreversibility of oxygen evolution/reduction.

The DFT calculations, however, fail to explain pronounced formation of the hydrogen peroxide on all ruthenium based catalysts at low overpotentials (0.55–0.40 V) when the hydrogen peroxide on Ru *cus* sites should be thermodynamically excluded. Given the relatively short timescale of the RRDE experiments one may therefore suggest that the system fails to reach the thermodynamically stable surface structure on the experimental timescale and the hydrogen peroxide is released from meta-stable intermediates not reflected in the DFT calculations.

Conclusions

Nanocrystalline ruthenia based electrocatalysts offer a convenient model for investigating the role of the local structure in the oxygen reduction on oxide electrodes. The oxygen reduction related activity of RuO_2 is comparable with that of the doped ruthenia. The selectivity of doped ruthenia catalysts differs from that of the RuO_2 in which the non-doped as well as Zn-doped catalysts prefer 4-electron oxygen reduction while the Ni- and Co-doped ruthenia produce significant amount of hydrogen peroxide. The observed selectivity trends can be rationalized using a thermodynamic analysis of the oxygen reduction process based on DFT calculations.

The DFT based analysis confines the oxygen reduction activity to *cus* sites the occupancy of which controls the selectivity of the oxygen reduction process. Oxygen reduction on non-doped ruthenium dioxide is controlled by the fourth electron transfer. Doping the ruthenium dioxide shifts the potential control to the first electron transfer. This trend can be attributed to decreasing occupancy of the *cus* sites with ruthenium. The strong adsorption of the *OOH intermediate on the Ru *cus* site steers the reaction mechanism towards 4-electron reduction pathway. Incorporation of reactive transition metal cations into *bridge* sites has negligible effect on the ORR activity. A confinement of the reactive transition metal into *cus* sites weakens the adsorption of the reaction intermediates and opens the 2-electron reaction pathway at relatively low overpotentials.

Acknowledgements

Notes and references

1 G. Chen, S. R. Bare and T. E. Mallouka, *J. Electrochem. Soc.*, 2002, A1092–A1099.

2 Y. Zhang, C. Wang, N. Wan and Z. Mao, *Int. J. Hydrogen Energy*, 2007, **32**, 400–404.

3 M. T. M. Koper, *J. Electroanal. Chem.*, 2011, 254–260.

4 I. C. Man, H.-Y. Su, F. Calle-Vallejo, H. A. Hansen, J. I. Martinez, N. G. Inoglu, J. Kitchin, T. F. Jaramillo, J. K. Norskov and J. Rossmeisl, *ChemCatChem*, 2011, **3**, 1159–1165.

5 S. Trasatti, *Electrochim. Acta*, 1984, **29**, 1503–1512.

6 M. Wohlfahrt-Mehrens and J. Heitbaum, *J. Electroanal. Chem.*, 1987, **237**, 251–260.

7 M. E. G. Lyons and S. Floquet, *Phys. Chem. Chem. Phys.*, 2011, **13**, 5314–5335.

8 S. Song, H. Zhang, X. Ma, Z. Shao, R. T. Baker and B. Yi, *Int. J. Hydrogen Energy*, 2008, **33**, 4955–4961.

9 S. Fierro, T. Nagel, H. Baltruschat and C. Comninellis, *Electrochem. Commun.*, 2007, **9**, 1969–1974.

10 A. J. Esswein, M. J. McMurdo, P. N. Ross, A. T. Bell and T. D. Tilley, *J. Phys. Chem. C*, 2009, **113**, 15068–15072.

11 C. C. Chang and T. C. Wen, *J. Appl. Electrochem.*, 1997, **27**, 355–363.

12 C.-C. Chang and T.-C. Wen, *J. Electrochem. Soc.*, 1996, **143**, 1485–1491.

13 F. Cheng, J. Shen, B. Peng, Y. Pan, Z. Tao and J. Chen, *Nat. Chem.*, 2011, **3**, 79–84.

14 M. Hamdani, R. N. Singh and P. Chartier, *Int. J. Electrochem. Sci.*, 2010, **5**, 556–577.

15 J. Suntivich, H. A. Gasteiger, N. Yabuuchi, H. Nakanishi, J. B. Goodenough and Y. Shao-Horn, *Nat. Chem.*, 2011, **3**, 546–550.

16 H. S. Horowitz, J. M. Longo and H. H. Horowitz, *J. Electrochem. Soc.*, 1983, **130**, 1851–1859.

17 R. G. Egdell, J. B. Goodenough, A. Hamnett and C. C. Naish, *J. Chem. Soc., Faraday Trans. 1*, 1983, **79**, 893–912.

18 M. Garcia-Mota, A. Vojvodic, H. Metiu, I. C. Man, H.-Y. Su, J. Rossmeisl and J. K. Nørskov, *ChemCatChem*, 2011, **3**, 1607–1611.

19 J. Rossmeisl, Z.-W. Qu, H. Zhu, G.-J. Kroes and J. K. Nørskov, *J. Electroanal. Chem.*, 2007, **607**, 83–89.

20 K. Macounova, M. Makarova, J. Jirkovsky, J. Franc and P. Krtil, *Electrochim. Acta*, 2008, **53**, 6126–6134.

21 V. Petrykin, Z. Bastl, J. Franc, K. Macounova, M. Makarova, S. Mukerjee, N. Ramaswamy, I. Spirovova and P. Krtil, *J. Phys. Chem. C*, 2009, **113**, 21657–21666.

22 N. Krstajic and S. Trasatti, *J. Electrochem. Soc.*, 1995, **142**, 2675–2681.

23 N. Krstajic and S. Trasatti, *J. Appl. Electrochem.*, 1998, **28**, 1291–1297.

24 L. M. D. Silva, J. F. C. Boodts and L. A. DeFaria, *Electrochim. Acta*, 2000, **45**, 2719–2727.

25 L. M. D. Silva, J. F. C. Boodts and L. A. D. Faria, *Electrochim. Acta*, 2001, **46**, 1369–1375.

26 L. M. D. Silva, L. A. D. Faria and J. F. C. Boodts, *J. Electroanal. Chem.*, 2002, **532**, 141–150.

27 V. Petrykin, K. Macounová, M. Okube, S. Mukerjee and P. Krtil, *Catal. Today*, 2013, **202**, 63–69.

28 K. Macounová, M. Makarova, J. Franc, J. Jirkovský and P. Krtil, *J. Electrochem. Soc.*, 2008, **11**, F27–F29.

29 V. Petrykin, K. Macounova, J. Franc, O. Shlyakhtin, M. Klementova, S. Mukerjee and P. Krtil, *Chem. Mater.*, 2011, **23**, 200–207.

30 V. Petrykin, K. Macounova, O. A. Shlyakhtin and P. Krtil, *Angew. Chem.*, 2010, **49**, 4813–4815.

31 Y. D. Tretyakov and O. A. Shlyakhtin, *J. Mater. Chem.*, 1999, **9**, 19–24.

32 U. A. Paulus, T. J. Schmidt, H. A. Gasteiger and R. J. Behm, *J. Electroanal. Chem.*, 2001, **495**, 134–145.

33 N. B. Halck, V. Petrykin, P. Krtil and J. Rossmeisl, *Phys. Chem. Chem. Phys.*, 2014, **16**, 13682–13688.

34 S. R. Bahn and K. W. Jacobsen, *Comput. Sci. Eng.*, 2002, **4**, 56–66.

35 B. Hammer, L. B. Hansen and J. K. Norskov, *Phys. Rev. B: Condens. Matter*, 1999, **59**, 7413–7421.

36 M. Pourbaix, *Atlas of Electrochemical Equilibria in Aqueous Solutions*, Pergamon Press, Oxford, U.K., 1966.

37 K. Macounová, I. Jirka, A. Trojánek, M. Makarova, Z. Samec and P. Krtil, *J. Electrochem. Soc.*, 2007, **154**, A1077–A1082.

38 A. J. Bard and L. R. Faulkner, *Electrochemical Methods: Fundamentals and Applications*, John Wiley & Sons, Inc., New York, 2nd edn, 2001.

39 N. M. Markovic, H. A. Gasteiger and P. N. Ross, *J. Phys. Chem.*, 1996, **100**, 6715–6721.

40 K. L. Hsueh, D. T. Chin and S. Srinivasan, *J. Electroanal. Chem.*, 1983, **153**, 79–95.

41 A. Damjanovic, M. A. Genshaw and J. O. M. Bockris, *J. Phys. Chem.*, 1966, **45**, 4057–4059.

42 S. Siahrostami, V.-C. Arnau, M. Karamad, D. Deiana, P. Malacrida, B. Wickman, M. Escudero-Escribano, E. A. Paoli, R. Frydendal and T. W. Hansen, *Nat. Mater.*, 2013, **12**, 1137–1143.

43 V. Viswanathan, H. A. Hansen, J. Rossmeisl and J. K. Nørskov, *J. Phys. Chem. Lett.*, 2012, **3**, 2948–2951.